2011

Weldability of Advanced High Strength Steels using Yb:YAG high power laser for Tailor-Welded Blank applications

Rajashekhar Shivaram Sharma
Iowa State University

Weldability of Advanced High Strength Steels using Yb:YAG high power laser for Tailor-Welded Blank applications

by

Rajashekhar Shivaram Sharma

A dissertation submitted to the graduate faculty in partial fulfillment of the requirements for the degree of
DOCTOR OF PHILOSOPHY

Major: Mechanical Engineering

Program of Study Committee

Pal Molian, Major Professor
Abhijit Chandra
Pranav Shrotriya
Scott Chumbley
Frank Peters

Iowa State University
Ames, Iowa
2011

DEDICATED TO MY DECEASED PARENTS:

Mrs. Padma Shivaram

and

Mr. H.S. Shivaram (Hanasoge Shivaramiah)

Incredibly loving, supportive and helpful parents with extraordinarily strong characters!

TABLE OF CONTENTS

LIST OF FIGURES

LIST OF TABLES

ACKNOWLEDGEMENTS

I would like to sincerely thank my major professor, Dr. Molian, for providing tremendous help and support during my work at Iowa State University. Without his support, I could not have started my work, let alone come to this stage of acknowledging his help in completing it. Incidentally, over twenty five years ago, Dr. Molian guided my master's degree work too, and I learnt then, as I did now, many things from him.

I would also like to gratefully acknowledge the help and support of Dr. Chandra, Dr. Shrotriya, Dr. Chumbley and Dr. Peters who kindly agreed to serve on my doctoral committee and provide advice and supportive comments to help me move towards successful completion of my dissertation.

Many other friends and colleagues at Ford Motor Company have helped me during the course of my doctoral work. I have spent many happy hours with John Bonnen discussing various aspects of my PhD work and asking for his opinion on various topics. John trained me in the use of fatigue test equipment and was very helpful and supportive. Ron Cooper has helped me tremendously in many areas by providing training in use of several test equipment such as microhardness tester, Instron tensile tester and others, offering excellent suggestions and always ready with great answers on questions related to advanced high strength steels, coatings and related topics. James Boileau trained me in using optical and scanning electron microscope, preparation of samples and other experimental work and all this was incredibly helpful. John and James also helped me with tensile sample preparation. Shannon Bollin and Jon Hangas helped me many times with problems related to optical and scanning electron microscopes. Among management, Matt Zaluzec helped me tremendously by allowing me use of the equipment at Ford Motor Company's Research and Innovation Center (RIC.) Brian Sullivan, my engineering supervisor, and, Shirleen Holland and Noah Mass, my managers, helped by supporting my venture. Brian has been incredibly patient with my constantly altering vacation schedules, which were necessary to allow me to work at RIC, and I know that he resolved some of my work related problems in my absence. Also in my absence, my colleague Mellissa Ream handled some of my responsibilities. Eric Frevik, Process and Engineering Manager in the Metal Formability group, gave me permission to use AutoForm FEA code, and I am currently working on mastering it. My colleagues, Karthik Viswanathan and Rudresh Chandrashekhar are currently helping me with modeling formability and tensile testing using AutoForm and LS-Dyna respectively. My grateful thanks go to all of them.

In addition to my friends and colleagues at Ford, many friends outside of Ford provided significant and indispensable help to me. Matt Gallagher, Benda Yan and Min Kuo of Arcelor Mittal, and Raj Mohan Iyengar of Severstal, provided me the DP980, TRIP780, USIBOR and mild steels for my experimental work, and helped me obtain valuable data related to these steels. My meetings with Min have been very helpful since he

has provided me with valuable thoughts on steels and their processing. Naveen Ramisetti helped by evaluating the microstructures in the fusion and heat affected zones using SEM and color tint etching, which are incorporated into Chapter 6. Juergen Stollhof and David Havrilla of Trumpf Inc gave me kind permission to use their laser welding facilities in their Plymouth, Michigan facilities, not once but twice; and, Hans Leidich helped me with high quality laser welding of all my samples and providing a ton of helpful suggestions and comments on laser welding. Tim Montroy and George Paraskos of AK Steel gave me permission to use their Middletown, OH facilities for my formability work and Rob Comstock spent a lot of his valuable time by preparing the samples, running the formability tests with me, modifying the dies to accommodate the difficult DP980 material and providing me with the data, which are all included in Chapter 6. My most sincere thanks to all of them for the invaluable help provided to me.

My wife, Ranjini, and my mother-in-law, Mrs. Padma Sundar, have been patiently supportive by helping out when they could during my erratic work hours. I have spent a major part of my vacation hours during the last five years at RIC and many weekends at home working on this project; during this time, they have shouldered more household responsibilities than they should have. Thanks to their help, my work has progressed satisfactorily. My son, Naveen, an incredibly sharp kid, helped me many times with software and formatting problems while making several helpful suggestions. My autistic son, Nikhil, has known that I am working on this difficult project and has been patient in his own way. My grateful thanks go to all my family members.

Finally I want to thank the long lineage of teachers that I have had the pleasure of studying under. I regretfully have to condense this list to just a few. My mother, Mrs. Padma Shivaram, a music teacher and a great Veena player, first instilled love of reading in me; and then my father, Mr. H.S.Shivaram, a renowned and highly popular high school math teacher, turned me into a great lover of both reading and mathematics. Mr. Appanna Reddy of Narayana Ghatta, my elementary school teacher, who opened my eyes to social problems at a young age, has made a profound impact on me. When I entered PES College of Engineering in Mandya under the University of Mysore, many great teachers such as Professors Riaz Ahmad of Chemistry, Narayana Rao of Mathematics, Basavaraj, Gangadharan and Nagarajiah of Mechanical Engineering Department, instilled love for science and engineering in me. At Indian Institute of Technology, Madras, Professors B.V.A. Rao, B.S. Prabhu and S. Narayanan were my favorite teachers. Professors Nagarajiah and Narayanan were my undergraduate and post-graduate major professors at Mandya and Madras respectively. Because of Professor Narayanan's course on Random Vibrations and our work on Monte Carlo methods, I became addicted to statistical methods, and happily, I probably will never be able to shake it off! Over at Iowa State University, when I worked on my master's degree in mechanical engineering, Professor Hotchkiss of Statistics Department reinforced that love for statistics while Professor John Verhoeven kindled a new interest in Materials Science in me. It was Professor Verhoeven who made me realize that Materials Science is not just a beautiful area, but also an extremely important one, since many engineering problems are related to materials as well as

manufacturing. Recently, when I took the course under him, Professor Molian showed the way to the beautiful, emerging world of micro/Nanomanufacturing. Thus I end my heartfelt acknowledgements by thanking all my teachers starting with Mrs. Padma Shivaram and Mr. H.S. Shivaram, and for now, ending with Professor Pal Molian.

ABSTRACT

Use of a high power Yb:YAG laser is investigated for joining advanced high strength steel materials for use in tailor-welded blank (TWB) applications. TWB's are materials of different chemistry, coating or thicknesses that are joined before metal forming and other operations such as trimming, assembly and painting are carried out. TWB is becoming an important design tool in the automotive industry for reducing weight, improving fuel economy and passenger safety, while reducing the overall costs for the customer.

Three advanced high strength steels, TRIP780, DP980 and USIBOR, which have many unique properties that are conducive to achieving these objectives, along with mild steel, are used in this work. The objective of this work is to ensure that high quality welds can be obtained using Yb:YAG lasers which are also becoming popular for metal joining operations, since they produce high quality laser beams that suffer minimal distortion when transported via fiber optic cables. Various power levels and speeds for the laser beam were used during the investigation. Argon gas was consistently used for shielding purposes during the welding process. After the samples were welded, metallographic examination of the fusion and heat-affected zones using optical and scanning electron microscopes were carried out to determine the microstructures as well as weld defects. Optical and scanning electron microscopes were also used to examine the top of welds as well as fracture surfaces. Additionally, cross-weld microhardness evaluations, tensile tests using Instron tester, limited fatigue tests as well as formability evaluations using OSU plane strain evaluation were carried out. The examinations included a 2-factor full factorial design of experiments to determine the impact of coatings on the surface roughness on the top of the welds. Tensile strengths of DP980, TRIP780 and mild steel materials as well as DP980 welded to TRIP780 and mild steel in the rolling direction as well as transverse direction were evaluated.

Metallographic examinations determined that most of the fusion zone is martensitic with small regions of bainite and ferrite. High microhardness values of the order of 550 - 600 Hv were noted in most joints, which are attributed to high alloy content of the fusion zone as well as high rates of cooling typical of laser welds. During tensile, fatigue and formability tests, no fractures in the fusion or heat affected zones were observed. Geometric variability evaluations indicated that coatings such as aluminum (in the case of USIBOR) and galvanized zinc (TRIP780) can affect the variability of the weld zone and the surface roughness on the top of the weld. Excessive variability in the form of weld concavity in the weld zones can lead to fractures in the weld region, even though higher hardness can, to some extent, compensate for these surface irregularities. The 2-factor design of experiments further confirmed that coatings adversely affect the surface roughness on the top of the welds. Although thickness differentials alone do not make a significant impact on surface roughness, together with coatings, they can have an adverse effect on roughness. Tensile tests in the direction of rolling as well as in the transverse direction indicate that TRIP780 seems weaker in the direction of rolling when

compared to transverse direction while mild steel is stronger in the direction of rolling. Weldability analyses revealed that the typical melting efficiency is on the order of 50-70% for full penetration welding. Formability tests showed that TR/MS joints fractured in a direction parallel to the weld line when tested with the loads perpendicular to the weld line. Tests have also confirmed that weld speed and power have no impact on the outcome of formability results.

Overall, this work conclusively proves that high power Yb:YAG lasers can effectively join high strength materials such as DP980, TRIP780, USIBOR, as well as mild steel, for use in tailor-welded blank applications, contributing to lighter, more fuel-efficient and safer vehicles.

CHAPTER 1. INTRODUCTION

1.1 Introduction

Automotive companies worldwide are under increasing pressure to improve fuel economy of vehicles due to increasing fuel costs as well as limited fossil fuel availability, while ensuring that the vehicles perform at optimum levels. These often conflicting requirements include high margin of safety during all kinds of accidents such as vehicle rollover, side impact and frontal collision. Reducing vehicle weight, without sacrificing the safety and other functions as needed, is the key to achieving these objectives. Although the use of materials such as aluminum and, in some rare cases, magnesium, for manufacturing of body structures and closures do reduce weight, these can be considerably expensive. The alternative is the use of tailor-welded blanks (TWB) using advanced high strength steels (AHSS) that will result in significant weight reduction while maintaining the safety levels of the vehicles and carefully controlled costs. The definition of TWB is joining of materials of differing compositions, coatings and or thicknesses by a suitable metal joining operation before further operations such as metal forming, edge trimming, hole piercing, joining with other panels and painting are carried out.

An automobile body requires many high performance characteristics such as high strength, durability, corrosion resistance and crash worthiness while minimizing the weight to achieve maximum fuel efficiency and minimizing the cost to the customer. In order to meet all these characteristics, hundreds of panels with varying sizes were developed. However, engineers understood that to improve accuracy, reliability as well as productivity, the number of parts must be minimized for each body panel. TWB produced by cutting and welding before metal forming (Figure 1.1) thus came into existence. Apart from reducing the number of parts, the advantages of TWB are numerous: Fewer dies are required, fewer spot welds, reduced design and development time, lower manufacturing costs, less material volume and thus better utilization of raw materials, improved dimensional accuracy and structural integrity [1]. An excellent illustrative example that explains some of these concepts is offered by Bob Lewinski, Vice President for marketing and sales for VIL/Wayne Trail Technologies as follows [2]: "It may be desirable to form a component such as an inner door panel that has a deep-draw depth to accommodate the contour of the finished vehicle door. This requires a very soft, and relatively thin metal. However, the front of the same inner door where the hinges will attach have to be strong enough to hold up the weight of the entire door. In the past, this would have required the addition of several extra parts to strengthen this area. By producing a tailored blank with a large, thin soft piece of flat material joined to a thick, stronger small piece of flat material, this customized blank can then be formed into one piece inner door, deeply drawn in one area." Thus, following Bob Lewinski's logic, the hinge and latch reinforcements, and, possibly other parts such as belt reinforcement and even side intrusion beam, can be

eliminated by use of one inner panel using a clever TWB design. This will eliminate several dies and manufacturing sequences which will lead to many of the advantages stated earlier.

The history of TWB's goes back to 1979 when Volvo used resistance mash seam process in Europe. Today TWB's are "… used for body side frames, door inner panels, motor compartment rails, center pillar inner panels and wheelhouse/shock tower panels"[1]. In the near future, they'll be used on more body parts due to the reduction in tooling and operating costs. Several examples for TWB applications are provided in literature [3, 4].

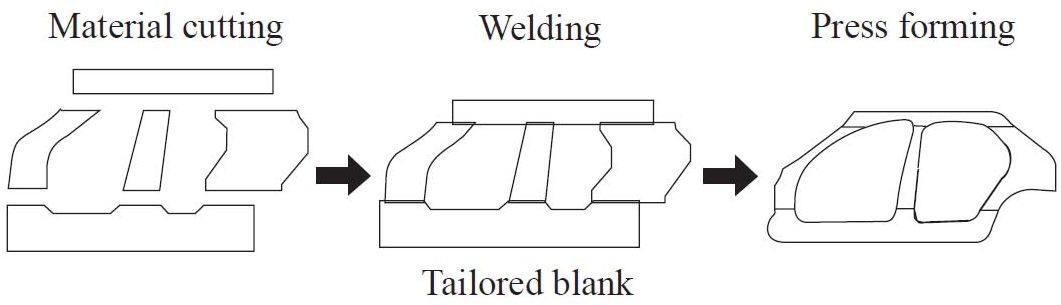

Figure 1.1 An application of TWB to body outer panel [5]

TWB's are produced by laser welding, mash seam welding, and plasma welding. Laser welding is a "keyhole" fusion welding process that produces welds with narrow width and deep penetration. Lasers are ideal for TWB applications as these both cut individual blanks and weld the component parts to form a finished tailored blank; during this process, a laser weld results in small fusion and heat affected zones. Other advantages of laser welding include: high processing speed, low heat input, high-strength joints and easy to automate. Mash seam welding is a resistance welding process using electrode wheels with high-speed capability; however it suffers from contamination, wider seam, poor weld bead appearance and difficulty in welding high-strength steel sheets. The welds exhibit lower hardness than laser welds. Plasma welding is also a keyhole welding process with lower cost of equipment than laser and mash welding units. However the seams are much wider and inferior in formability.

There are two central issues in the manufacture of laser TWB: One is the needed edge preparation while the other is the type of laser used for welding. In the first case, since it is necessary to keep the edges close to each other with narrow gaps, an edge preparation such as milling or even laser cutting to close tolerances are necessary. After this, the blanks are loaded into fixtures with clamping systems that apply side pressure on the fixtures or use a roller system to deform the sheet adjacent to the weld to keep edges in intimate contact (<0.1 mm gap). Such preparation is important when welding is carried out autogenously, but when filler material is used, the edge preparation becomes less important; however, use of a filler material during welding adds to the

cost of the process. Beam weaving or twin spot welding processes can also be used to overcome this issue, but the maximum welding speeds that can be achieved will be compromised and this too adds to the total costs. For the choice of laser type, 5-6 kW continuous wave CO2 lasers were extensively used in automated production systems prior to the development of Nd:YAG lasers with more than 3 kW power. A number of TWB production systems based on Nd:YAG lasers have been installed for tailored blank manufacture which have the benefits of increased versatility due to the fiber optic beam delivery, higher welding speeds (due to the improved coupling of the laser wavelength), improved tolerances to gaps and elimination of the need for gas shielding.

The development of disk lasers such as Yb:YAG significantly improved the advantages of using lasers for TWB preparation. In the case of Nd:YAG lasers, the YAG rod (typically 6 mm diameter and 150 mm long) which is cooled by water, results in thermal gradients from the outer surface (which is maintained at a lower temperature) and the hotter core; this results in lower beam quality. The thin disk lasing medium, typically 14 mm diameter and 0.2 mm thick, is mounted to a water cooled block and exhibits nearly negligible thermal gradient, resulting in a higher beam quality. Also, the back reflection of the laser beam, in the case of diode lasers, are lower when compared to the rod lasers, which eliminates extremely high peak powers that can damage internal optics and the fiber optic cables that carry the laser beam. For this reason, laser beam produced by Yb:YAG laser can be transported to a remote location with minimal distortion of the beam. Another advantage of Yb:YAG lasers (and Nd:YAG lasers too) is that they produce a high wall plug efficiency of greater than 15% when compared to 3% to 4% for lamp-pumped laser [6]. For these reasons, the reliability of Yb:YAG lasers is very high and their maintenance costs are lower [7]

Advanced high strength steels (AHSS) offer yield strengths in excess of 350 MPa and tensile strengths as high as 1700 MPa for martensitic steel as shown in Figure 1.2 [8, 9]. Several grades of these steels such as Dual Phase (DP), Transformation Induced Plasticity (TRIP) and Complex Phase (CP) steels can be processed in the conventional way while others like boron steels (also called USIBOR) need special processing. Among these, DP steels are the most popular, and are used in door beams, bumper reinforcements and in seat structures and seat tracks, while USIBOR is finding applications in front and rear end rail extensions, A- B- and hinge pillars and reinforcements, and door and bumper beams [10]. Ford Motor Company, for example, has used DP steels for rocker panels, side roof arch and hinge pillars and aluminized boron steel for A-pillar [11]. Similarly, General Motors has used considerable ultra high strength steels in addition to high strength steels in Chevy Volt to improve crashworthiness and stiffness of the body structure; over 70% of the body structure is said to have been designed with high strength steels [12]. The use of AHSS materials are projected to increase over the next decade. Dick Schultz and Abey Abraham of Ducker Worldwide state that the use of DP steel is projected to increase from 110.7 lbs per average car in 2009 to 312 lbs per average car in 2020, while the total AHSS is projected to increase from 150.8 lbs to 450 lbs during the same period [13].

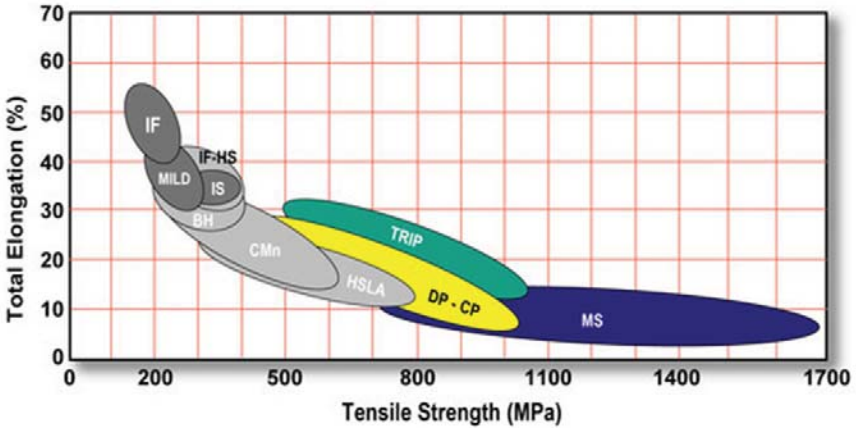

Figure 1.2 Conventional, low strength steels (shown in dark gray), high strength steels (shown in light gray) and advanced high strength steels (shown in color) [8]. Boron steels, also called USIBOR, are part of the martensitic steels shown in the blue region.

Use of AHSS materials in TWB applications further improves the effectiveness of the process. By integrating AHSS with TWB using a high power laser beam, automakers can aggressively reduce the weight and cost of their products. This idea is being stressed increasingly by steel suppliers. For example, Arcelor points out that "a tailor welded blank with AHSS and drawing steels allows for instance to combine the strength necessary in the middle with the formability requirements in the upper and lower parts of a B-pillar" [14]. Automakers seem to agree with similar analysis and are implementing a combination of AHSS and TWB's. For example, Ford Motor Company used DP600 as part of tailor-welded blanks in the side member inner where it was teamed with HSLA 250, and the side member outer where it was combined with mild steel [15]. More research, in all aspects involving AHSS, TWB and laser welding, needs to be carried out to help the OEM's achieve their goals. Use of AHSS materials by Ford Motor Company is shown schematically in Figure 1.3.

1.2 Objectives of this research

The overarching goal of this research project is to enhance the knowledge-base in tailor welded blanks consisting of advanced high strength steels as well as mild steel, using a high power laser. Specific objectives consist of the following:

1. To confirm that high quality welds can be obtained by using the laser beam produced by a high power disk laser such as Yb:YAG (which uses ytterbium doped yttrium aluminum garnet crystal as the lasing medium) carried to a remote location with the use of fiber optics technology.

2. To assess the melting efficiencies during the welding process and to confirm that laser welding using Yb:YAG is a highly efficient process. Confirmation of the accuracy of the weld speeds predicted by mathematical models using bead-on-plate experiments is also of part of this objective.
3. To understand the microstructures in the heat affected zones as well as the fusion zones of various combinations for the AHSS materials, to assess the microhardness values in these zones and to confirm using tensile and fatigue tests that the joints obtained would be of high quality,
4. To assess the variability of the fusion zones as well as the roughness of the top of the weld zone, as this variability can have significant impact on the performance on the joint on a statistical basis, and,
5. To assess the formability of the joints using a process such as the Ohio State University (OSU) formability test for plane strain tests and confirm that the joints would not fracture during metal forming.

Statistical analysis is applied to draw conclusions in several areas of the dissertation and, where appropriate and available, variability in the results are presented, since such information is vital to ensure high quality in practice.

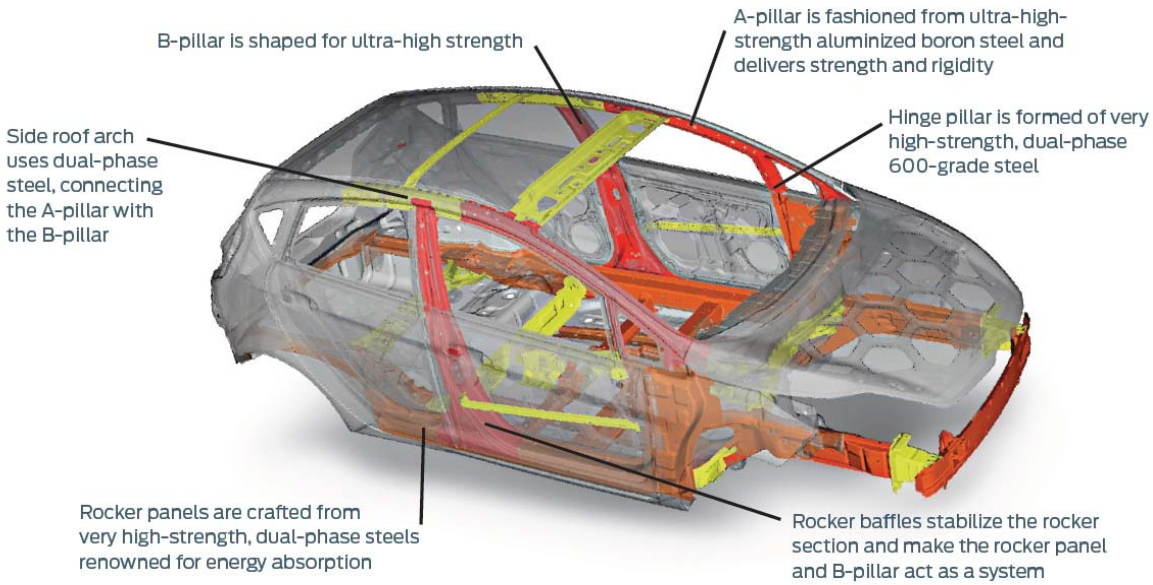

Figure 1.3 Ford Motor Company uses AHSS materials in several advanced vehicles including European Ford Fiesta [11]

1.3 Thesis organization

A brief literature survey of all aspects of TWB's including AHSS materials is provided in Chapter 2. This chapter is kept brief since a detailed literature survey is provided in the beginning of Chapters 3-6. Chapter 3 explains the microstructural examinations as well as tensile and fatigue tests carried out on combinations involving TRIP780 steels, namely, TRIP780 welded to mild steel and DP980 steel. The dimensional variability obtained for various combinations is examined in great detail in Chapter 4. Results of the evaluation of weld efficiencies and depth of weld are presented in Chapter 5. Formability evaluations of AHSS materials, in particular TRIP780 steel welded to mild steel, is presented in Chapter 6. Appendix A presents results of a 2-factor full factorial Design of Experiments that examined the effects of coatings and thickness differentials between samples being welded on surface roughness on the top of the weld. Appendix B examines the effect of rolling direction on the strength of the joints, while Appendix C provides further information on disk lasers.

1.4 References:

[1] Ronak, T. Working with Tailor-Welded Blanks. Body Shop Business, May 2006. http://www.bodyshopbusiness.com/Article/2882/working_with_tailorwelded_blanks.aspx.

[2] Trem, R. The Future of Automaking: Tailor Welded Blanks. February 2004. http://weldingdesign.com/consumables/news/wdf_10713/

[3] Auto-Steel Partnership. Tailor welded blank applications and manufacturing. http://www.a-sp.org/database/custom/twb/TWBApp.pdf

[4] TWB Company. Applications. http://www.twbcompany.com/Applications.html

[5] Miyazaki, Y., Hashimoto, K., Kuriyama, Y., Kobayashi, J. Welding methods and forming characteristics of tailored blanks (TBs). Nippon Steel Technical Report No. 88 July 2003. http://www.nsc.co.jp/en/tech/report/no88.html

[6] Havrilla, D. DISK LASERS: YAG is redefined through the diode-pumped disk laser. Laser Focus World, http://www.laserfocusworld.com/articles/print/volume-41/issue-8/features/disk-lasers-yag-is-redefined-through-the-diode-pumped-disk-laser.html

[7] Ream S.L. Disk and fiber gain ground. Industrial Laser Solutions. http://www.industrial-lasers.com/articles/2005/02/disc-and-fiber-gain-ground.html

[8] Automotive steel definitions. http://www.worldautosteel.org/SteelBasics/Definitions/Automotive-Definitions.aspx

[9] Advanced high strength steels: A collision perspective. http://www.i-car.com/pdf/advantage/online/2006/061206.pdf

[10] Kuvin, B.F. The rapid advancement of advanced high strength steels. Metal forming facts, 2011. http://www.metalformingfacts.com/forming-basics/advancement-high-strength-steel.html

[11] Ford Motor Company. Ultra-high-strength-steels. http://media.ford.com/images/10031/Boron.pdf

[12] General Motors uses advanced high-strength steel in 2011 Chevy Volt structure. http://www.azom.com/news.aspx?newsID=26036

[13] Schultz, R.A., Abraham, A.K. Metallic material trends for North American light vehicles. Great Designs in Steel, 2009, http://members.steel.org/AM/TemplateRedirect.cfm?Template=/CM/ContentDisplay.cfm&ContentID=32138

[14] Arcelor Steel. Tailored blanks value proposal. http://www.google.com/url?q=http://www.arcelormittal.com/fce/repository/Tailored_Blanks/Catalogue-Chapter1.pdf&sa=U&ei=MWdZTrLoE6rD0AGEh8SbDA&ved=0CCQQFjAH&usg=AFQjCNHvNKT_zIa0ySUG_csqfmssyI6W4Q

[15] Auto World Steel. http://www.worldautosteel.org/Applications/Vehicles/Ford-Freestyle.aspx.

CHAPTER 2. LITERATURE SURVEY

2.1 Advanced high strength steels

Before the literature survey of tailor-welded blank (TWB) applications of advanced high strength steels (AHSS) is presented, it is imperative that the science behind these materials is provided. AHSS consists, as of today, mostly of Dual Phase (DP), Transformation Induced Plasticity (TRIP), Complex Phase (CP) and martensitic (MS) or martensite phase (MP) which includes boron-alloyed (MnB or USIBOR) steels. Other steels such as Twinning Induced Plasticity (TWIP) are still in the laboratory stage and are left out of this chapter.

Among these, TRIP steels, or, more appropriately, "TRIP-assisted steels" [1] have high work hardening rates and combine high strength greater than 750 MPa with excellent ductility. Main metallurgical mechanism in these steels that provide these properties involves the strain-induced transformation of austenite to martensite during cold rolling [2]. As a result of these properties, TRIP steels offer high strength and toughness combination with excellent uniform elongation. Since these steels have ability to absorb more energy during crash due to the delayed transformation of retained austenite to martensite, they are used widely in automotive industry where such energy absorption during crash conditions is important. TRIP steels have a microstructure consisting of various fractions of ferrite, martensite, bainite, and retained austenite, giving the steels their unique balance of properties. Generally lower carbon levels are preferred for TRIP steels so that transformation of retained austenite to martensite occurs at the beginning of forming leading to excellent formability and strain distribution; at higher carbon levels, retained austenite is more stable and does not transform into martensite. It should be noted that further transformation to martensite occurs during subsequent deformation such as crash event, and this provides even greater crash energy absorption [3]. Microstructure of TRIP780 steel and is shown in Figure 2.1 with small regions of retained austenite.

DP steels consist of a dispersion of islands of hard martensite (5 to 20% by volume) in soft ferrite matrix [3]. These steels are characterized by high work hardening and used in automobile components that require high strength, good crashworthiness and acceptable formability. The strength levels of these steels depend upon the amount of martensite in the microstructure, which varies considerably depending upon the steel grade. DP steels are produced by controlled cooling from the austenite phase (in hot-rolled products) or from the two-phase ferrite plus austenite phase (for continuously annealed cold-rolled and hot-dip coated products) to transform some austenite to ferrite before a rapid cooling transforms the remaining austenite to martensite [4]. Although DP steels have excellent mechanical properties, the persistence of high work-hardening rate at higher strains in TRIP steels gives them a distinct advantage over DP steels on formability. As noted under Chapter 1, DP steels are the most popular AHSS choice among automotive companies.

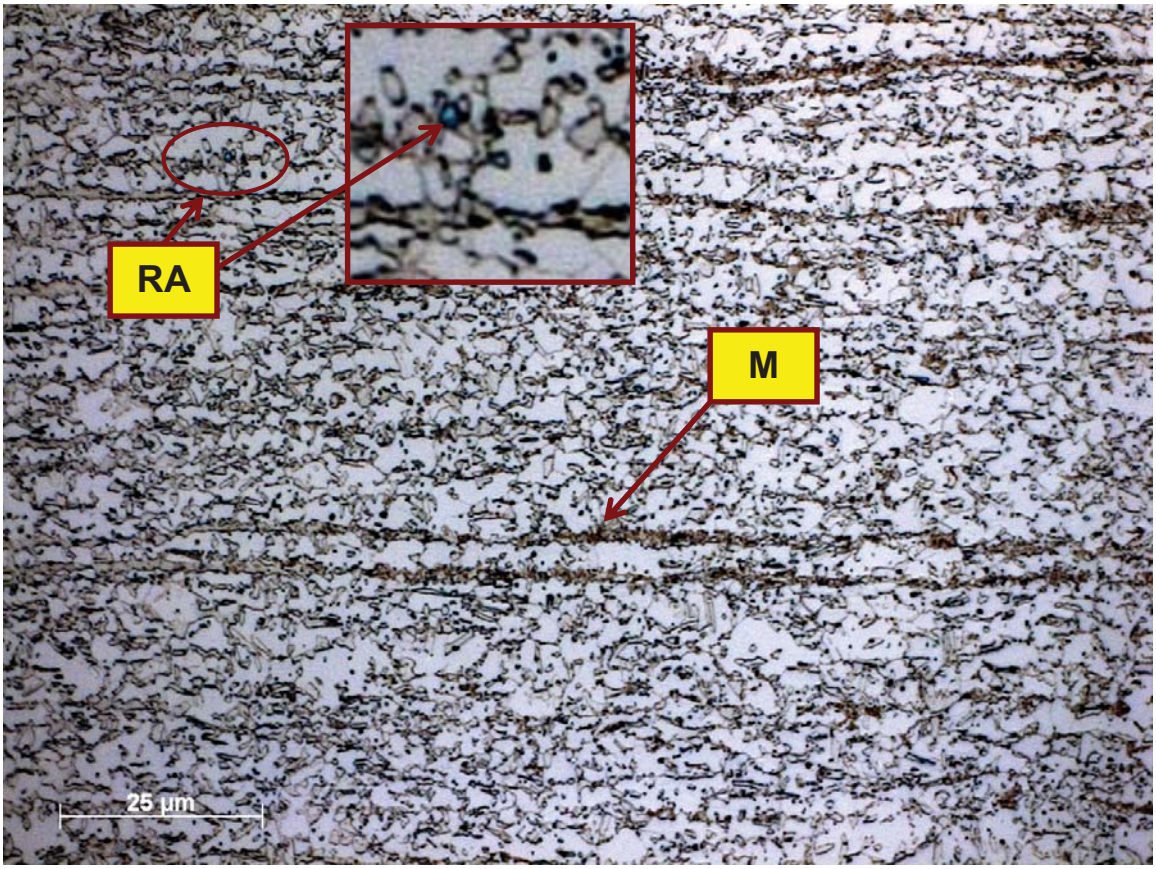

Figure 2.1 TRIP780 Microstructure showing martensite and retained austenite in a soft matrix of ferrite and bainite (Image captured by Naveen Ramisetti of Arcelor Mittal after treating with sodium metabisulphite).

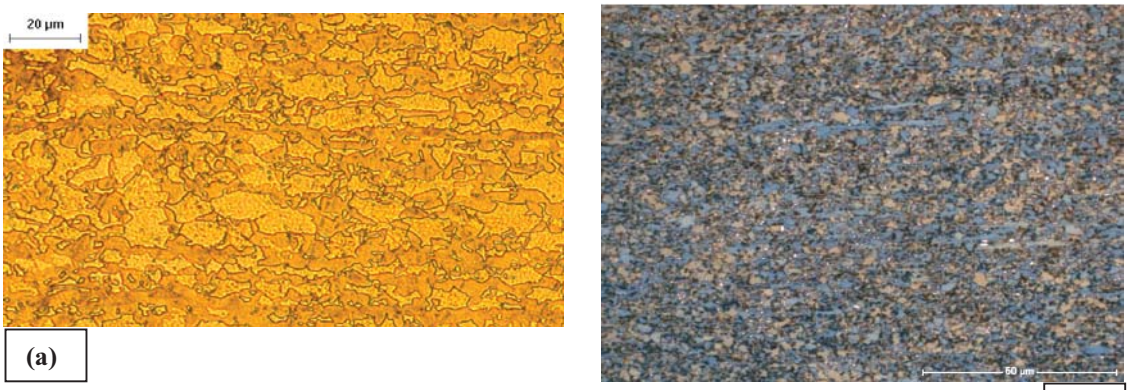

Figure 2.2 Optical micrographs of (a) DP steel (captured at 400X), and, (b) Complex Phase Steel (ThyssenKrupp CP-K 70/98. www.thyssenkrupp-steel.com)

CP steels offer very high minimum strengths and are characterized by high work hardening potential even at low levels of deformation and high wear-resistance [5]. The microstructure of CP steels contains small amounts of martensite, retained austenite and pearlite within ferrite/bainite matrix. In comparison to DP steels, CP steels show significantly higher yield strengths at equal tensile strengths of 800 MPa and greater. CP steels are characterized by high energy absorption and high residual deformation capacity [4]. Optical micrographs of DP and CP steels are shown in Figure 2.2.

Martensitic steels have a microstructure of entirely martensite with small amounts of ferrite and/or bainite [6]. To create MS steels, the austenite that exists during hot rolling or annealing is transformed into martensite during quenching in the cooling section of the continuous annealing line or via post-forming heat treatment. One example of martensitic steels is boron-alloyed ultra high strength steels (MnB), trademarked as USIBOR, and is widely recognized by automakers. Essentially this steel (hot stamped and die-quenched) contains Mn and B as alloying elements resulting in excellent hardenability. Hot stamping process consists of heating the blank to austenitization, press forming and then quenching within the die to form hard phases that give rise to extreme tensile strength of up to 1500 MPa. It may be noted that the base material, 22MnB5, has a ferritic-pearlitic microstructure with a tensile strength of approximately 600 MPa; after the part is hot stamped, it has a martensitic microstructure and increased strength, up to 250% of its initial value [7]. Thus MnB steels offer great potential for minimizing component weight by reducing sheet thickness as well as the number of components needed.

2.2 Welding Techniques and related issues

Laser welding is the preferred method of joining materials for TWB's, since a continuous weld line can be obtained when lasers are used. However, friction stir welding (FSW) is also being explored to join AHSS materials for spot welding. For example, Feng et al [8] studied welding a 600 MPa DP steel to a 1310 MPa martensitic steel (M190) and concluded that it is possible to use the fixed pin approach to produce metallurgical bonding for both DP600 and M190 in under 3 seconds of welding time. A similar demonstration that FSW can be effectively used to join AHSS was carried out by Hovanski and Santella [9], Sklad et al [10]. Khan et al [11] studied both resistance spot welding and friction stir spot welding of DP600 and concluded that a correlation can be found among microstructure, failure loads, energy requirements and bonded area for both processes.

Butt welding is the preferred method for joining AHSS materials and, where TWB's are involved, the only process that can be used. Welding of galvanized AHSS steels results in vaporization of zinc, which needs to exit from the weld-pool area; for this reason, spacers (commonly called shims) are used when lap welding of

galvanized steels is carried out [12]. Butt welding does not carry this disadvantage. However, in the case of butt welding, the edges need to be machined (milling or grinding). Liu et al [13] suggest keeping the gap between the workpieces at 0.04 mm, Wu et al [14] at 0.10 mm to 0.15 mm and Shao et al [15] at 0.2 mm or better. Such close gaps are more important when parts are welded autogenously, and a way to resolve it is by use of filler material [12]. A fixture is recommended for both butt and lap welds to keep the workpieces close to each other. This is more critical in lap welds, where a larger gap may result in increased interface fusion zone between the parts resulting in poor shear strength. Use of a shielding gas such as Argon might be helpful to avoid hydrogen embrittlement, although the type of shielding gas and the volumetric flow rate required depend upon specific applications. Nitrogen is probably not a good choice [14] since it may react with the molten pool. Argon seems to be the shielding gas of choice, although Nitrogen [14] and Helium [16] are also sometimes used. Hartley and Ono [17] used Corgon 18 (82% Ar, 18% CO_2) with success on DP steels for tailored blank applications. It is important to remove oxide layers and contamination from the surfaces before welding, as these would adversely affect the weld properties. The choice for the workpiece thickness is important, as larger specimen thickness may result in more frequent weld defects as reported by Matsumoto et al [18]. They also report that a larger welding heat input may be favorable since it keeps the fusion zone molten for longer periods of time and allows in-molten metal gas to escape and thus reduce porosities. This, however, results in larger heat affected zone (HAZ) which may not always be desirable. The choice of the laser is also important. Nd:YAG and Yb:YAG lasers offer higher energy absorption due to lower reflectivity; this can help achieve higher welding speeds and thus lower costs, and also result in lower residual stresses. But these lasers need special eye protection, a disadvantage not present among CO2 lasers. Depending upon the type of laser used, proper protection should be worn to prevent eye injury [19].

2.3 Weld geometry and defects

During welding of butt joints, a concave shaped bead formation on the top of the weld can sometimes result. Yan and Gallagher [20] observed such concave shaped weld pool formation on the top, during welding of EDDS and DP590 steels and other combinations. At the bottom of the weld pool, due to the effects of gravity, concavity is almost never observed. At the bottom of the weld zone, a tear-drop shape with concave-up geometry is noticed. Even when full penetration is not achieved, due to the shape of the laser beam (generally a Gaussian shape), the bottom of the fusion zone is generally concave up.

Yan and Gallagher [20] have observed that concavity has little effect on the results of tensile tests, if the concavity is less than 20% of the metal thickness. They attribute this to the higher strengths obtained in the weld pool and the HAZ of the welded samples. A combination of softening of HAZ and concavity could, however, adversely affect results of transverse tensile tests. For example, high strength AHSS materials such as DP980, when welded to itself, would result in lower hardness in the HAZ; in such cases, weld concavity could become an important consideration.

Generally, with increased speeds, weld widths become narrower. But welding carried out by Yan and Gallagher [20] on M900 steels showed different results. They found out that for the same conditions, the average weld pool widths were lower than those for other materials (0.9 mm width for cold rolled M900 steel, versus 1.4mm for DP600 GI and HSLA350 GI steels). The authors suggest that this could be attributed to absence of spacers during welding of M900, which was carried out as a lap joint.

During butt-welding of 800 MPa class TRIP steel using a CO_2 laser, Han et al. [21] found that porosity will be lower at higher welding speeds.

2.4 Microstructures in the weld

During laser welding of materials, high cooling rates are experienced by both the fusion zone and HAZ, which results in transformation of microstructures. During laser welding of 1.6 mm EDDS steel (an interstitial-free steel), Yan and Gallagher [20] observed growth of small clusters of Widmanstatten ferrite and allitromorphic ferrite growing from the grain boundaries inside large columnar ferrite grains inside the fusion zone (see picture). On the other hand, laser welding of HSS350 material resulted in a small amount of austenite formed from dissolved cementite, which transformed into Widmanstatten ferrite or pearlite, with the amount of pearlite increasing at points closer to the fusion zone, and the fusion zone consisted of almost 100% Widmanstatten ferrite and small amounts of primary ferrite. Both EDDS and HSS350 materials show hardness values continuously increasing from base material through HAZ and into the fusion zone.

When materials such as DP600 steels are laser welded, the hardness in both the fusion zone and HAZ will also tend to be higher than that of base metal. This is because the high alloying content of AHSS materials increases the carbon equivalent and, coupled with the rapid solidification process observed in laser welding, generally increases the potential for the formation of martensite. While laser welding DP590 steel (consisting of ferrite and 20% martensite), Yan and Gallagher [20] found that some austenite formed in the HAZ in the intercritical region, which subsequently transformed to new martensite during cooling after welding. Closer to the weld fusion line, more and more austenite formed, some of which subsequently transformed into martensite. In the fusion zone, the microstructure was 100% martensite. This resulted in a continuous increase in hardness from base metal to the fusion zone. This phenomenon has been found to occur in the case of spot-welding of DP600 steels as well [22]. On the other hand, when materials such as Martensitic steels that contain high proportion or 100% martensite are laser welded, the HAZ experiences 'softening' due to tempering of martensite which leads to formation of ferrite with regions of martensite, thus resulting in lower microstructural hardness. Similar phenomenon was observed by Xia et al [23] who found softening of the HAZ while welding DP980, which contains significantly larger proportion of martensite in a matrix of ferrite. Such softening was not noted by the same authors while welding the relatively softer HSLA steels. Other authors [17, 24] confirmed such softening

of HAZ in DP980 steels. Interestingly, Hirai et al [25] report that there is some softening during welding of DP590 steels also. The authors attribute this to thermal softening of the martensitic phase. Apparently their results do not agree with the results reported by Gallagher, et al. [12] during laser welding of DP600 steels. Comparison of the weld profiles obtained by Hirai [25] and Gallagher et al [12] is shown in Figure 2.3.

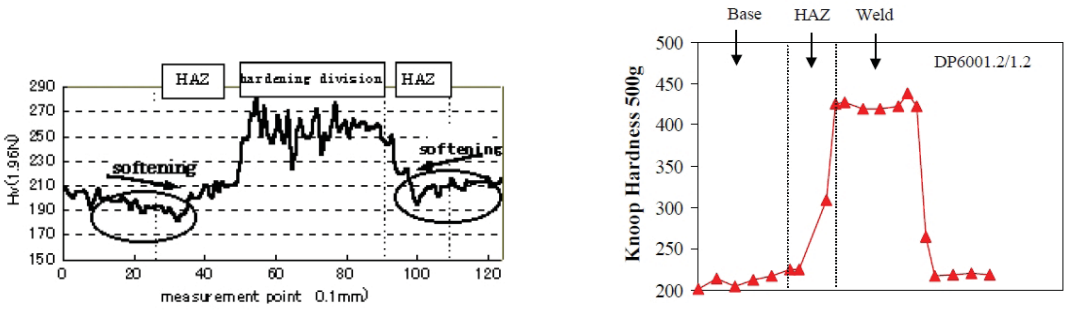

(a) **(b)**

Figure 2.3 (a) Drop in the microhardness at the edge of HAZ in DP590 [Hirai] (b) Microhardness in DP600 laser weld does not show such drop in microhardness [Matt Gallagher and Benda Yan]

2.5 Tensile tests

Tensile tests run by Gallagher et al [12] show that for lap welds, as the weld speed is decreased and higher weld penetration achieved, tensile strengths of the joints increase until the penetration reaches 30% thickness of the lower substrate, when maximum weld strength is achieved. This trend is observed for IF and HSLA350 steels as well. DP600 steels showed failures in an area away from the welds which indicates that maximum strength is governed by the base material properties for materials that do not soften in the HAZ region during laser welding. Tensile tests conducted on optimized weld conditions show that 2.0/2.0 DP600 steels (2 mm thick DP600 steel welded to 2 mm thick DP600) perform better than 2.0/2.0 M1310 steels, Also, DP600 consistently showed higher elongation than the Martensitic or mixed Martensitic/DP steels, which is not surprising.

Tensile tests run by Wu et al [14] on laser welded galvanized DP800 DOGAL steel showed failures mostly in the heat affected zones of the welded steels, while tailor-welded weldment on general steels similar to an IF steel break off far away from the weld seam. The authors comment that laser welding of high strength galvanized steel sheets do not soften HAZ, although the authors do not show hardness values in the fusion and HAZ zones. Microstructural analysis of fusion zone in the galvanized DP800 steels shows upper bainite + low carbon martensite microstructure and the HAZ show upper bainite + low carbon martensite + ferrite microstructure, which explains the failures in the HAZ for DP800 steels.

Work carried out by Xia et al [23] on HSLA and DP980 steels show that transverse tensile tests of DP980 steels result in failures in the HAZ by ductile rupture where softening occurs. Closer examination revealed that yielding occurred first in the soft zones resulting in necking and eventual failure. Failure zones in the HSLA materials are not explained, although HSLA shows somewhat higher variance in the values with excellent elongation.

2.6 Formability tests

Most researchers use Erichsen cup test using AISI test procedure [26]. Generally the hardness (or strength) plays a major role in the outcome of formability tests. This includes the effect of rolling direction in cases where softening of HAZ does not affect the performance of the joint. For example, tests run by Xia et al [23] indicate that directionality of rolling may be an important factor in some cases when weld region is not stretched. The authors report that formability tests run on parent DP980 steels showed fracture path was at a radial distance of 17 mm from the disk center and propagated in a direction parallel to the rolling direction in all cases. Formability tests run on parent HSLA material did not show such relationship between rolling direction and direction of fracture. However, when formability tests were run on welded samples of DP980, the fracture was always entirely in the outer HAZ. The DP980 specimens with laser welds showed strain values lower than DP980 parent specimens. In the case of HSLA, there was no difference in the fracture path followed by samples with weld seam versus samples of parent metal. Xia et al [23] infer that a specimen with fewer differentials in microhardness performs slightly better during formability tests. The softer zone first yields compared to the surroundings, resulting in a severe concentration of strain in that area. Thus specimens with local softening would show failures earlier, with a resultant lower average strain value. The resulting Martensitic substructures would aggravate the problem. This seems to indicate that a joint such as laser welded HSLA materials would result in excellent stretchability; Xia et al report that the laser welded HSLA materials have a 98% formability value of the parent material.

Tests run by Wu et al [14] on DP800 and general steel (comparable to Mild Steel) shows that the Erichsen number of equal thickness TWB's will reduce by 20% from the base material values due to microstructural changes and increase in microhardness of fusion zone and HAZ. Differential thickness TWB's fared worse, with 35% drop in Erichsen number from those of base materials.

Saunders and Wagoner [27] note that when samples are stretched parallel to the weld, the limited weld ductility allows cracks to nucleate and propagate normal to the weld line; and when the samples are stretched perpendicular to the weld, the stronger material constrains the weaker one to fail near plane-strain tension with the crack in the weaker material running parallel to the crack. This observation is reflected in the results of formability tests reported by Sreenivasan et al [24]

2.7 Fatigue tests

Tests run by Yan and Gallagher [20] suggest that the fatigue strength of laser welded specimens is lower than the parent metals. This difference is more in the low load and long life region than high load and short life region. Tests run by these authors on DP600 2.0 mm welded to 2.0 mm thick plates (DP600 2.0/2.0), HSLA350 1.9/1.9, M900 1.5/1.5 and M190 2.0/2.0 suggest that, unlike tensile strengths, no discernable differences can be noticed for fatigue properties for laser welds [Figure 2.3 (a)]. Minor differences noted between various laser welded samples are attributed to differences in gage thickness. The weld fatigue strength seems to be a function of material thickness rather than steel grade and microstructure [12].

Yan and Gallagher [20] note that if severe concavity of greater than 20% is present, fatigue strength is greatly reduced. In the absence of such concavity, Yan and Gallagher noted crack initiation occurring in the HAZ next to the base metal for all fatigue specimens due to high stress concentration in that region; once crack is initiated, it propagated into the base metal.

Work conducted by Anand et al [28] indicates that fatigue limit of uncoated TWB combination was 1.4 times higher than that of the zinc coated TWB's. The lowered fatigue strength of galvanized versions is attributed to the residual tensile stresses generated on the surface of the steel when the molten zinc in the fusion zone solidifies and is further subjected to temper rolling or a skin pass operation for a homogeneous texture. While zinc would alloy with iron in the fusion zone, hard and brittle zinc-iron phases may develop at the interface between the steel substrate and zinc coating during hot dip galvanizing process. Outbursts or local growth of zinc-iron phases at steel grain boundaries and the resulting mismatch between the inhibition layer and the steel substrate may cause cracking. Thus, the fatigue strength of laser welded galvanized steels becomes lower compared to laser welded cold-rolled specimens. Anand et al also note that fatigue crack propagation in the base metal and bare TWB's was mainly characterized by fatigue striations, while the galvanized TWB's exhibited intergranular cracking caused by the presence of zinc penetrating beneath the sheet surface.

Research work published by Tsay et al [29] indicate that formation of lower bainite and tempered martensite in the weld zone and HAZ during welding of D6AC high strength steels (a medium carbon, low alloy steel) with 225°C preheating not only retarded the fatigue crack propagation but also improved Charpy toughness in these regions. However, such a process will result in higher part costs.

References

[1] Bhadeshia, H.K.D.H. TRIP-assisted steels? ISIJ International, Vol. 42 (2002), No. 9, pp. 1059-1060.

[2] Ginzburg, V.B. Metallurgical design of flat rolled steels.

[3] Schaeffler, Dan. Advanced high strength steels: Enhanced formability adds to vehicle strength. http://www.eqsgroup.com/publications/Advanced_High_Strength.pdf)

[4] WorldAutoSteel. DP Steels. http://www.worldautosteel.org/SteelBasics/Steel-Types/Dual-Phase.aspx

[5] ThyssenKrupp (InCar). Complex-phase steels: CP-K / CP-W. http://incar.thyssenkrupp.com/7_01_031_CP_Staehle.html?lang=en

[6] WorldAutoSteel. Martensitic (MS) Steels. http://www.worldautosteel.org/SteelBasics/Steel-Types/Martensitic.aspx

[7] Ohio State U. Hot-stamping boron-alloyed steels for automotive parts. Part II: Microstructure, material strength changes during hot stamping. http://nsmwww.eng.ohio-state.edu/Jan07RDUpdate.pdf)

[8] Feng, Z, Santella, M.L., David, S.A., Steel, R.J., Packer, S.M., Pan, T., Kuo, M. Bhatnagar, R.S. Friction Stir Spot welding of advanced high strength steels – a feasibility study. SAE 2005-01-1248.

[9] Hovanski, Y., Santella, M. Friction stir spot welding of advanced high strength steels II. (http://www1.eere.energy.gov/vehiclesandfuels/pdfs/merit_review_2011/lightweight_materials/lm030_hovanski_2011_o.pdf)

[10] Sklad, P., Santella, M., Hovanski, Y., Grant, G. Friction Stir Spot welding of advanced high strength steels (AHSS) http://www1.eere.energy.gov/vehiclesandfuels/pdfs/merit_review_2008/lightweight_materials/merit08_sklad_2.pdf.

[11] Khan, M.I., Kuntz, M.L., Su, P., Gerlich, A., North, T., Zhou, Y. Resistance and friction stir spot welding of DP600: a comparative study. Science and Technology of Welding Joining (2007), Volume 12, Issue 2, pp 175-182. http://www.mendeley.com/research/resistance-and-friction-stir-spot-welding-of-dp600-a-comparative-study/

[12] Gallagher, M., Yan, B., Nadkarni, G., Polon, M., Aefferer, H., Leidich, H. Laser assembly welding of advanced high strength steels. Adv Laser Appl Conf Exposition 2005; 3; pp 49-62.

[13] Liu, X. -Bo, Yu, G., Pang, M., Fan, J., Wang, H., Zheng, C. Dissimilar autogenous full penetration welding of superalloy K418 and 42CrMo steel by a high power CW Nd:YAG laser. Applied Surface Science, 253 (2007) pp 7281-7289.

[14] Wu, Q., Gong, J., Chen, G., Xu, L. Research on laser welding of vehicle body. Optics and Laser Technology, Vol 40, Issue 2, March 2008, pp 420-426.

[15] Shao, H., Gould, J., Albright, C. Laser blank welding of high-strength steels. Metallurgical and Materials Transactions B, Vol 38B, April 2007, pp 321-331.

[16] Anand D., Chen, D.L., Bhole, S.D., Andreychuk P., Boudreau, G. Fatigue behavior of tailor (laser)-welded blanks for automotive applications. Mater Sci Eng A 2006;420:199–207.

[17] Hartley, B., Ono, M. Laser weldability of dual phase steels in tailored blank applications. SAE Technical Paper Series, 2002-01-0150.

[18] Matsumoto, T., Fukuda, N., Kondo, Y., Ohmori, A., Inoue, K., Arata, Y. Study on prevention of welding defects in high power CO2 laser materials processing. Journal of Laser Applications, Vol 11, Issue 6, 1999.

[19] Laser welding safety concerns. http://www.weldingtipsandtricks.com/laser-welding.html)

[20] Yan, B., Gallagher, M. Strength and fatigue of laser butt welds for IF, HSLA and dual phase sheet steels. Int. Symposium on advanced high strength steels for the ground transportation industry, Mater Sci Technology (MS&T) Vol 2, 2006, pp 87-101.

[21] Han T, Park SS, Kim K, Kang C, Woo I, Lee J. CO2 laser welding characteristics of 800 MPa class TRIP steel. ISIJ Int 2005;45:60–5

[22] Ma, C., Chen, D.L., Bhole, S.D., Boudreau, G., Lee, A., Biro, E. Microstructure and fracture characteristics of spot-welded DP600 steel. Materials Science and Engineering: A Vol 484, Issues 1-2, 2008, pp 334-346.

[23] Xia M., Sreenivasan N., Lawson S., Zhou Y., Tian Z. A comparative study of formability of diode laser welds in DP980 and HSLA steels. ASME Trans 2009;129:446–52.

[24] Sreenivasan, N., Xia, M., Lawson, S., Zhou, Y. Effect of laser welding on formability of DP980 steel. Journal of Engineering Materials and Technology, Vol 130, 2008.

[25] Hirai, K. Formability and dynamic energy absorption of tailored blank with high strength steel sheets. SAE paper 2000-01-2662.

[26] ASTM Standard E643, 2009. Standard test method for ball punch deformation of metallic sheet material. ASTM International, West Conshohocken, PA. www.astm.org.

[27] Saunders, F.I., Wagoner, R.H. The use of tailor-welded blanks in automotive applications. Simulation of Materials Processing, Balkema, Rotterdam, 1995, pp 157-164.

[28] Anand, D., Chen, D.L., Bhole, S.D., Andreychuk, P., Boudreau, G. Fatigue behavior of tailor (laser)-welded blanks for automotive applications. Materials Science and Engineering A, Vol 420, Issues 1-2, 25-March-2006, Pages 199-206.

[29] Tsay, L.W., Chung, C.S., Chen, C. Fatigue crack propagation of D6AC laser welds. Int. J. Fatigue, Vol 19, No. 1, pp 25-31, 1997.

CHAPTER 3. Yb:YAG WELDING OF TRIP780 WITH DUAL PHASE AND MILD STEELS FOR USE IN TAILOR WELDED BLANKS

Paper published in Materials and Design 30 (2009) 4146-4155

Rajashekhar S Sharma and Pal Molian

Abstract

Advanced high strength steels (AHSS) are essential to meet the demands of safety and fuel efficiency in vehicles. In this paper, we present the results of laser welding of two AHSS steels, TRIP780 and DP980. A 2 kW Trumpf TRUDISK 6002Yb:YAG laser beam was utilized to join 1 mm thick TRIP780 with 1.5 mm thick DP980 and 1 mm thick mild steel. Optical metallography was used to characterize the weld profile and microstructures. Microhardness, tensile and fatigue tests were performed to evaluate the mechanical properties. Results indicate that the laser welds exhibit excellent strength and hardness with minimal defects which are attributed to the high beam quality, disk type of laser. In addition, there is a distinct effect of pre-straining of TRIP780 steels on the energy absorption.

3.1 Introduction

With the increases in energy consumption, the fuel prices have been steadily rising all over the world, resulting in higher demands for fuel-efficient vehicles. At the same time, due to increased awareness, consumers are looking for environmentally friendly vehicles that offer higher safety during crashes. As a result of these often conflicting demands, advanced high strength steels (AHSS) are aggressively deployed in automotive industry to reduce weight of the vehicle body and closures panels, while at the same time increasing energy absorption in some areas and stiffness in others. Considerable information on AHSS materials and their properties can be found in literature (for examples, see Refs. [1,2]).

Tailor welded blanks (TWB) is one method of making full utilization of AHSS. TWB's are blanks of differing materials and/or treatments, thicknesses, or surfaces, which are generally welded before the stamping operations are carried out. Since some AHSS steels such as transformation induced plasticity (TRIP) have high strength combined with improved ductility, it may be advantageous to use these steels where energy absorption and high strength characteristics are important, while other materials such as dual phase (DP) steels will need to be used where even higher strengths with reduced ductility are desired. Whether TWB's are used or not, attaching panels made of differing materials such as DP, TRIP and mild steel remains a challenge and a safe and reliable joining process is critical to the success of fuel-efficient vehicles.

In recent years, lasers are efficiently used to join different automobile panels. The lasers offer significant advantages such as high strength, excellent finish, simplicity, flexibility and reliability in manufacturing compared to other processes such as resistance spot welding, gas metal arc welding and electron beam welding. The chief limitation namely cost per watt is rapidly dropping with novel advances in laser technology. Autogenous welding is the most common form of laser welding although in some cases such as when a gap needs to be filled, a suitable filler material may be required.

Research has been carried out to understand the effects of laser welding on AHSS materials. Han et al. [3] butt-welded 800 MPa class TRIP steel using a CO2 laser and found lower porosity at higher welding speeds. However, welding speed did not seem to have a perceptible effect on microhardness values. Gallagher et al. [4] used an Nd:YAG laser to weld HSLA300, DP600, M900 and M1310 steels at various speeds and found that weld tensile strength appeared to be dependent upon steel grade, weld penetration and weld width. However, weld fatigue strength was a function of material thickness rather than steel grade and microstructure. Others [5,6] have found factors such as weld concavity [5] and presence of zinc [6] to be significant in affecting the weld fatigue performance. Formability of the laser welds has also been investigated [7,8] with the ensuing conclusions that strength difference between the parent metals being joined [7] and soft zones formed in the HAZ [8] can be seriously influencing the formability of the joint. Finite element analysis using LS-Dyna software has also been successfully used on laser welding of DP980 steels to simulate the tensile test results for elongation [9] that allows easier prediction of the mechanical properties in the softened HAZ.

New innovations being applied on other materials are also being researched for applications in the welding of AHSS materials. These include hybrid joining techniques such as Laser-MIG welding process [10,11], which can result in cost avoidance by eliminating edge preparation, typical of GMAW arc welding. Other factors such as the stability conditions for the hybrid laser-GMAW welding process [12] or the effect of the shielding gas on the stability of the hybrid Laser-MIG process [13] have not been researched for AHSS materials.

The microstructures obtained in the fusion zone of laser welded AHSS materials are mostly martensitic due to formation of austenite during the welding process and the subsequent high rates of cooling. This has been confirmed by Rizzi et al. [14] who conducted experiments on laser welding of TRIP, DP and martensitic steels. This may not hold true in all cases. For example, Xia et al. [15] used laser welding process on Al-alloyed TRIP steel with a chemical composition of Fe–1.5C–1.73Al–2Mn and found that ferrite was one of the predominant phases in the fusion zone due to the ferrite-stabilizing property of Al. In the HAZ of lower strength steels such as DP600, austenite formation will be higher at closer proximity to the fusion zone and the percentage of martensite in the HAZ decreases with increased distance away from the fusion zone. This has been verified by Yan and Gallagher [5] on DP590 materials. In the HAZ of higher strength materials such as M1310 steels, tempered martensite or ferrite could form resulting in softened regions [4]. When two materials of widely

differing alloy compositions are laser welded, microstructures that emerge depend upon the composition of the fusion zone. This has been reported by Yan and Gallagher [5] who found formation of Widmanstatten Ferrite during welding of DP590 with EDDS (an Interstitial Free material).

A knowledge of the microstructure and mechanical performance of the fusion zone as well as heat affected zone (HAZ) obtained with laser welding is essential to ensure the reliability of the process. In this paper, laser welding of TRIP780 (galvanized) was investigated by autogenously welding it to DP980 (cold rolled) and to mild steel (cold rolled) separately using a high beam quality YAG laser. It was noted that during repair procedures, pre-strained TRIP780 steels might be re-used by welding them to other panels that are undamaged. In order to understand the performance of pre-formed TRIP780 steels, pre-strained strips of TRIP780 were also used in the experiments.

3.2 Experimental Procedure

TRIP780 and mild steel were received in the form of large sheets of 1.0 mm thick, while DP steel was procured with a thickness of 1.5 mm. TRIP780 steel was cold rolled and coated with zinc using galvanized iron (GI) process. DP980 and mild steel were cold rolled without any surface protection. In contrast to DP steels, TRIP steels exhibit high work-hardening rates at higher strains. This workhardening difference is one of the primary reasons for the enhanced formability of TRIP steels, a significant advantage over DP steels. Tables 3.1(a) and (b) list the chemical composition and properties of these steels.

Table 3.1 (a) Chemical compositions (wt%) of DP980, TRIP780 and mild steel used

Steel	C	Mn	Mo	P	S	Si	Cr	Al	B	Ti	V	Nb	Ni	Cu	N
DP980	0.135	2.100	0.350	--	--	0.050	0.150	0.450	0.007	--	--	--	--	--	--
TRIP780	0.190	1.580	--	0.013	0.025	1.600	0.070	0.036	--	0.027	--	0.038	0.020	0.020	
Mild Steel	0.043	0.270	0.002	0.041	0.009	0.021	0.020	0.040	0.000	0.002	0.001	--	--	--	0.007

Table 3.1 (b) Mechanical properties of DP980, TRIP780 and Mild Steel used.

Steel	Yield strength (MPa)	Ultimate strength (MPa)	Elongation (%)
DP980 CR	534	980	12.2
TRIP780 CR	471	792	18
Mild Steel	215	355	37.8

Strips of 75 mm width were cut from parent materials of TRIP780, DP980 and mild steel. Some of the TRIP780 strips were plastically deformed to 10% engineering strain (9.53% true strain) in an Instron Tester to study the effect of pre-straining on the performance of the joints. All samples were milled on the edges to ensure that the gap between the edges remained well within 10% (0.1 mm) recommended in literature for butt welding [5, 7]. Since it is the most common form, butt joint configuration was used in all cases. A Trumpf high power TRUDISK6002 laser beam, delivered from a 6 kW Yb:YAG solid state laser (wavelength: 1030 nm, focal length: 200 mm, focal spot diameter: 0.6 mm) to a robotic arm via fiber optics, was used to weld the samples [Figure 3.1(a).] The samples were held stationary in the fixture as shown in Figure 3.1(b), while the laser beam attached to the robot's end effector moved along the edges of the samples being joined. The laser beam was set perpendicular to the surfaces of the plates being joined. Bead-on-plate technique was initially used to determine the speed at which a laser power of 2 kW would achieve full weld penetration. Before the welding was carried out, the samples were cleaned in acetone to remove any debris and contamination remaining on the edges. After that, they were loaded on the flat surface of the fixture and clamped down while ensuring that the milled edges were firmly in contact against each other. The top plates and the bolts (two used on each side) assured that the plates being welded did not move during the welding operation. Locating scheme as shown in Figure 3.1(b) assured consistency in the location of the samples, which minimized re-adjustment of the starting point of the laser beam and its direction of movement. Argon shielding gas was used at a flow rate of 30 l/min (1.8 cubic m/h) during the welding process, although in industrial practice, the shield gas may not always be used (for example, work carried out in Refs. [4,5] does not use shield gas). The direction of shielding gas flow was set perpendicular to the welding direction, with the nozzle moving synchronously with the laser beam to keep the shielding uniform over the weld pool. The welding was carried out at 2 kW at a constant speed of 70 mm/s (4.2 m/min) while ensuring that full weld penetration was achieved. The weld parameters and material combinations are shown in Table 3.2.

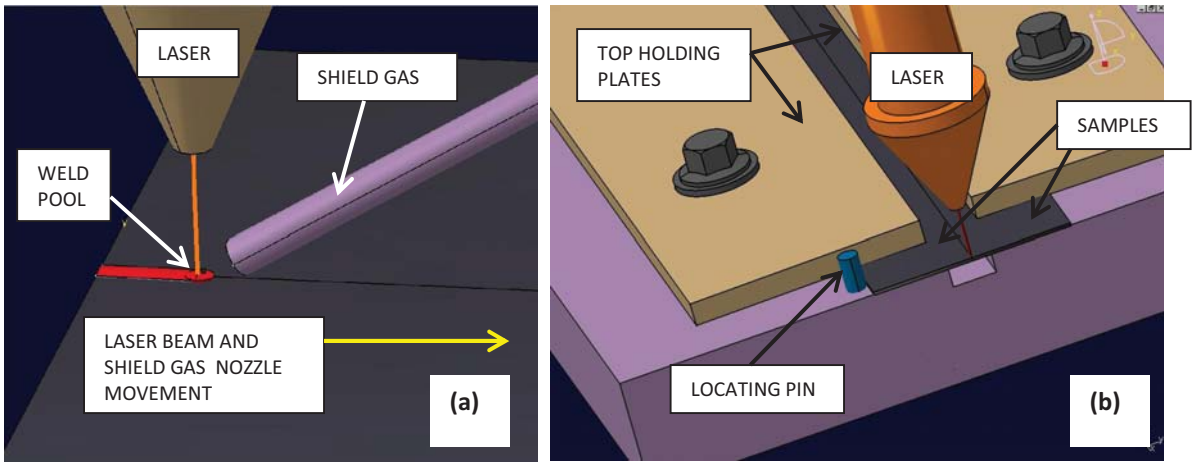

Figure 3.1 (a) Laser set-up and (b) weld fixture adjustment

Table 3.2 Weld scheme

Material 1	Thickness of Material 1	Material 2	Thickness of Material 2	Sample ID number
TRIP780 CR and GI, unstretched	1mm	Mild Steel, Cold Rolled	1mm	1A
TRIP780 CR and GI, 10% stretched	1mm*	Mild Steel, Cold Rolled	1mm	1C
TRIP780 CR and GI, unstretched	1mm	DP980 Cold Rolled	1.5mm	1D
TRIP780 CR and GI, 10% stretched	1mm*	DP980 Cold Rolled	1.5mm	1F

* Thickness before stretching

NOTES:

CR=Cold Rolled, GI = Galvanized Iron

Laser power: 2 kW

Laser beam speed: 70 mm/sec (4.2 m/min)

Focal spot diameter: 0.6mm

Shield gas: Argon

Shield gas flow rate: 30 liters/min (1.8 cubic meters/hour)

After the welding was completed, small samples were cut at a distance of 25 mm away from the edges to eliminate the effects of starting and stopping of the welding operations. They were then mounted in resin, polished and etched with 3% Nital solution for microstructural examination that included optical metallography and microhardness testing. All microhardness values were obtained in HV using a load of 0.3 kN.

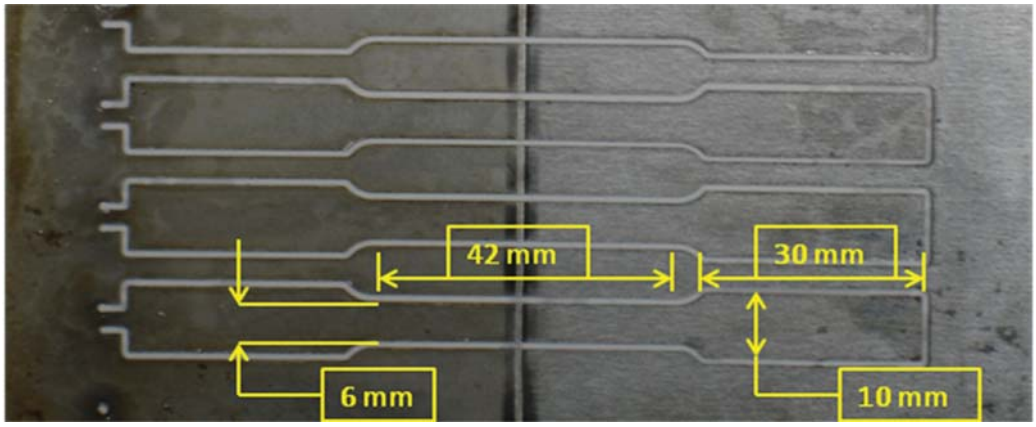

Figure 3.2 Coupon of TRIP-0 welded to mild steel (TRIP-0:MS) and tensile samples cut using high pressure hydro jet. Major nominal dimensions are shown.

Further, tensile test samples 10 mm wide at the grip and 6 mm in the mid region, as shown in Figure 3.2, were prepared using high pressure hydro-jet cutting operation. Measurements of the cut samples showed that all samples were within 6.0 ± 0.25 mm. Statistical analysis showed that the standard deviation of the sample width at the weld point was 0.08 mm, with an average width of 6.04 mm. All tensile testing was carried out in a direction perpendicular to the weld. Also, the direction of tensile load was set to be perpendicular to the direction of elongation in the TRIP-10 steel. Tensile testing was carried out on Instron Tester and stress–displacement graphs were obtained using five to six samples for each combination. Fractured surfaces of TRIP780 steel were examined using scanning electron microscope (SEM) to understand the ductile and brittle fracture modes. Fractured surfaces of mild steel were not studied as these are well known. Finally a few fatigue tests were conducted on samples of TRIP-0 steel welded to mild steel using a MTS fatigue testing machine.

3.3 Results and discussion

3.3.1 Microstructure and microhardness of TRIP780 and DP980 base metals

Microstructural examination of un-stretched TRIP780 base metal (referred to as TRIP-0) versus 10% stretched TRIP780 steel (TRIP-10) showed that the TRIP effect was successful in increasing the hardness of the base metal from 240–260 HV to 310–320 HV. Optical micrographs of the base metal of TRIP-0 and TRIP-10 as well as DP980 are shown in Figure 3.3. The microstructure of TRIP780 consists of soft ferrite matrix with grain boundary retained austenite and martensite (dark spots). The various levels of these phases give TRIP steels their unique balance of properties. The increase in hardness is attributed to the plastic-strain induced transformation of retained austenite to martensite. During pre-straining, the retained austenite transforms to martensite, leading to volume and shape changes within the microstructure. DP steels have a microstructure of

mainly soft ferrite, with islands of hard martensite dispersed throughout. The strength level of these grades is related to the amount of martensite in the microstructure.

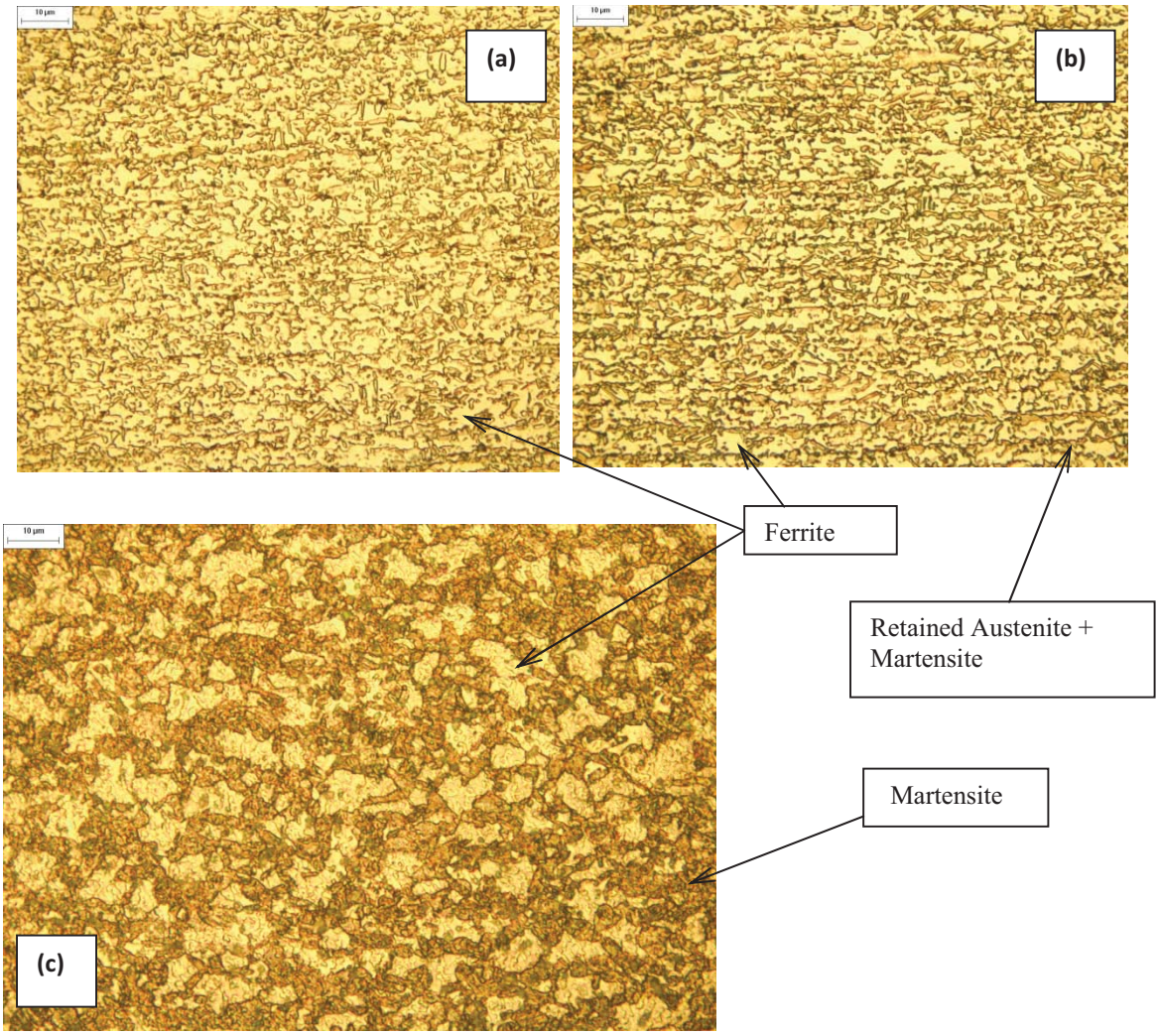

Figure 3.3 Microstructure of base materials used. (a) TRIP steel, un-stretched, at 1000X, showing retained austenite and martensite (red) in a matrix of soft ferrite (yellow). (b) TRIP steel, stretched to 10% engineering strain, 1000X. (c) DP980 base metal, 1000X, with martensite (red) in a matrix of soft ferrite (yellow).

3.3.2 Fusion and heat affected zones

The weld profiles obtained in the laser welding are illustrated in Figure 3.4. At the speed of 4.2 m/min, the fusion zone exhibits hour-glass configuration with a concave shape at the bottom. The gravitational forces acting upon the liquid metal caused the concave shape. Considerable variability in the hour-glass shape can be expected if laser power, welding speed and flow rate of the shield gas were varied. The small variation in the

hour-glass shape of the fusion zones is believed to be an effect of material and thickness changes. The monochrome photographs of Figure 3.4 clearly show the HAZ for various cases. While TRIP steels welded to mild steels showed about equal sized regions of HAZ, DP980 steels welded to TRIP steels showed larger HAZ in the DP980 base metal, as shown in Figure 3.4(b).

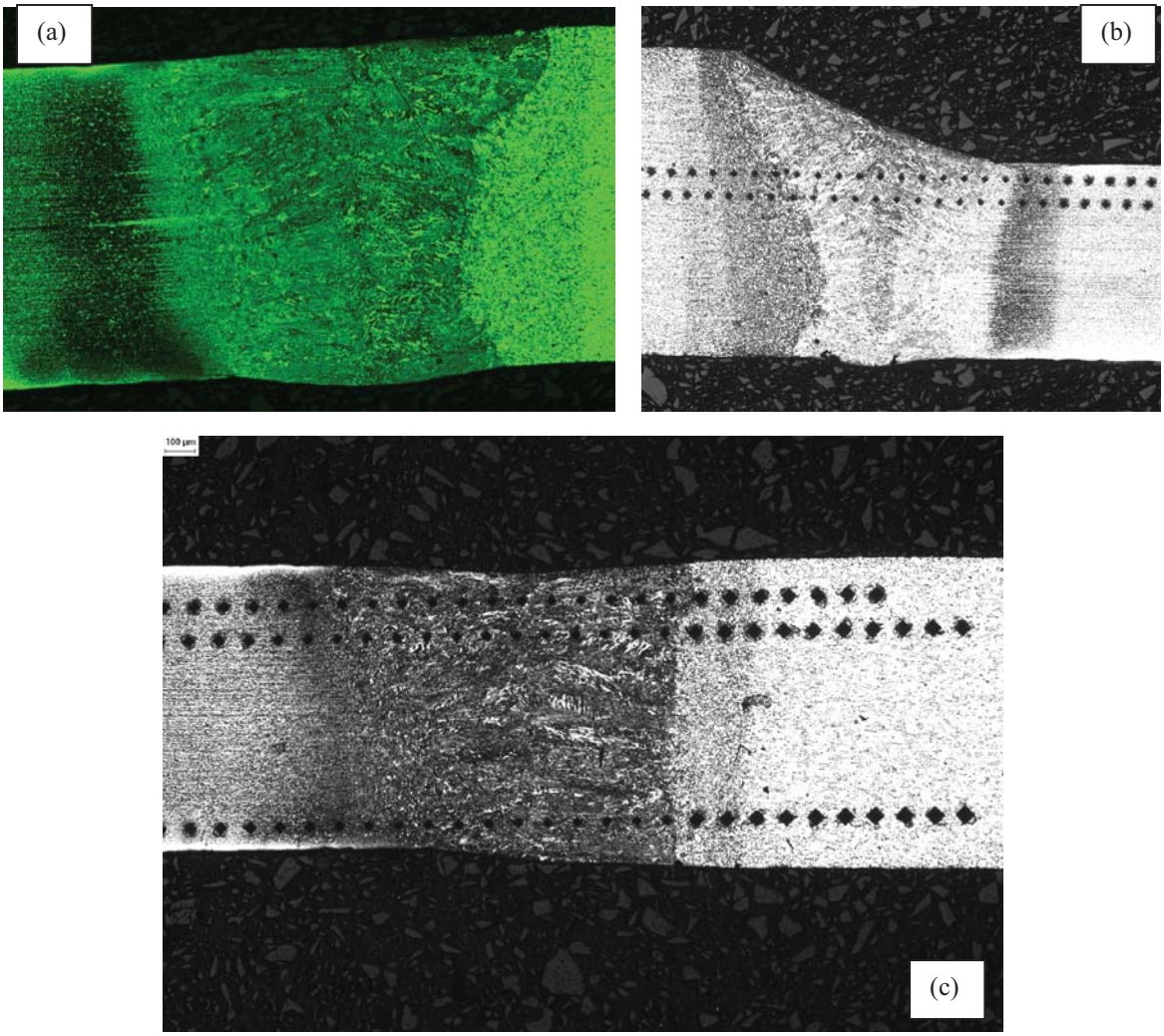

Figure 3.4 Shapes obtained during the welding process using optical microscope, shown without color to improve clarity. (a) Micrograph of TRIP-0 welded to MS showing hourglass configuration in the fusion zone shown at 50X. MS base metal is shown on the left and TRIP-0 shown on the right. (b) Micrograph of TRIP-10 welded to DP980 steel, shown at 50X. The hour glass is still present, and the concave shape in the bottom is evident. (c) Picture of TRIP-10 welded to mild steel, still exhibiting an hour-glass shape but to a much lesser extent. Note the microhardness indentations shown in (b) and (c).

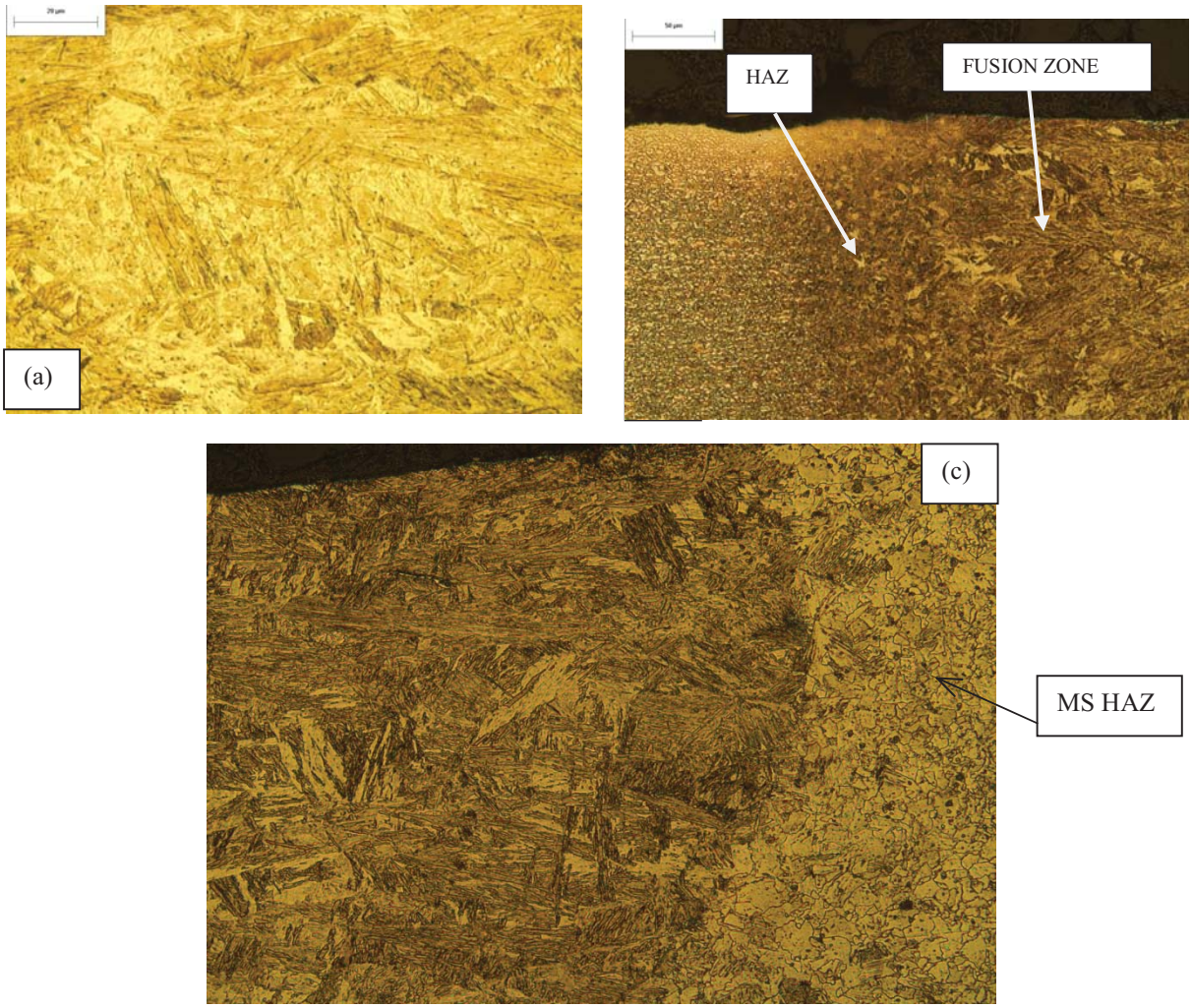

Figure 3.5 Microstructures in TRIP780 steels welded to MS, 3% Nital etched. (a) TRIP-0 welded to MS, 1000X. (b) TRIP-10 welded to MS showing TRIP780 base metal and HAZ near the top of the weld, 400X. (c) TRIP-10 welded to MS showing fusion zone and mild steel's HAZ near the top of the weld, 400X.

3.3.3 Microstructure and microhardness

The microstructures obtained in TRIP steels welded to MS are shown in Figure 3.5. The microstructure is predominantly martensite with small areas of ferrite present throughout the fusion zone. Weld defects such as cracks were prominently absent. Figure 3.5(a) shows the microstructure in the TRIP-0 samples welded to mild steel (TRIP-0:MS), which showed hardness in the range 480–510 HV. The HAZ in the TRIP steel, adjacent to the fusion zone, is shown in Figure 3.5(b), while the HAZ in MS is shown in Figure 3.5(c). Nital etching seems to have darkened the HAZ of TRIP steel considerably more compared to the fusion zone and the HAZ of MS base metal. The mild steel region showed a larger HAZ with higher values of microhardness.

Figure 3.6 shows microstructures obtained in TRIP steels welded to DP980. The hour-glass shape is evident in both TRIP-0:DP as indicated by Figure 3.6(a) and TRIP-10:DP fusion zone as shown in Figure 3.6(b). Both micrographs show clear concave shape at the bottom of the fusion zones. The microstructure of the fusion zone for TRIP-10:DP near the bottom of the fusion zone near TRIP-10's HAZ is shown in Figure 3.6(c) at 1000X. The microstructure is predominantly martensitic with islands of ferrite, and exhibited hardness values in the region of 500 HV.

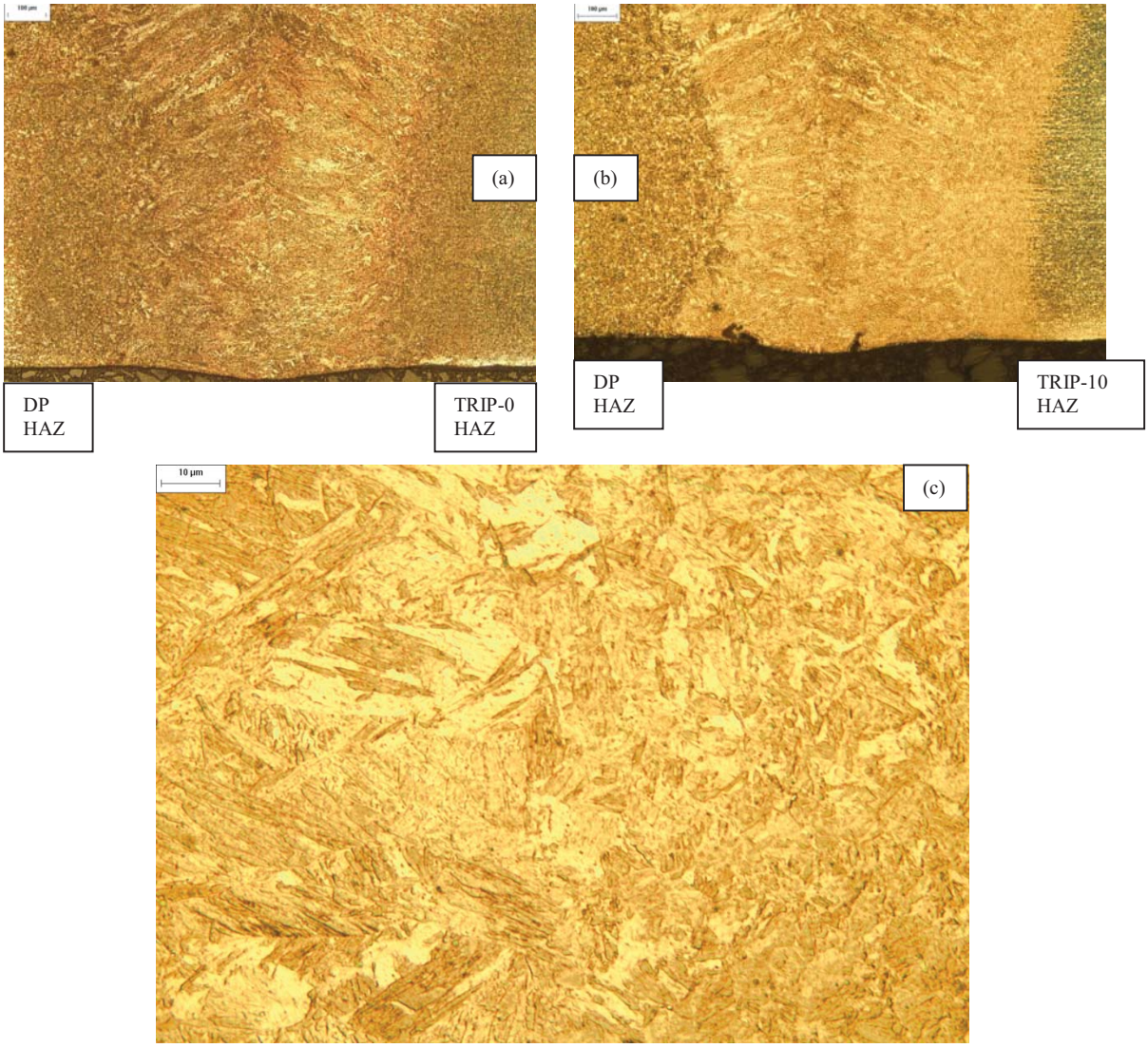

Figure 3.6 Microstructures in TRIP780 steels welded to DP980, 3% Nital etched. (a) TRIP-0 welded to DP980 showing bottom of the fusion zone and HAZ of both TRIP-0 and DP980, 100X. (b) TRIP-10 welded to DP980 showing bottom of the fusion zone and HAZ of DP980 on left and HAZ of TRIP780 on right, 100X. (c) TRIP-10 welded to DP980 showing fusion zone near bottom, just left of TRIP steel's HAZ, 1000X.

Microhardness evaluations of the weld zone, HAZ and base metal were carried out for all cases. Figure 3.7 shows microhardness data for TRIP-0 samples welded to mild steel (TRIP-0:MS) at several depths, as shown in Figure 3.7(a), to determine if there is considerable variability of hardness with depth. As shown in Figures 3.7(b)–(d), the hardness values are quite consistent in the fusion zone, although higher values of hardness are observed in the upper area of the fusion zone compared to the lower regions. Data analysis carried out, assuming a normal distribution and using t-test, suggests that statistically, the microhardness values in the top row of the fusion zone are higher compared to those in lower rows. This analysis is shown in Table 3.3, indicating that the null hypothesis is rejected for both levels of confidence (a) for the top row versus the third row from the top, while it cannot be rejected for the third row versus the second row from the bottom. The higher values of the microhardness in the top of the fusion zone are attributed to higher rates of cooling achieved due to convection currents that result from shield gas flow.

Table 3.3 Hypothesis testing for microhardness values

Set up H_0: $X_1 \leqq X_2$ or $X_1 - X_2 \leqq 0$
H_1: $X_1 > X_2$

Where H_0 = Null Hypothesis
H_1 = Alternative Hypothesis

$$t_{calc} = \frac{\bar{X}_1 - \bar{X}_2 - \delta_0}{\sqrt{(s_1^2/n_1^2 + s_2^2/n_2^2)}}, \quad \delta_0 = 0$$

$t_{v=21}$ = 1.721 at α = 0.05
2.831 at α = 0.005

$t_{v=18}$ = 1.734 at α = 0.05
2.878 at α = 0.005

Row	Mean	Standard Deviation	Sample Size	t_{calc}	Reject H_0 at 99.5%?	Reject H_0 at 99.95%?
Top row	$\bar{X}_1$ = 502.9	S_1 = 17.9	n_1 = 13	5.8980	Yes	Yes
Third row from top	$\bar{X}_2$ = 493.1	S_2 =9.3	n_2 = 10			
Third row fromtop	$\bar{X}_2$ = 493.1	S_2 =9.3	n_2 = 10	0.1733	No	No
Second row from bottom	$\bar{X}$3 = 492.8	S_2 =14.6	n_2 = 10			

The microhardness data measured for TRIP-0:MS combination are summarized in Table 3.4. Although the standard deviation values are high, in general, the microhardness values in the TRIP steels welded to mild steel are around 490 HV in the fusion zone. This confirms that the structure is mostly martensitic. Typical microhardness values observed with the other combinations are presented in Figure 3.8. Fusion zone in the TRIP-10 welded to mild steel (TRIP-10:MS) exhibited microhardness values similar to TRIP-0:MS combination. This is expected because the effects of prior straining will disappear by laser melting and the chemical analysis as well as the rate of cooling would be similar to TRIP-0:MS. On the other hand, the fusion zones of TRIP steels welded to DP980 exhibited microhardness values much higher, in some instances as high

as 600 HV. The fusion zone of TRIP780:DP980 will be richer in chromium (Cr) compared to the fusion zone of TRIP780:MS, since both DP980 and TRIP780 contribute Cr. This results in a general increase in the hardness. Furthermore, the presence of Ni also reduces the grain size. The effect of all of these is increased hardness in the fusion zone of TRIP780:DP980 combination compared to TRIP780:MS fusion zone.

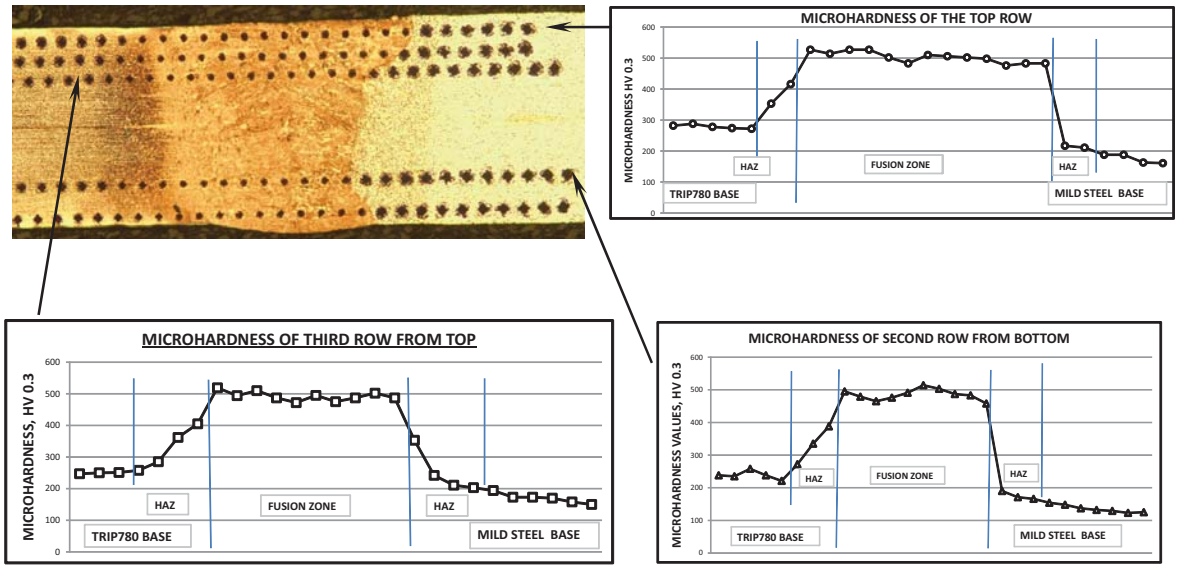

Figure 3.7 Microhardness evaluations in TRIP-0 samples welded to mild steel at 70 mm/s. The hardness in the fusion zone and HAZ is consistent from row to row, although slightly higher hardness values were noticed in the top than in the bottom, presumably due to higher rates of cooling in the top region.

A closer examination of Figures 3.7 and 3.8 suggests that there could be a slight softening of HAZ in TRIP-0 and TRIP-10 steels. On the other hand, the softening of HAZ zone in DP980 area is significantly higher. This phenomenon has been subject to some controversial observations. Gallagher et al. did not find any such softening in laser welded DP600 [4]. However, Wu et al. [16] investigated welding of DOGAL (DP800) to BUSD (mild steel), but reported the softening phenomenon. Gallagher et al. reports that the local softening in the HAZ has occurred only in very high strength steels such as M900 martensitic steel [4]. This suggests that if DP980 is welded to DP980 using the same process, HAZ would be indeed soft and fracture is likely to occur in the HAZ during tensile testing. This has been reported by Panda et al. [9] who conducted tensile and formability tests on DP980 steels. It should be noted from Figure 3.7(c) that the softened HAZ in DP980 has microhardness values similar to that for TRIP780 steel. Since microhardness values can be related to tensile strengths [17], it can be expected that the fractures could occur either in the HAZ of DP980 or TRIP780 steels, or in the TRIP780 base metal. On the other hand, the HAZ in mild steel region exhibited much higher microhardness values of 200 HV or higher compared to about 150 HV in the base metal. For this reason, welding of AHSS materials such as DP600 or TRIP780 to mild steel will not adversely affect the tensile strength of the joint when compared to the base metal properties, but in fact may actually improve it.

The softening of DP980 and the considerable differential in the microhardness values between the fusion zone, HAZ and base metal are not suitable for the formability of the steels. Xia et al. [8] conducted limiting dome tests on samples of DP980 and HSLA steel and reported that high differentials in hardness across the weld resulted in early fractures in the softened HAZ during metal forming.

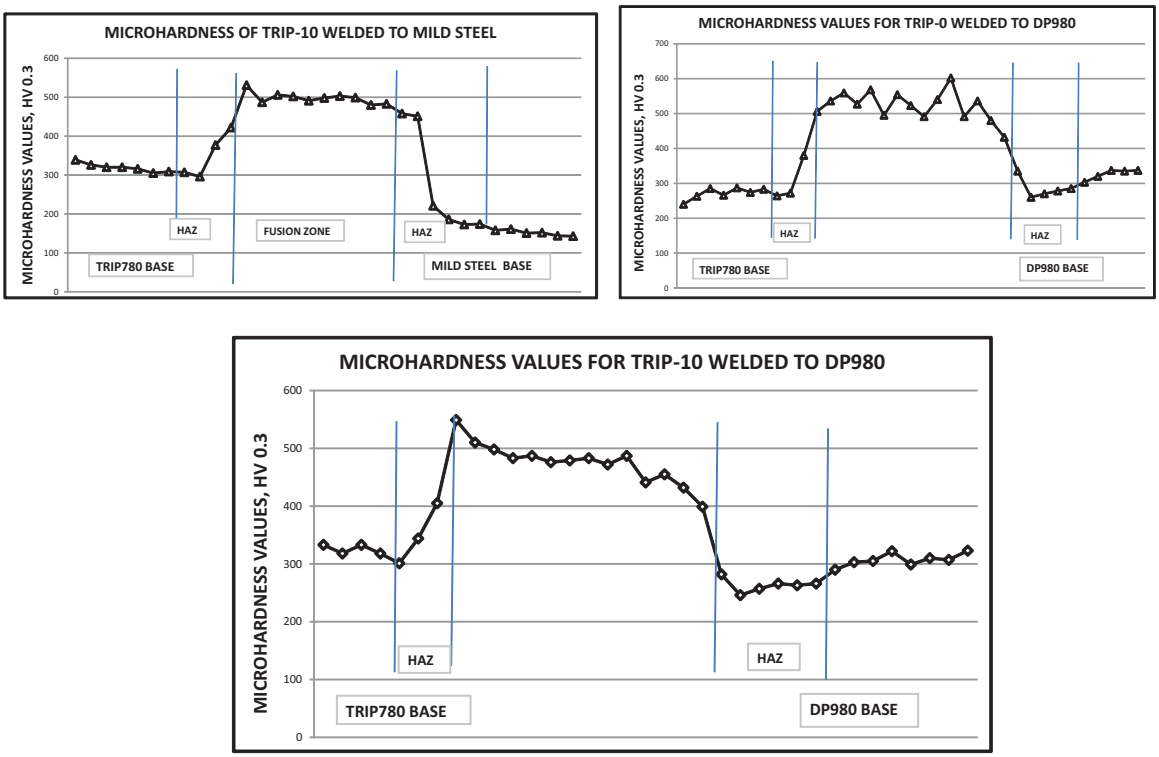

Figure 3.8 Typical microhardness values observed in other material combinations are shown.

Table 3.4 Microhardness values observed in TRIP-0:MS

	TRIP steel			Mild Steel	
	Base metal hardness	HAZ hardness	Fusion zone hardness	Base metal hardness	HAZ hardness
Mean	258	358	493	156	216
Standard deviation	15	52	18	21	47

3.3.4 Tensile tests

Figure 3.2 shows part of the coupon with tensile samples cut using the hydro-jet operation. The figure also shows the major nominal dimensions programmed into the CNC for the sample cutting process. Dimensional

analysis of samples cut indicated that the sample dimensions were consistent with all sample widths falling in the 5.75–6.25 mm range.

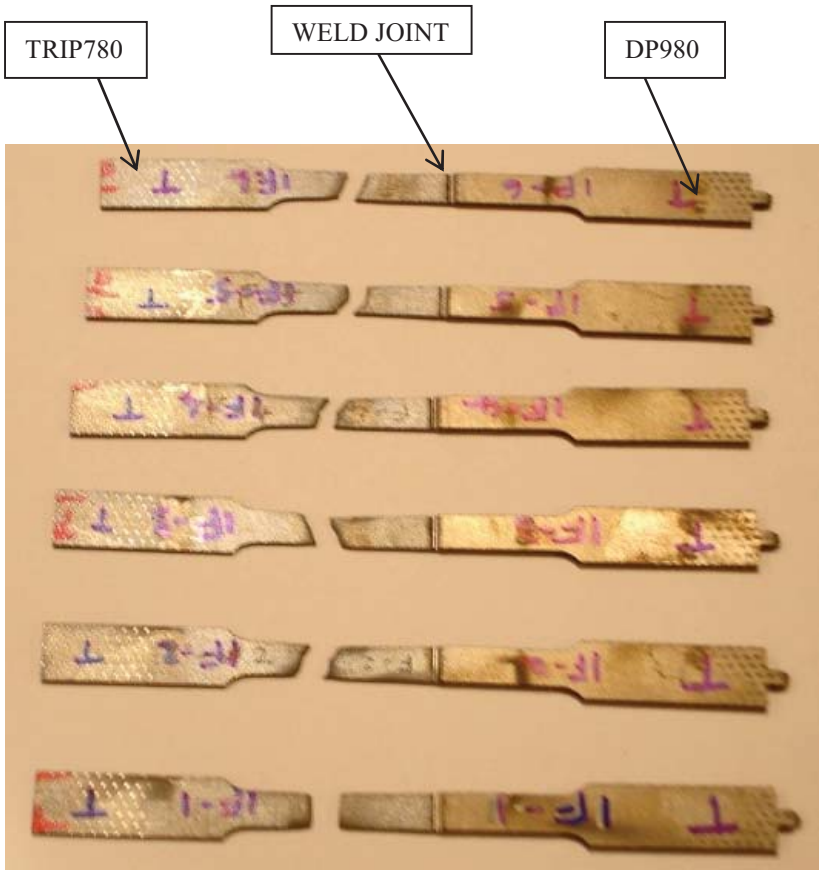

Figure 3.9 Tensile test samples of TRIP-10 welded to DP980 showing fracture zone away from the weld.

Tensile tests were carried out for all the combinations studied. For both the TRIP–MS combinations, all fractures occurred in the base metal area of the mild steel, while for both the TRIP–DP combinations, fractures occurred in the base metal region of TRIP steel. The fracture tendency can be directly correlated to the microhardness values which are always higher in the HAZ and fusion zones compared to the base metal values. The tests also confirmed that the minor softening of the HAZ in TRIP–DP combinations was insignificant. Also, if the welded region had showed significantly reduced cross sectional areas, we could have seen fractures in the HAZ or fusion zones. However, drastic reductions in cross-sections were not noted in any cases. All fractures occurred about half way from the weld region to the transition region to the grip area. Some of the fractured samples are shown in Figure 3.9.

The tensile test data is summarized in Table 3.5 with stochastic parameters of mean and standard deviation values for maximum deflection at fracture, maximum true stress achieved and maximum true strain at fracture. Calculations were carried out for the joint of an initial length of 42 mm. Variations in the sample dimensions were accounted for during the calculations. For example, in the case of TRIP-10:DP combination, the thickness of the fractured TRIP base metal was initially at 0.93 mm that was used to calculate the stress values. As can be seen from Table 3.5, for the two TRIP:MS combinations, all fractures occurred at an engineering stress of 375–385 MPa or true stress of 396–408 MPa; this indicates that the TRIP base metal, which has a yield strength of 435 MPa, did not reach the yield point in the traditional sense, although some local yielding might have occurred in the TRIP base metal. Thus the elongations of the joint occurred primarily in the mild steel region. Since little yielding can be expected in the TRIP base metal region for the TRIP:MS combinations, the maximum elongations achieved for the two mild steel cases are similar. On the other hand, for the TRIP–DP combinations, engineering stress of about 811–870 MPa was reached before fracture occurred in the TRIP steel's base metal area. Since the yield point of DP980 is about 560 MPa, it can be expected that the total strain in the TRIP–DP combinations consisted of some elongation in the DP980 regions. It can also be noted from Table 3.5, that the total deflection as well as true strain values for TRIP–MS combinations are much higher than those for the TRIP–DP combinations. This result is not surprising since the mild steel has an elongation of 38% compared to 18% for TRIP780 and 12% for DP980 steels.

Table 3.5 Results of tensile tests

Material combination	Sample size	Statistics	Max deflection @ fracture, mm	Deflection at max engrg stress, mm	Max load (at max engrg stress), kN	Maximum engrg stress achieved, MPa	Maximum engrg strain	Maximum true stress achieved, MPa	Maximum true strain
TRIP-0 to Mild Steel	5	Mean	9.275	5.569	2.244	375.38	0.221	395.44	0.199
		Standard Deviation	1.523	1.355	0.014	2.40	0.036	2.65	0.029
TRIP-10 to Mild Steel	6	Mean	9.128	5.397	2.325	380.77	0.217	401.85	0.197
		Standard Deviation	0.408	0.541	0.007	1.65	0.010	1.78	0.008
TRIP-0 to DP980	6	Mean	5.952	4.728	4.774	803.88	0.142	895.25	0.133
		Standard Deviation	0.174	0.109	0.024	5.36	0.004	6.33	0.004
TRIP-10 to DP980	6	Mean	5.013	3.478	4.782	838.53	0.119	934.02	0.113
		Standard Deviation	0.369	0.243	0.043	8.90	0.009	10.13	0.008

From Table 3.5, it can be seen that the true strain in the TRIP–MS cases is much higher than in the TRIP–DP cases. This is expected as the mild steel is considerably more ductile than TRIP780 steel. Another interesting observation noted is that the variability for the TRIP-10:DP samples was much higher than that for the TRIP-0:DP samples. On the other hand, the tensile tests for TRIP-10:MS samples showed lower variability compared to TRIP-0:MS samples. This indicates that the TRIP effect has not been uniform in the TRIP-10 samples that are stretched to 10% engineering strain. On the other hand, in the TRIP:MS samples which always fractured in the mild steel region, strengthened TRIP-10 samples result in less plastic deformation and therefore TRIP-10:MS samples showed less variability compared to TRIP-0:MS samples.

Typical load–displacement diagrams for all four cases are presented in Figure 3.10. As can be seen, for the TRIP:MS cases, the graphs are identical, but the total elongation achieved in TRIP-10:DP is significantly lower than that in the TRIP-0:DP980 combination. Since the total energy absorbed is represented by the area under the load–deflection curve and the two TRIP:DP combinations fracture at about the same load, it can be surmised that TRIP-10:DP cases absorb much lower energy than TRIP-0:DP combination. Statistical hypothesis testing (shown in Table 3.6) was utilized to confirm that the energy absorption for the TRIP-10:DP samples is much lower compared to that for the TRIP-0:DP samples; this infers that when pre-stretched TRIP steel is repaired by welding to a much stronger material, the energy absorption will be significantly reduced; this factor must be kept under consideration during repair of vehicle bodies.

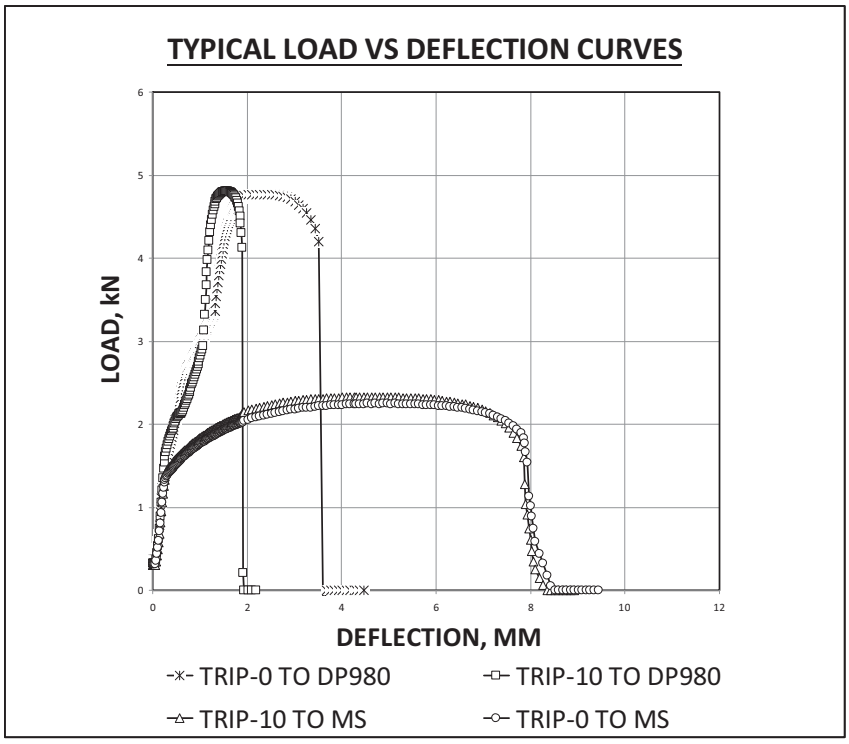

Figure 3.10 Typical load versus deflection curves for all the combinations studied.

Table 3.6 Hypothesis testing for maximum deflection (H_0: No difference between treatments)

Treatment	Mean	St Dev	Sample size	t_{calc}	Reject H_0 at $\alpha = 0.05$?	Reject H_0 at $\alpha = 0.005$?
TRIP-0:DP	5.952	0.174	$n_1 = 6$	13.8099	Yes	Yes
TRIP-10:DP	5.013	0.369	$n_2 = 6$			

$t_{v=10} = 1.812$ at $\alpha = 0.05$

$t_{v=10} = 3.169$ at $\alpha = 0.005$

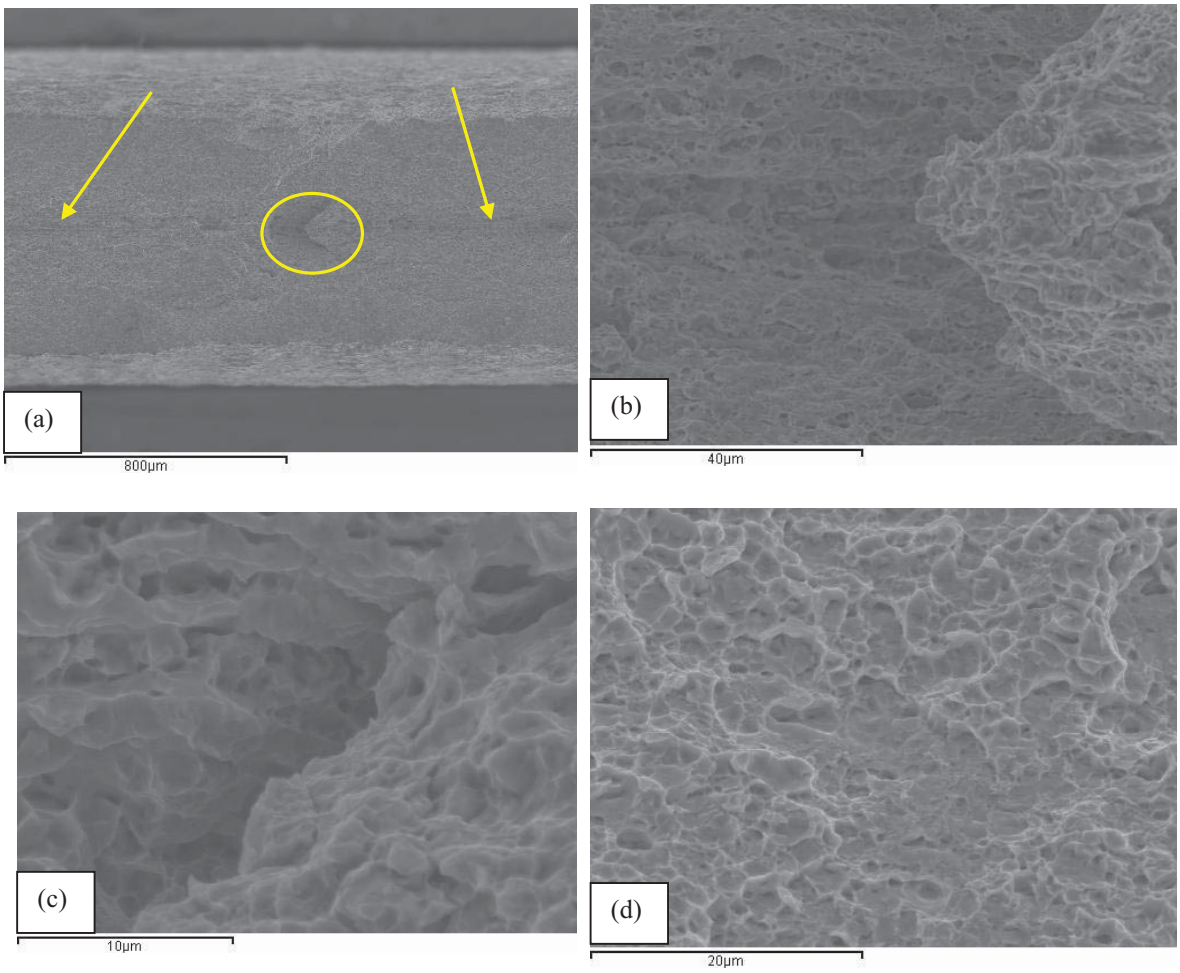

Figure 3.11 SEM micrographs of the fractured zones of the TRIP steel for the TRIP-10:DP980 combination. (a) Typical horizontal fracture zone shown in the middle of the sample (80X) indicated by the yellow lines. Such a fracture zone was observed for all TRIP–DP combinations. (b) Details in the area circled in (a) showing a bright spot and areas of fracture (1300X). (c) SEM micrograph within a similar bright zone at 3000X showing some areas of brittle fracture in the bright zone. (d) SEM micrograph at 5000X outside the bright zone showing almost entirely ductile fracture.

3.3.5 SEM examination of TRIP780 fractured surfaces

The fractured TRIP surfaces from several samples of both the TRIP–DP combinations were examined in the scanning electron microscope. All the samples exhibited a fracture line along the width of the sample, as shown in Figure 3.11(a), from which the fracture seems to have been initiated. All the samples also exhibited bright spots such as shown circled in Figure 3.11(a), shown at higher magnification in Figure 3.11 (b), which also shows clearly the fracture zone running along the width of the sample. Closer examination of the bright spot showed that this area consisted of both brittle and ductile fracture zones as shown in Figure 3.11(c), while

areas just left of the bright zone consisted of cup and cone structure which indicates ductile fracture as shown in Figure 3.11(d). Quantitative energy dispersive spectral analysis was carried out in the bright spot as well as the region just left of the bright spot, and is shown in Figure 3.12. Higher percentage of carbon in the bright spot (11.65 at%) was observed compared to the regions left of the bright spot (6.96 at%). Thus, the quantitative analysis coupled with the existence of brittle fracture zones in the bright spots confirms that the fracture could have initiated in the bright spots along the width of the sample, which then propagate along the whole width and then fracture occurs.

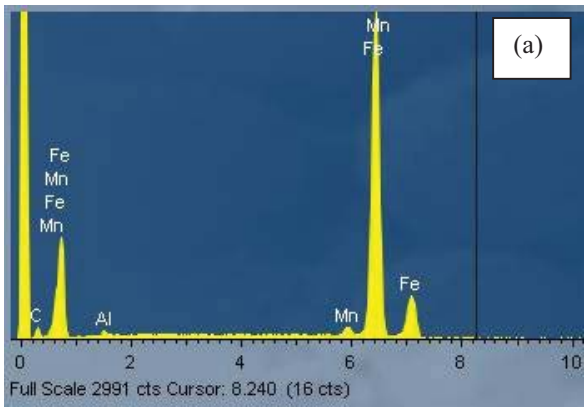

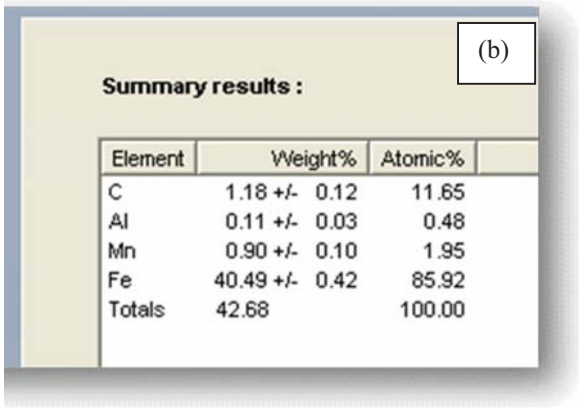

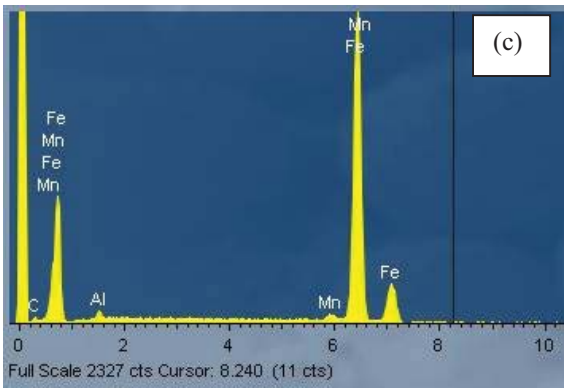

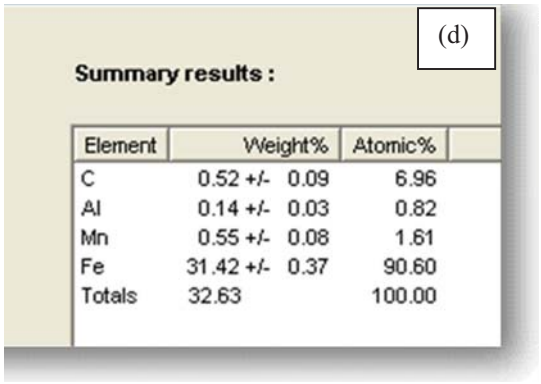

Figure 3.12 Spectral analysis from the SEM (a) and (b) show spectral analysis and Quanta for the bright spot of the sample shown in Figure 3.11, while the spectral analysis and Quanta for the darker region just left of the bright spot of Figure 3.11 are shown in (c) and (d). Note the lower carbon content in the darker region (d), compared to the bright spot in (b).

3.3.6 Fatigue test results

Preliminary fatigue tests were carried out on TRIP-0:MS combination samples using the tensile test samples. Data shows that stress versus number of cycles (S–N) graph remained flat with run-out of 106 cycles achieved for mean stress values of up to 320 MPa for R0.1 set-up, where R0.1 carries a value of 0.1 for the ratio of minimum to maximum stresses applied. For high stress values of 370 MPa, fracture occurred in the mild steel region after 100–150 cycles (low cycle) with ductile fracture. Yan and Gallagher [5] reports that the weld fatigue failure in AHSS is a crack propagation process rather than crack initiation process. For butt welds, absence of crack-like features such as noted in all our combinations, means crack propagation theory may not apply. In addition to this, a severe weld concavity of more than 20% might result in initiation of cracks in the HAZ and its propagation into base metal. In cases where such weld defects are absent, the base metal strength might determine the fatigue life of the joint. This explains the reason why no fatigue failures were noted in the HAZ during our fatigue testing of TRIP-0:MS samples. Anand et al. [6] have concluded that the fatigue strength is compromised by the presence of molten zinc in the fusion zone. Their findings indicate that the fatigue limit of the bare TWB's can be 1.4 times higher than those of galvanized TWB's. This leads to the possibility of fatigue fractures occurring in the fusion zone of the TRIP:DP combinations. In the case of TRIP:MS combination, the initial tensile strength of the fusion zone would be significantly higher than that of mild steel, which would lead to early fractures in the mild steel base metal for high load, low cycle fatigue. For this reason, no fractures could be expected in the fusion zone of the TRIP:MS combination.

3.4 Conclusions

The experimental work presented in this paper confirms that high quality, excellent laser welds can be achieved in joining of TRIP780 to mild steel and DP980, which can be successfully used for applications such as tailor welded blanks. Following are the principal results obtained:

(1) The fusion zone was free of defects such as cracks, porosity, voids, inclusions and others.
(2) High microhardness values were obtained in all the fusion zones, although the values reached in the TRIP:DP combinations were higher than those achieved in the TRIP:MS combinations.
(3) Evidence that suggests that the hardness values in the top is higher than elsewhere in the fusion zone.
(4) Some softening of the heat affected zone (HAZ) was noted in the DP980 base metal regions; however, it did not affect the outcome of the tensile tests for the combinations tested.
(5) Tensile tests indicated that most elongations for the TRIP:MS combinations are due to the mild steel region. However, for the TRIP:DP combinations, considerable plastic deformation has occurred due to the TRIP region.

(6) The strength/elongation analysis reveals that energy absorption of stretched TRIP steels welded to higher strength steels will be lower than un-stretched TRIP steels welded to similar steels. This is true although the direction of stretching is perpendicular to the direction of loads.

(7) Examination of the TRIP780 fractured samples using SEM indicates that there is a fracture line running along the width of the sample, consisting of areas of higher brittleness.

(8) It is hypothesized that the weld regions of TRIP:MS combinations would provide excellent formability properties. In contrast, the formability of TRIP:DP combinations could be poor due to the expected fracture in the HAZ of DP980 base metal.

(9) Fatigue tests show that TRIP:MS combinations exhibited excellent fatigue life, with fractures occurring in the base metal region of mild steel at values approaching the tensile strength of mild steel.

Acknowledgements

The authors wish to thank Ford Motor Company in general for their support. In particular, Matt Zaluzec, John Bonnen, James Boileau, Ron Cooper, Brian Sullivan and Shirleen Holland of Ford Motor Company are thanked for their invaluable help and support. Thanks are also due to Benda Yan and Matt Gallagher of Arcelor Mittal for providing the TRIP and DP materials and Raj Mohan Iyengar of Severstal Inc. for providing mild steel material. The invaluable help of Juergen Stollhof, David Havrilla and Hans Leidich of Trumpf Inc. in getting the samples welded is also gratefully acknowledged.

References

[1] Gope N, Rout DK, Mukherjee S, Jha G, Bhagat AN, Verma AK, et al. High strength steels for automotive applications: recent trends and experience at Tata steel. SAE Trans 2005;26:333–44.

[2] Bhadeshia H, Honeycombe R. Steels: microstructure and properties. Oxford (UK): Butterworth-Heinemann; 2006.

[3] Han T, Park SS, Kim K, Kang C, Woo I, Lee J. CO2 laser welding characteristics of 800 MPa class TRIP steel. ISIJ Int 2005;45:60–5.

[4] Gallagher M, Yan B, Nadkarni G, Polon M, Aefferer H, Leidich H. Laser assembly welding of advanced high strength steels. Adv Laser Appl Conf Exposition 2005;3:49–62.

[5] Yan B, Gallagher M. Strength and fatigue of laser butt welds for IF, HSLA and dual phase sheet steels. In: International symposium on advanced high strength steels for the ground transportation industry. Mater Sci Technol (MS&T), vol. 2; 2006. p. 87–101.

[6] Anand D, Chen DL, Bhole SD, Andreychuk P, Boudreau G. Fatigue behavior of tailor (laser)-welded blanks for automotive applications. Mater Sci Eng A 2006;420:199–207.

[7] Shao H, Gould J, Albright C. Laser blank welding of high-strength steels. Metall Mater Trans 2007;38:321–31.

[8] Xia M, Sreenivasan N, Lawson S, Zhou Y, Tian Z. A comparative study of formability of diode laser welds in DP980 and HSLA steels. ASME Trans 2009; 129; 446–52.

[9] Panda SK, Sreenivasan N, Kuntz ML, Zhou Y. Numerical simulations and experimental results of tensile test behavior of laser butt welded DP980 steels. ASME J Eng Mater Technol 2008;130:041003-1:9.

[10] Koganti Ramakrishna, Angotti Sergio, Joaquin Armando, Eric Stiles. Laser hybrid welding of aluminized coated boron steel for automotive body construction. SAE technical paper series 2008-01. p. 1112–9.

[11] Zhongjie L, Muneharu K, Liquan S. CO2 laser-MAG hybrid welding of 590 MPa high strength steel – study on laser-arc hybrid welding of high strength steel (report 1), vol. 24. Tokyo (Japan): Quarterly Journal of Japan Welding Society; 2006. p. 17–25.

[12] Campana G, Fortunato A, Ascari A, Tani G, Tomesani L. The influence of arc transfer mode in hybrid laser-MIG welding. J Mater Process Technol 2007;191:111–3.

[13] Tani G, Campana G, Fortunato A, Ascari A. The influence of shielding gas in hybrid laser-MIG welding. Appl Surf Sci 2007;253:8050–3.

[14] Rizzi P, Bellingeri S, Massimino F, Baldissin D, Battezzati L. Microstructures in laser welded high strength steels. In: The 13th international conference on rapidly quenched and metastable materials, vol. 144; 2009. p. 1–4.

[15] Xia M, Tian Z, Zhao L, Zhou YN. Fusion zone microstructure evolution of Al alloyed TRIP steel in diode laser welding. Mater Trans 2008;49(4):746–53.

[16] Wu Q, Gong J, Chen G, Xu L. Research on laser welding of vehicle body. Opt Laser Technol 2008;40:420–6.

[17] Shigley J, Mischke C, Budynas R. Mechanical engineering design. New York: McGraw Hill Higher Education; 2004.

CHAPTER 4. GEOMETRIC VARIABILITY AND SURFACE FINISH OF WELD ZONES IN Yb:YAG LASER WELDED ADVANCED HIGH STRENGTH STEELS

Paper published in SME Journal of Manufacturing Processes, 12 (2010) 73-84

Rajashekhar S Sharma, Pal Molian and Frank Peters

Abstract

Laser welding is used for joining advanced high strength steels (AHSS) to improve formability and performance. In this paper, the geometric variability observed in the fusion zones and heat affected zones of several combinations of AHSS (different types, coatings and thicknesses), which were butt welded using a Trumpf TRUDISK 6000® Yb:YAG laser beam, is presented. The surface texture parameters such as roughness and waviness of laser welds were also measured and correlated with geometric variability. Results indicate that although high quality welds with minimal defects can be obtained using the Yb:YAG laser welding process, there is considerable variation in both the shape and the dimensions of weld zones. The variability increased with an increase in thickness differentials between the sheets being welded. Analysis of top of the weld surfaces also suggested that aluminum coating on USIBOR samples contributes significantly to increased roughness. An increase in laser power coupled with corresponding increase in welding speed did not impact variability. A fair correlation between the surface roughness and weld region variability exists, although this needs further study.

4.1 Introduction

Demand for higher automotive fuel efficiency without an undue sacrifice of passenger safety has been on the rise in the worldwide automotive market. Consequently the vehicles need to be lighter while at the same time the vehicle structures should have the ability to manage the crash energy better; this led to the utilization of advanced high strength steels (AHSS). Considerable information on AHSS materials and their properties can be found in literature (for example, see References 1, 2). The most popular among the AHSS materials are Transformation Induced Plasticity (TRIP) steels, Dual Phase (DP) steels, Martensitic steels and the more recently developed Twinning Induced Plasticity (TWIP) steels. USIBOR steels, also called Boron steels or MnB steels, are also emerging as serious contenders but cannot be cold-formed. Hot stamping is used for such materials by first austenitizing the material to about 900˚C, stamping in the hot condition and subsequently quenching in the die to produce large fraction of martensite. With this process, USIBOR materials can attain tensile strengths of up to 1500 MPa.

One of the most efficient ways of designing with AHSS is Tailor Welded Blanks (TWB), which uses blanks of different materials, thicknesses, coatings, or surface treatments which are joined together before metal forming operations are carried out. This could result in substantial weight reduction while adding ultra high strength or high energy absorption characteristics resulting in increased fuel efficiency and safety. Butt welded joints are more suitable than lap-welded joints for TWB applications since they can be used more effectively for metal forming operations.

Lasers offer significant advantages when joining automobile panels such as high weld strength, excellent finish, simplicity, flexibility and reliability in manufacturing compared to other processes such as resistance spot welding, gas metal arc welding and electron beam welding [3]. The main limitation is the cost per watt, however, this is rapidly declining with novel advances in laser technology. Autogenous welding is the most common form of laser welding although a suitable filler material can be added in some cases, such as when a gap needs to be filled.

A knowledge of the microstructure and mechanical performance of the fusion zone as well as the heat affected zone (HAZ) obtained with laser welding is essential to ensure the reliability of the process; these aspects are well addressed [4-9]. However, a clear understanding of the size variability of the fusion zone and HAZ, as well as the surface finish that can be achieved during the laser welding, can contribute to the improved reliability and usage of the laser welds. Geometric variability and surface finish become more significant for TWB's involving hot-forming materials such as USIBOR that are welded to other ultra-high strength materials such as DP980; this is because the subsequent austenitizing and quenching process considerably lowers the hardness of the fusion zone and therefore the tensile strength of the joints. In such cases, severe concavity, for instance, would significantly lower the joint strength. Limited work has been reported on the effect of various parameters on the kerf width and heat affected zone variability and the majority of said work has been for traditional 4130 steels [10]. Research data has also been documented on the surface roughness produced by CO2 laser welding of zinc coated low carbon steels [11]. But the information on the dimensional variability and surface roughness of fusion zones in laser welded AHSS steels is not available.

In this paper, the geometry and surface finish of the fusion zone obtained during laser welding were studied when welding a variety of AHSS steels. A high beam quality Yb:YAG laser was utilized to prepare the joints.

4.2 Experimental Procedure

The following types of materials were used for the welding experiments:

- TRIP780 (galvanized using galvanized iron or GI process and cold rolled, 1.0 mm thick),
- DP980 (without protective coating and cold rolled, 1.5 mm thick),
- USIBOR (aluminum coated and cold rolled, 1.8 mm thick), and
- Mild steel (without protective coating cold rolled, 1.0 mm thick).

The chemical compositions of the materials are presented in Table 4.1. Strips of 75 mm width were cut from parent materials of TRIP780 (designated TR), DP980 (DP), USIBOR (U) and mild steel (MS). Prior to welding of the samples, the edges were milled and cleaned with acetone to remove any debris. A butt joint configuration was used in all cases. The samples were loaded on the flat surface of the weld fixture and clamped down while ensuring that the milled edges were firmly in contact against each other. Two 25 mm thick top plates and bolts (two on each side) were used to clamp down the samples that assured the absence of movement during the welding operation [Figure 4.1(a)]. The locating scheme, as shown in Figure 4.1(b), also minimized re-adjustment of the starting point of the laser beam and its direction of movement. Argon shielding gas was used at a flow rate of 30 liters/min (1.8 cubic meters/hour) during the welding process. The shielding gas flow was set perpendicular to the welding direction, with the nozzle moving synchronously with the laser beam to keep the shielding uniform over the weld pool.

Table 4.1 Chemical compositions (wt%) of materials used

Steel	C	Mn	Mo	P	S	Si	Cr	Al	B	Ti	V	Nb	Ni	Cu	N
USIBOR 1500P	0.220	1.100	0.003	0.012	0.003	0.264	0.172	0.051	0.0023	0.040	0.005	0.001	0.009	0.028	0.004
DP980	0.135	2.100	0.350	--	--	0.050	0.150	0.450	0.007	--	--	--	--	--	--
TRIP780	0.190	1.580	--	0.013	0.025	1.600	0.070	0.036	--	0.027	--	0.038	0.020	0.020	
Mild Steel	0.043	0.270	0.002	0.041	0.009	0.021	0.020	0.040	0.000	0.002	0.001	--	--	--	0.007

Welding was carried at two power levels, 2.0 kW and 3.7 kW, at constant speeds of 70 mm/sec and 150 mm/sec, respectively. These parameters ensured that full weld penetration was achieved. These two speeds and power levels were determined by a series of trials using bead-on-plate approach. A Trumpf high power TRUDISK® 6002 laser beam, delivered from a 6 kW Yb:YAG solid state laser (wavelength: 1030 nm, focal length: 200 mm, focal spot diameter: 0.6 mm) to a robotic arm via fiber optics, was used to weld the samples using the fixture as shown in Figure 4.1(b). The samples were held stationary in the fixture, while the laser beam attached to the robot's end effector moved along the edges of the samples being joined. For the combinations involving USIBOR steels, the laser beam was set at a 6 degree angular deviation from normal to join the materials. A higher power level of 4.5 kW was used for USIBOR combinations since USIBOR had a thickness of 1.8 mm. For all other combinations, the laser beam was set perpendicular to the surfaces of materials being joined. Five combinations of welds carried out are studied in this paper:

- TRIP780 welded to mild steel at 70 mm/sec speed (designated TR/MS-70),
- TRIP780 welded to mild steel at a higher speed of 150 mm/sec (TR/MS-150),
- TRIP780 welded to DP980 (TR/DP),
- USIBOR welded to TRIP780 (U/TR), and
- USIBOR welded to DP980 (U/DP).

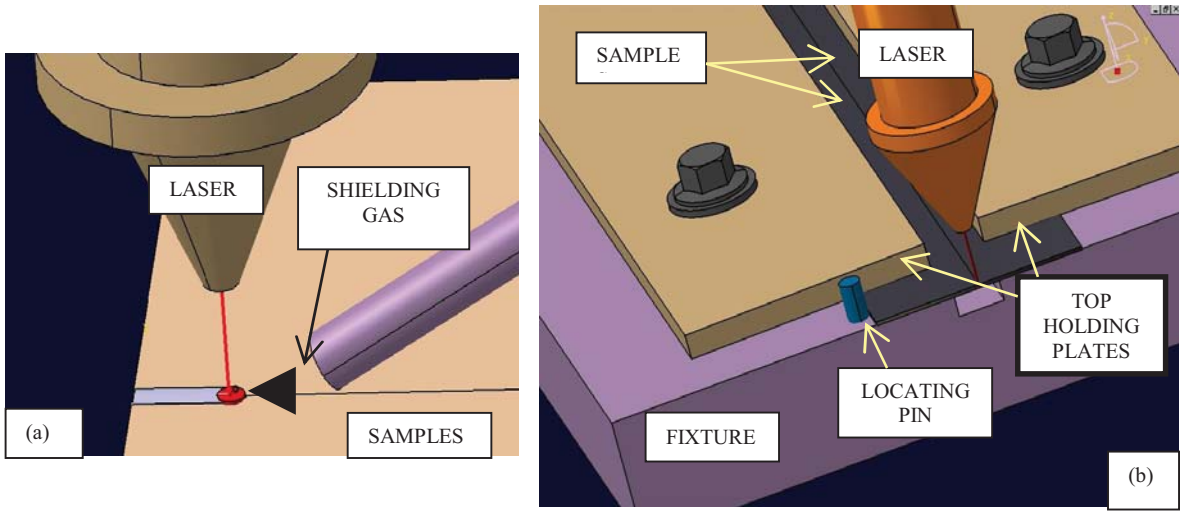

Figure 4.1(a) Laser welding set-up showing (a) laser beam welding the samples, with the shield gas flowing in a direction opposite to the welding direction, and (b) weld fixture.

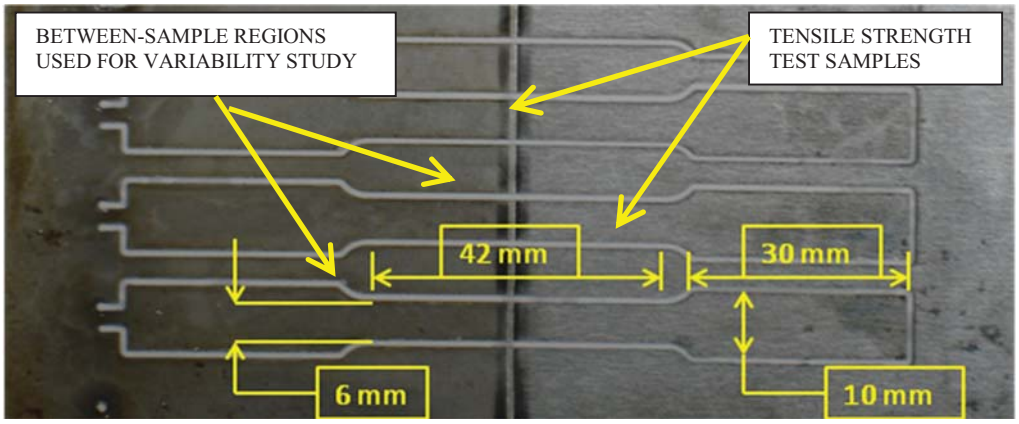

Figure 4.2 Coupon of TRIP780 welded to mild steel (TRIP/MS) and tensile samples cut using high pressure hydro jet. Major nominal dimensions are shown.

More information on the laser power and weld speed used is provided in Table 4.2. After the welding was completed, tensile test samples 10 mm wide at the grip and 6 mm in the mid region, as shown in Figure 4.2, were prepared using high pressure hydro-jet cutting operation. Results of tensile tests using these samples have been reported earlier on combinations of TRIP780 welded to mild steel (TR/MS) and TRIP780 welded to DP980 (TR/DP) [9]. Measurements of the cut samples showed that the width of all samples was within 6.0 ± 0.25 mm. Statistical analysis revealed that the standard deviation of the sample widths at the weld point was 0.08 mm, with an average width of 6.04 mm.

Table 4.2 Experimental set-up for laser welds

Sample ID	Material 1	Thickness (mm)	Material 2	Thickness (mm)	Laser Power (KW)	Weld Speed (mm/sec)	Laser beam incident angle
TR/MS-70	TRIP780 cold rolled & galvanized (GI process)	1.0	Mild Steel cold rolled, no protection	1.0	2.0	70	Normal to sample surface
TR/MS-150	TRIP780 cold rolled & galvanized (GI process)	1.0	Mild Steel cold rolled, no protection	1.0	3.7	150	Normal to sample surface
TR/DP	TRIP780 cold rolled & galvanized (GI process)	1.0	DP980 cold rolled, no protection	1.5	2.0	70	Normal to sample surface
U/TR	USIBOR (Boron Steel) aluminum coating	1.8	TRIP780 cold rolled & galvanized (GI process)	1.0	4.5	150	6˚ off normal to sample surface
U/DP	USIBOR (Boron Steel) aluminum coating	1.8	DP980 cold rolled, no protection	1.5	4.5	150	6˚ off normal to sample surface

The welded regions left between the tensile samples were saved for metallurgical analysis and for surface roughness measurements. These pieces were sectioned using a cutoff wheel, mounted in resin, polished and etched with 3% Nital solution. Six samples of each of four weld types, TR/MS-70, TR/MS-150, TR/DP and U/TR, were used to study the variability of several characteristics. Optical micrographs at 50X were obtained for each sample and measurements for various characteristics were recorded to understand the variability for each characteristic. Surface roughness measurements were made on the same four weld types using the laser scan surface roughness analyzing system manufactured by UBM Corporation. For each case, six scans in 0.5 mm width of the weld region for a length of 40 mm were obtained. It was noted that U/TR weld, which had aluminum from the USIBOR sample and zinc from TRIP780 exhibited significantly higher values of surface

roughness and waviness. To understand whether aluminum was the major contributor to higher surface roughness or if both aluminum and zinc contributed to it, the U/DP weld was also analyzed for surface roughness. These two sample combinations (U/TR and U/DP) were also further examined under scanning electron microscope (SEM) to identify the factors that might have caused higher roughness in U/TR combination.

4.3 Results and discussion

Visual and optical examination of the welds revealed full penetration joints with 0 to 3 mm distortion in a direction perpendicular to the surface of the samples. It is surmised that there could be some residual stresses around the weld region [12].

4.3.1 Dimensions of weld zones

Examination of the fusion zones of TR/MS-70 combination samples shows that the weld region is fairly consistent in both size and shape. Figure 4.3 shows the optical micrographs of the sections on four of these samples. The weld region shows a typical hour-glass configuration for all cases. Some sections show a minor concavity in the top of the weld and a dip in the bottom which is characteristic of full penetration weld due to gravity effects.

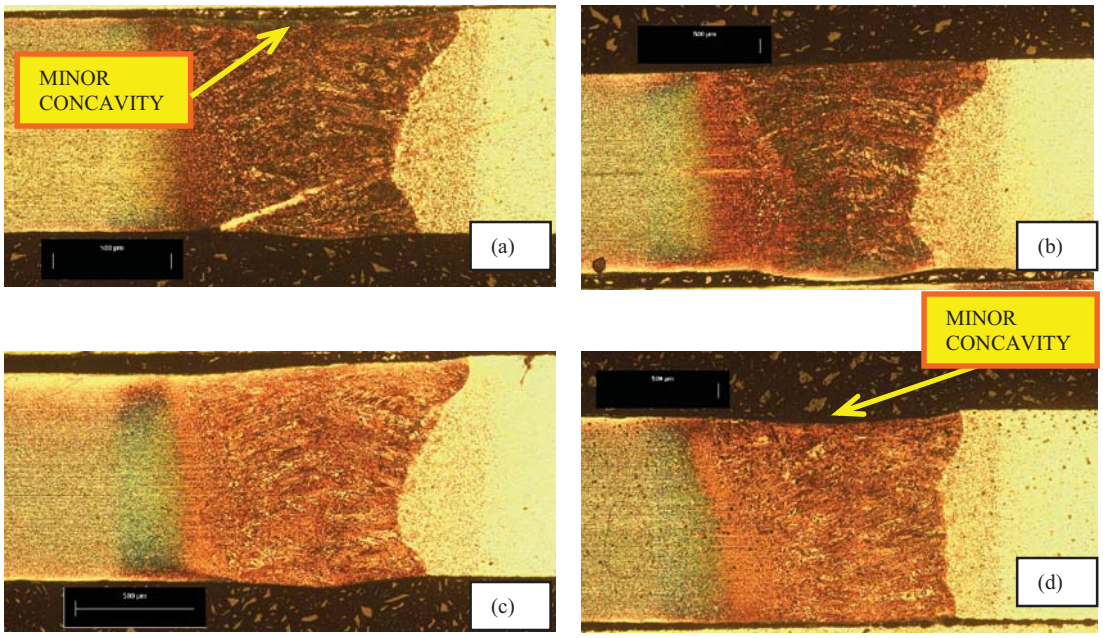

Figure 4.3 Optical micrographs (50X) showing variations in the fusion zones of TR/MS-70 combination welded at lower speed of 70 mm/sec and 2.0 kW power.

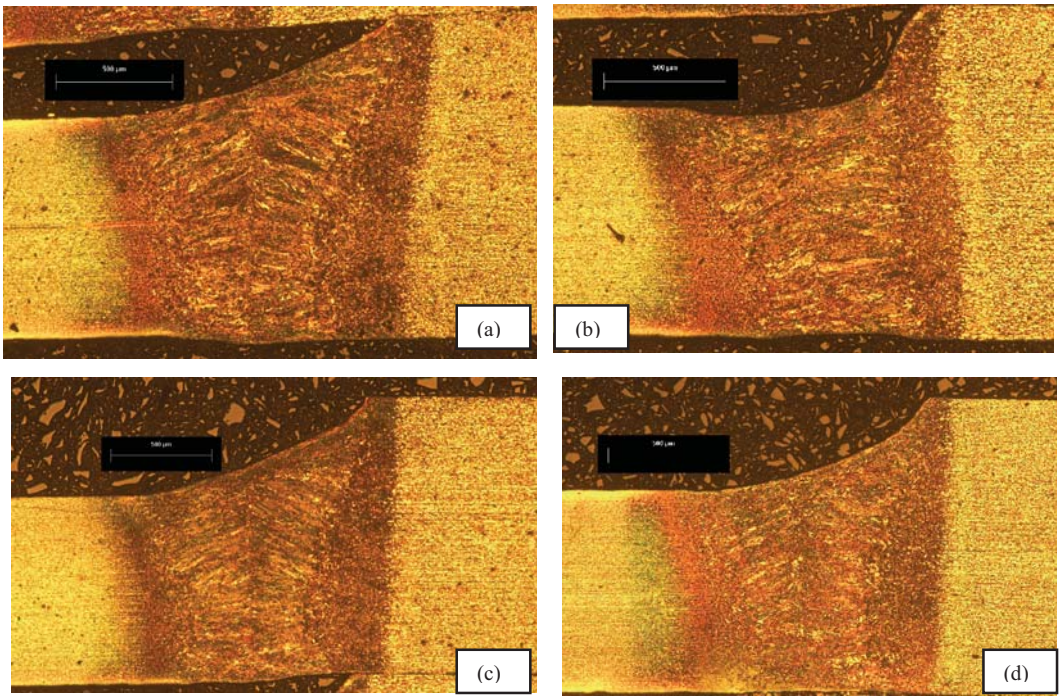

Figure 4.4 Optical micrographs (50X) showing variations in the fusion zones of TR/DP combination.

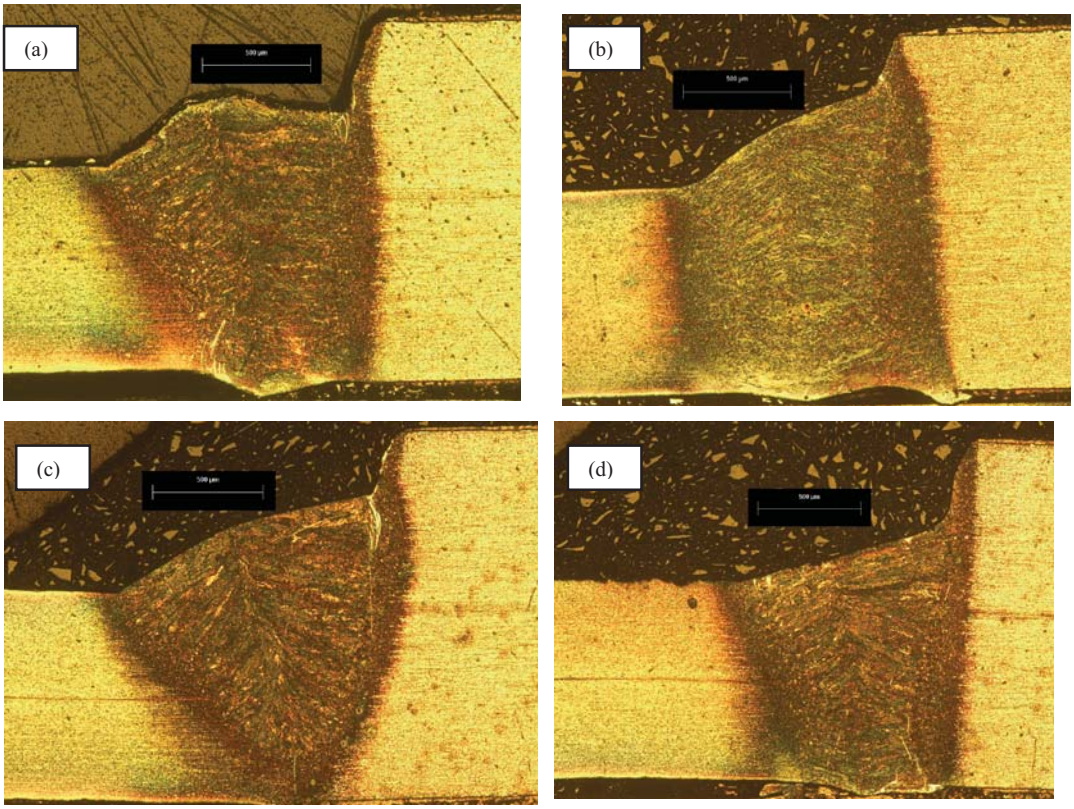

Figure 4.5 Optical micrographs (50X) showing variations in the fusion zones of U/TR combination.

The samples from the higher speed, higher power TR/MS-150 combination also showed similar consistency while exhibiting the hour-glass shape. The tear-drop in the bottom seemed to be more pronounced and is attributed to the higher heat input and speed. The weld pool becomes more elongated and a shift from elliptical to teardrop occurs. There is a tendency for more concavity in the top, especially on the MS side of the weld.

Four samples each for TR/DP and U/TR combinations are shown in Figures 4.4 – 4.5. The micrographs in Figures 4.4 and 4.5 indicate considerably more variation in TR/DP and U/TR than the TR/MS-70 welds. The weld concavity in the top is more pronounced in some cases and substantial differences in the size and shape of the weld zone can be noted. The larger variation in TR/DP and U/TR combinations can be partially attributed to variations in the path of the laser beam in the transverse direction. When the beam strays more towards the thinner material, lesser material from the thicker material would be melted and this would result in a deeper cavity on the top surface; when the beam strays towards the thicker material, more of the thicker material would be melted smoothing out the cavity and resulting in a smoother transition. This would also cause variations in the concavity observed in the sample combinations with larger thickness differentials. U/TR combination shows the highest variability in the shape and size of the fusion zone and indicates that for this combination, profiles of welds made under identical conditions are different. In two of the samples, the top shows an upstanding teardrop shape.

4.3.2 Measurement of dimensional characteristics in the fusion and heat affected zones

In order to quantify the dimensional variation in the weld zone, measurements of the fusion zone as well as HAZ were taken. Seven dimensions as shown in Figure 4.6 (a) - (c) were measured. Characteristics A, B and C measure the weld dimensions in the top, bottom and the waist regions, while D and E measure weld concavity in the top and the teardrop in the bottom. The HAZ characteristics are addressed by measurement of F, measured at the top and G, measured at the bottom. Characteristics for TR/MS-70 and TR/MS-150 samples were measured as shown in Fig. 6 (a). Slight changes to the measurement scheme as shown in Figure 4.6 (b) and (c) were made to accommodate larger thickness differentials in TR/DP and U/TR combinations.

Statistical analysis was performed on the dimensions measured for all samples of the four combinations. The results are shown in Table 4.3. In order to understand which combinations had significantly different averages and variations, two statistical tests – the two-tailed t-test and the F-test – were carried out [13]. It was assumed that all the data are normally distributed. The results are shown in Tables 4.4 and 4.5. Results with statistical significance are marked with “YES” and are circled in red. For the t-test, a significance level (α) of 0.005 was chosen, while for the F-test, a value of α=0.1 was used.

Table 4.3 Dimensions of characteristics of weld zones (μM)

Material combination	Statistics	A	B	C	D	E	F	G
TR/MS-70	Average	1137.5	822.8	722.0	32.2	34.3	1400.2	1212.2
	Standard Deviation	57.9	55.7	69.4	42.0	23.0	47.9	69.3
TR/DP	Average	1137.7	752.5	661.0	135.8	18.3	1360.7	1113.2
	Standard Deviation	94.0	23.2	25.0	57.3	17.3	58.5	27.7
TR/MS-150	Average	1058.7	873.8	776.0	18.0	59.0	1360.8	1227.5
	Standard Deviation	26.8	100.0	43.1	37.0	15.9	78.4	103.6
U/TR	Average	1065.2	792.6	693.4	16.8	188.2	40.7	1287.2
	Standard Deviation	112.2	82.9	96.1	35.3	66.5	28.3	117.6

Table 4.4 Student t-tests for comparison of means

$t_{DOF=10,\ \alpha=0.005}$	3.169

H_0: $\mu_1-\mu_2 = 0$ or $\mu1 = \mu2$

H_A: $\mu_1-\mu_2 \neq 0$ or $\mu1 \neq \mu2$

N_1	6
N_2	6
DOF	10

		A	B	C	D	E	F	G
TR/MS-70 Vs TR/MS-150	Standard Error (SE)	26.06	46.72	33.36	22.86	11.43	37.52	50.91
	$t_{statistic}$	3.03	-1.09	-1.62	0.62	-2.16	1.05	-0.30
	Absolute value($t_{statistic}$)	3.03	1.09	1.62	0.62	2.16	1.05	0.30
	Reject H0 at α=0.005?	NO	NO	NO	NO	NO	NO	NO
TR/MS-70 Vs TR/DP	Standard Error (SE)	45.09	24.64	30.12	29.02	11.76	30.89	30.48
	$t_{statistic}$	0.00	2.85	2.03	-3.57	1.36	1.28	3.25
	Absolute value($t_{statistic}$)	0.00	2.85	2.03	3.57	1.36	1.28	3.25
	Reject H0 at α=0.005?	NO	NO	NO	YES	NO	NO	YES
TR/MS-70 Vs U/TR	Standard Error (SE)	205.75	181.16	129.89	36.33	12.19	249.14	193.96
	$t_{statistic}$	1.36	1.30	2.14	-3.90	0.58	1.49	2.53
	Absolute value($t_{statistic}$)	1.36	1.30	2.14	3.90	0.58	1.49	2.53
	Reject H0 at α=0.005?	NO	NO	NO	YES	NO	NO	NO

The t-tests on TR/MS-70 versus TR/MS-150 samples indicate that higher laser power and weld speed used in TR/MS-150 samples have no effect on the characteristics measured. On the other hand, the t-tests on TR/MS-80 versus TR/DP as well as TR/MS-70 versus U/TR suggest that the weld concavity in the top (characteristic "D") is significantly larger when different thicknesses are joined. The effect seems to be larger in U/TR samples since there were two cases of ‘upstanding’ tear-drop shapes in the top with values of 88 and 13 μm. Because of the small sample size, statistical tests were not conducted to prove this point, however. Thicker DP980 material used in TR/DP combination has resulted in a large width of the HAZ (characteristic "G") at the

bottom. Barring this one exception, the widths of HAZ are not significantly different in TR/MS-150, TR/DP and U/TR combinations compared to TR/MS-70 samples.

Table 4.5 F-tests for comparison of variances

$F_{(5,5),\ \alpha=0.1}$	3.453	N_1	6	
H_0: $\sigma_1^2-\sigma_2^2 = 0$ or $\sigma_1^2 = \sigma_2^2$		N_2	6	
H_A: $\sigma_1^2 \neq \sigma_2^2$				

		Characteristics						
		A	B	C	D	E	F	G
F-test for TR/MS-70 versus TR/MS-150								
TR/MS-70	Standard Deviation	57.9	55.7	69.4	42.0	23.0	47.9	69.3
	Variance	3356.3	3104.6	4820.0	1763.0	529.5	2295.8	4809.4
TR/MS-150	Standard Deviation	26.8	100.0	43.1	37.0	15.9	78.4	103.6
	Variance	718.3	9994.2	1856.4	1371.2	254.0	6149.0	10742.7
	σ_1^2/σ_2^2	4.67	0.31	2.60	1.29	2.08	0.37	0.45
TR/MS-70 Vs TR/MS-150	$F_{statistic}$ (σ_1^2/σ_2^2, with $\sigma_1>\sigma_2$)	4.67	3.22	2.60	1.29	2.08	2.68	2.23
	Reject H0 at α=0.1?	YES	NO	NO	NO	NO	NO	NO
F-test for TR/MS-70 versus TR/DP								
TR/MS-70	STD DEVIATION	57.9	55.7	69.4	42.0	23.0	47.9	69.3
	VARIANCE	3356.3	3104.6	4820.0	1763.0	529.5	2295.8	4809.4
TR/DP	STD DEVIATION	94.0	23.2	25.0	57.3	17.3	58.5	27.7
	VARIANCE	8840.3	539.5	623.6	3289.0	300.3	3427.9	765.0
	σ_1^2/σ_2^2	0.38	5.75	7.73	0.54	1.76	0.67	6.29
TR/MS-70 Vs TR/DP	$F_{statistic}$ (σ_1^2/σ_2^2, with $\sigma_1>\sigma_2$)	2.63	5.75	7.73	1.87	1.76	1.49	6.29
	Reject H0 at α=0.1?	NO	YES	YES	NO	NO	NO	YES
F-test for TR/MS-70 versus U/TR								
TR/MS-70	STD DEVIATION	57.9	55.7	69.4	42.0	23.0	47.9	69.3
	VARIANCE	3356.3	3104.6	4820.0	1763.0	529.5	2295.8	4809.4
U/TR	STD DEVIATION	500.7	440.2	310.5	78.5	19.0	608.4	470.0
	VARIANCE	250653.3	193803.5	96406.5	6155.5	362.0	370115.0	220916.7
	σ_1^2/σ_2^2	0.01	0.02	0.05	0.29	1.46	0.01	0.02
TR/MS-70 Vs U/TR	$F_{statistic}$ (σ_1^2/σ_2^2, with $\sigma_1>\sigma_2$)	74.68	62.43	20.00	3.49	1.46	161.22	45.93
	Reject H0 at α=0.1?	YES	YES	YES	YES	NO	YES	YES

Results of the F-test comparing TR/MS-70 to TR/MS-150 indicate that, except for the width of the fusion zone (characteristic "A"), higher speed does not have any effect on variances. TR/DP sample combination has significantly different variability compared to TR/MS-70 for width of the fusion zone in the bottom ("B") and width of the fusion zone in the center ("C"). On the other hand, U/TR combination has significantly higher

variability compared to TR/MS-70 samples. Except for the variability in the bottom of the weld (characteristic "E") the null hypothesis that the variance for TR/MS-70 and U/TR are the same can be rejected for all characteristics. This includes a rejection of null hypothesis for characteristic "D" (concavity) at a confidence level of $\alpha = 0.1$. This indicates that increased thickness differentials between the samples being welded would result in higher variability for the characteristics such as concavity in the top of the weld.

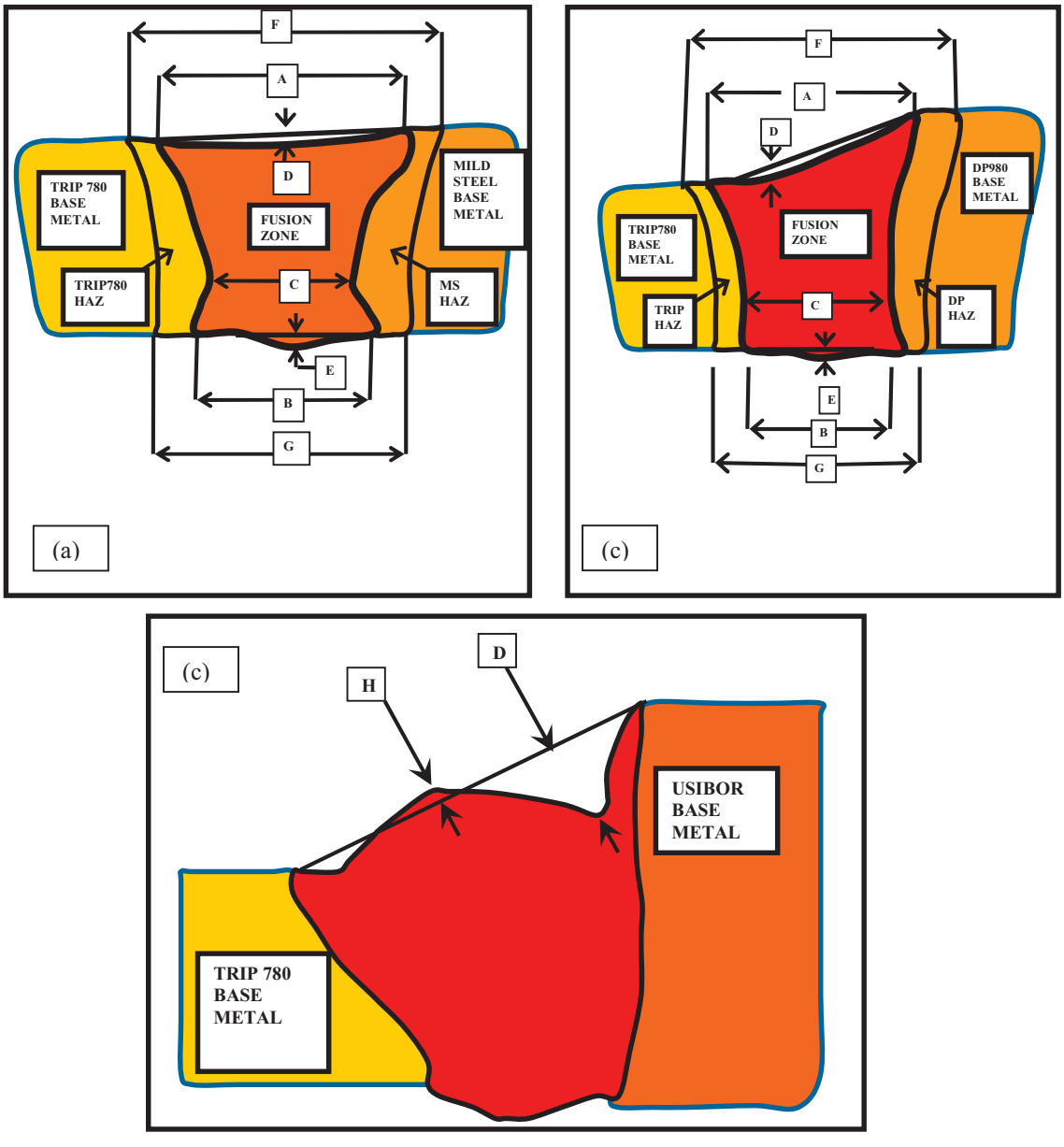

Figure 4.6 Characteristics measured in the weld zones of (a) TR/MS samples and (b) U/TR samples. Additional characteristic, H, measured on U/TR samples, is shown in (c) along characteristic D with the direction of measurement as shown.

4.3.3 Surface roughness

The high variability observed for the concavity (and 'reverse tear-drop') noted on the top of the weld for U/TR combinations could be associated with higher surface roughness compared to TR/MS-70 combination. To confirm this, the surface roughness values were obtained for the four combinations. Since U/TR samples had aluminum and zinc coatings on the USIBOR and TRIP materials, respectively, it was decided to obtain surface roughness on U/DP samples as well. Since DP samples are uncoated, by comparing U/TR to U/DP, one could arrive at a conclusion on whether the aluminum coating on USIBOR samples alone made a significant impact on surface roughness or whether aluminum and zinc coatings together would influence the results.

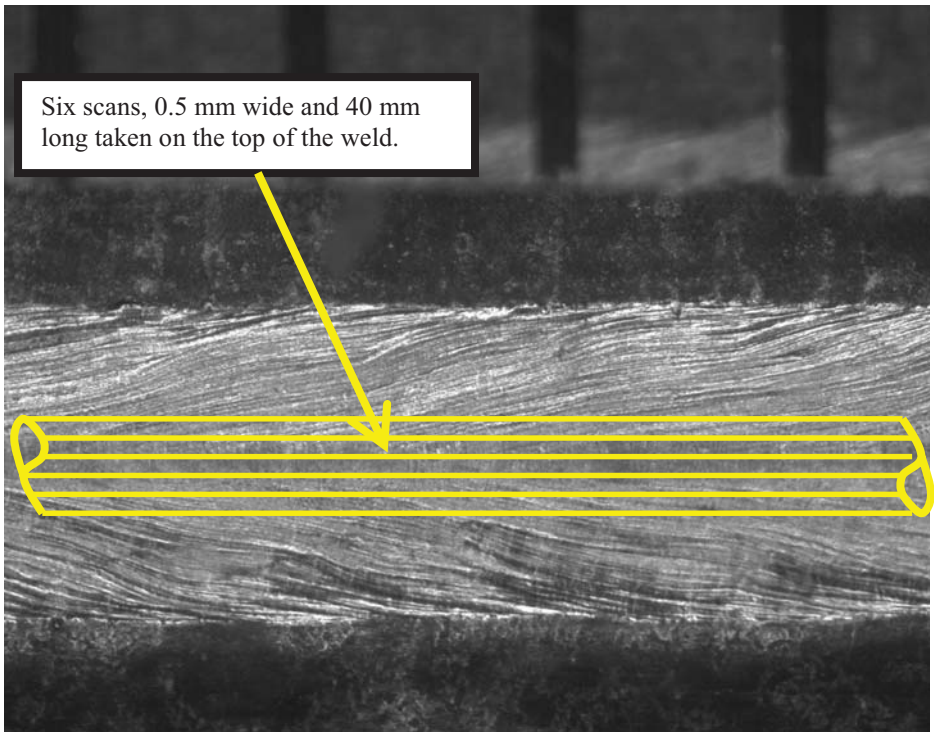

Figure 4.7 Area scanned on the top of the weld. The micrograph shows top of TR/MS-70 weld (scale indicated in mm in the top).

For each combination, six scans were obtained parallel to the weld direction in an area that was 0.5mm wide; each scan was 40 mm long, as shown in Figure 4.7. The roughness R_a and waviness W_t values for all scans obtained for the five combinations are shown in Table 4.6. Both R_a and W_t for U/TR combination are significantly higher than those for all other combinations including TR/MS-70 sample. This is in agreement with the F-test results rejecting the null hypothesis for the TR/MS-70 versus U/TR samples obtained for characteristic "D" and presented in Table 4.5. It can also be seen that the R_a value for the U/DP combination is

slightly higher than that obtained for the TR/MS-70 combination but not as high as the value obtained for the U/TR combination. The waviness value for U/DP is lower than that of the TR/MS-70 samples, but the U/TR samples exhibited the highest waviness values. Scanning electron microscope studies to understand this difference between U/TR and U/DP combinations are presented later in this paper.

Table 4.6 Roughness and waviness parameters (DIN 4776 standards)

Material combination	Description	Roughness R_a (Microns)	Waviness W_t (Microns)
TR/MS-70	All scans	9.05	73.28
TR/MS-150	All scans	3.41	23.73
TR/DP	All scans	2.77	45.29
U/TR	All scans	22.51	97.11
U/DP	All scans	9.43	54.56

The roughness profiles obtained for TR/MS-70, TR/DP and U/TR samples are displayed in Figure 4.8. There is a slight taper exhibited in all figures shown in Figures 8 (a) - (c) for TR/MS-70, TR/DP and U/TR samples indicating that the samples distorted during the welding process. The taper seems to be about 0.12 mm over a 40 mm length in the TR/MS-70 sample and about 0.1 mm over 40 mm length in the TR/DP sample. The taper seems to be higher in the U/TR sample and estimated to be about 0.2 mm. The tapers noticed were due to geometric variability due to various factors, since scanning the weld surface in other areas of the samples yielded different values for the tapers. The profiles as seen in Figure 4.7 and Table 4.6 suggest that the U/TR samples have higher roughness compared to TR/MS-70 and TR/DP samples. Typical single line scans for TR/MS-70 and U/TR samples, both filtered per DIN 4776 standards, are presented in Figure 4.9. The roughness characteristics for TR/MS-70 are more evident due to lesser waviness when compared to U/TR samples. It can be seen that the U/TR sample line trace shows a range of 300 μm. Since the 6σ value for characteristic D for U/TR is 210 μm (σ = 35 μm), using the 6σ value as the basis, the error is of the order of -43%, which can be considered reasonable considering that only 6 samples are used for the 6σ calculation.

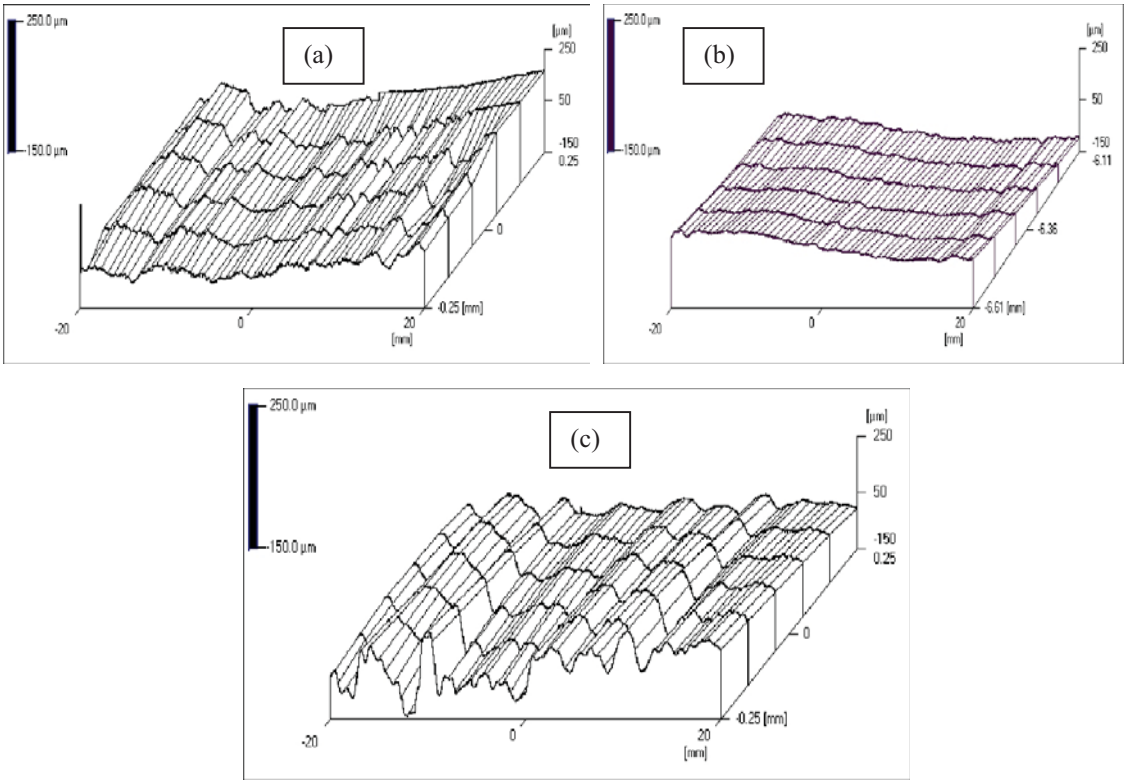

Figure 4.8 Roughness profiles (a) TR/MS-70 sample, (b) TR/DP sample and (c) U/TR samples, top of the weld. 6 scans in 0.5 mm width of the weld, each 40 mm long, were obtained.

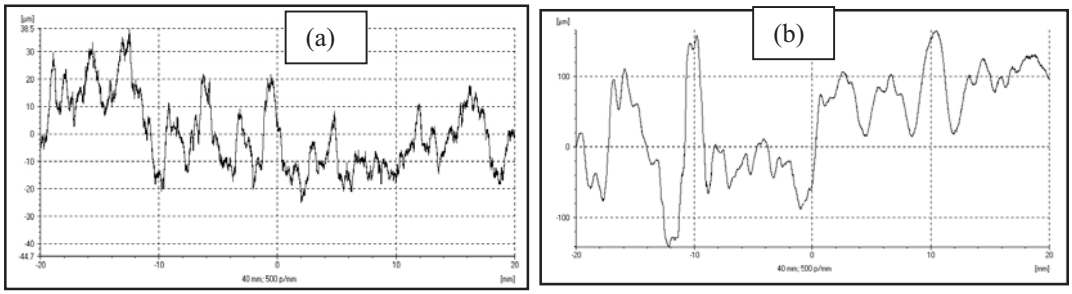

Figure 4.9 Single line scans of (a) TR/MS-70 sample, and (b) U/TR sample. The roughness characteristics of TR/MS-70 sample are more evident since it has less waviness. On the other hand, the larger waviness of U/TR samples seems to have hidden the roughness characteristics.

The concavity value "D" measured from the actual sections for the other samples studied did not compare as well with the line scan range data. For example, the TR/MS-70 sample had a line scan range of 70 µm and a 6σ value of 252 µm, resulting in a 72% error, while TR/DP sample had line scan data of 120 µm and 6σ value of 344 µm, with an error of 65%. This disparity can be explained by noting that the line scans are in a longitudinal direction while the 6σ values are arrived at by sectioning the weld regions in a transverse direction

(the UBM scanning system available could not handle the depths of field required for transverse scans). Also, since different samples are used for 6σ evaluation versus line scan data, more data will lead to better results.

Analysis of the R_a values plotted against W_t values for all scans showed good correlation, with a coefficient of 0.901. It has been reported in literature that due to their inherent stochastic nature, processes such as shot blasting and electrical discharge texturing show a good correlation between roughness and waviness parameters (there is generally an increase in the waviness with increase in surface roughness) [14]. Apparently the stochastic nature of the laser welding process also introduces a correlation between waviness and roughness factors. An attempt to correlate standard deviation values obtained from the actual sections (Table 4.3) to the roughness characteristics (R_a) for all scans for TR/MS-70, TR/DP, TR/MS-150 and U/TR sample combinations indicate a somewhat weaker correlation coefficient of -0.582. The waviness characteristics (W_t) showed even weaker correlation with a correlation coefficient of -0.306. Again, it is surmised that a better correlation can be obtained between the standard deviation values and roughness and waviness characteristics with the collection of more data. It is likely that a few large surface anomalies are providing a significant impact to the data set.

4.3.4 Analysis of U/TR and U/DP surfaces using SEM

Scanning electron microscopy (SEM) was utilized to study the surface roughness of U/TR samples and U/DP samples. It was theorized that aluminum coating on USIBOR samples contributed significantly to higher roughness and waviness values in U/TR samples. To determine if zinc had any effect on surface roughness a comparison of U/TR to U/DP was made since TR has zinc coating and DP has no coating (cold rolled). Since both contain aluminum and only one contains zinc, this would provide an understanding of the effect of zinc on surface roughness.

Figure 4.11 shows SEM micrographs of the top of the surfaces for the two combinations. It can be seen that the U/TR surface shown in Figure 4.11(a) consists of many rough ridges with bright surfaces near the USIBOR base metal. This surface seems to be considerably rougher compared to that obtained for the U/DP combination shown in Figure 4.11 (b). This is further supported by an examination of micrographs shown in Figure 4.12 shown at higher magnification. The ridges on U/DP in Figure 4.12 (a) near DP980 base metal seemed to be wider apart compared to those on U/TR shown in Figure 4.12 (b).

Further analysis of the U/TR weld showed many spatters of metal near the TRIP surface as shown in the micrograph of Figure 4.13 (a). One of these spatters, shown in Figure 4.13 (b), was subjected to spectral analysis and proved to contain both aluminum and zinc elements, indicating that the droplets could have been formed from the top layers of both USIBOR and TRIP780 steel. It can also be seen from Figure 4.13 (a) that

the surface is very grainy, which resulted in higher roughness. This suggests that the zinc layer also contributes to an increase in the surface roughness.

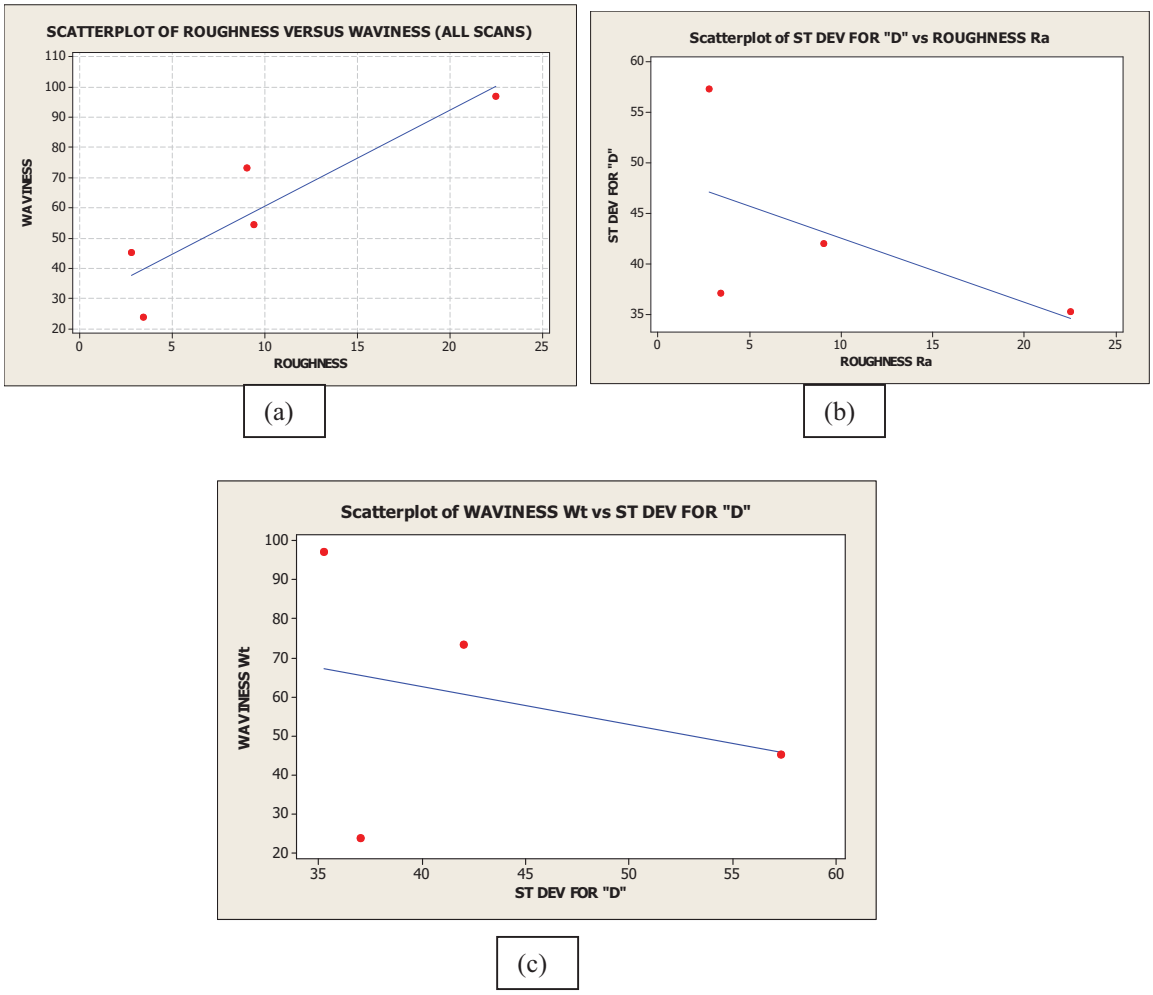

Figure 4.10 (a) Graph of roughness versus waviness parameters obtained for all values (correlation coefficient = 0.901) (b) Plot of roughness values obtained for all scans from Table 4.6 versus standard deviation values for characteristic "D" (correlation coefficient = -0.582) (c) Plot of waviness values obtained for all scans from Table 4.6 versus standard deviation values for characteristic "D" (correlation coefficient = -0.306)

The bright surfaces near the USIBOR region as shown in Figure 4.11 (b) are further analyzed in Figure 4.14. The bright layers forming rough ridges are quite uneven. Spectral analysis indicates that these bright layers are richer in zinc compared to aluminum, leading to the conclusion that zinc alloys in the coating of TRIP780 would have boiled, blown by the shielding gas and re-deposited on the weld surface.

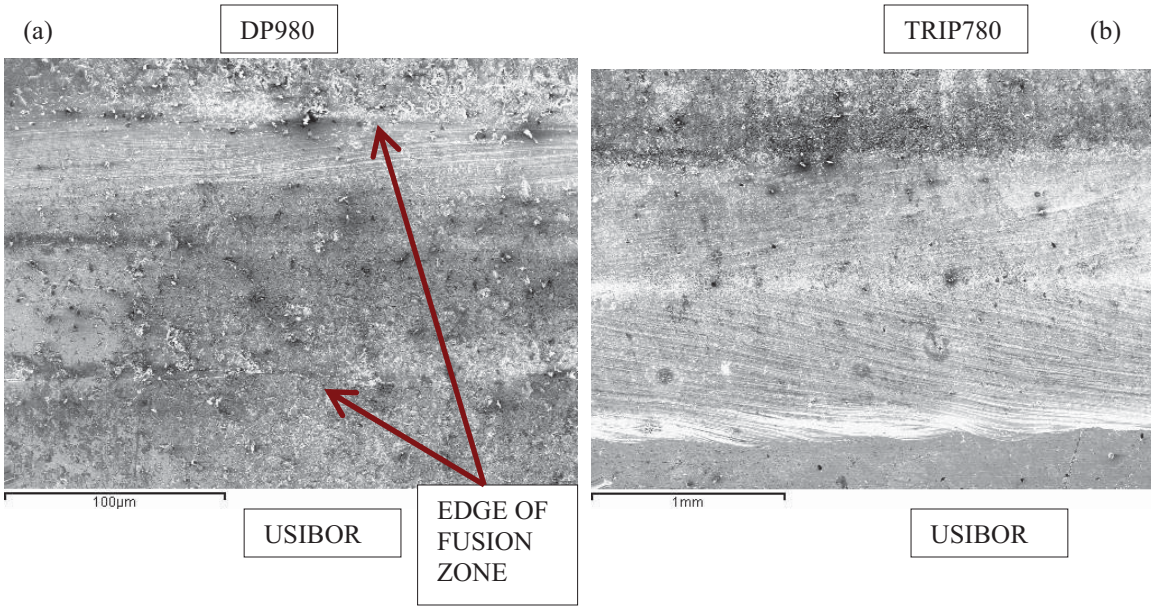

Figure 4.11 SEM micrographs of top of the welded surfaces for (a) U-DP combination and (b) U-TR combination, both shown at 45X.

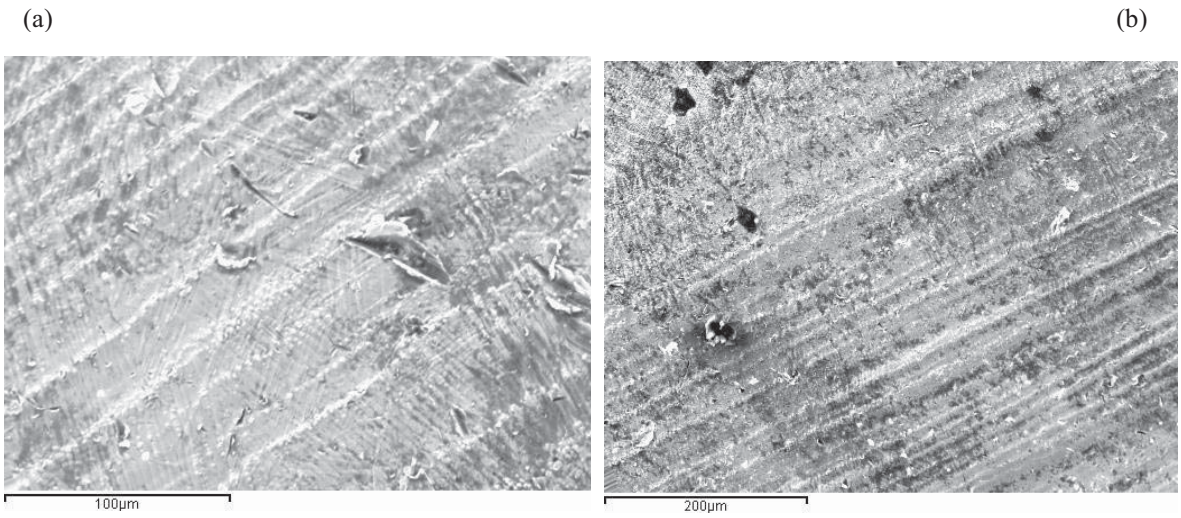

Figure 4.12 SEM micrographs of (a) U-DP combination near the DP region, shown at 100X and (b) U-TR combination near the TRIP region, shown at 230X. The samples were slightly tilted to get a better view. Spatters of metal, generally containing aluminum and zinc, seemed to be present on both surfaces but more frequently on U-TR surface.

USIBOR-TRIP WELD

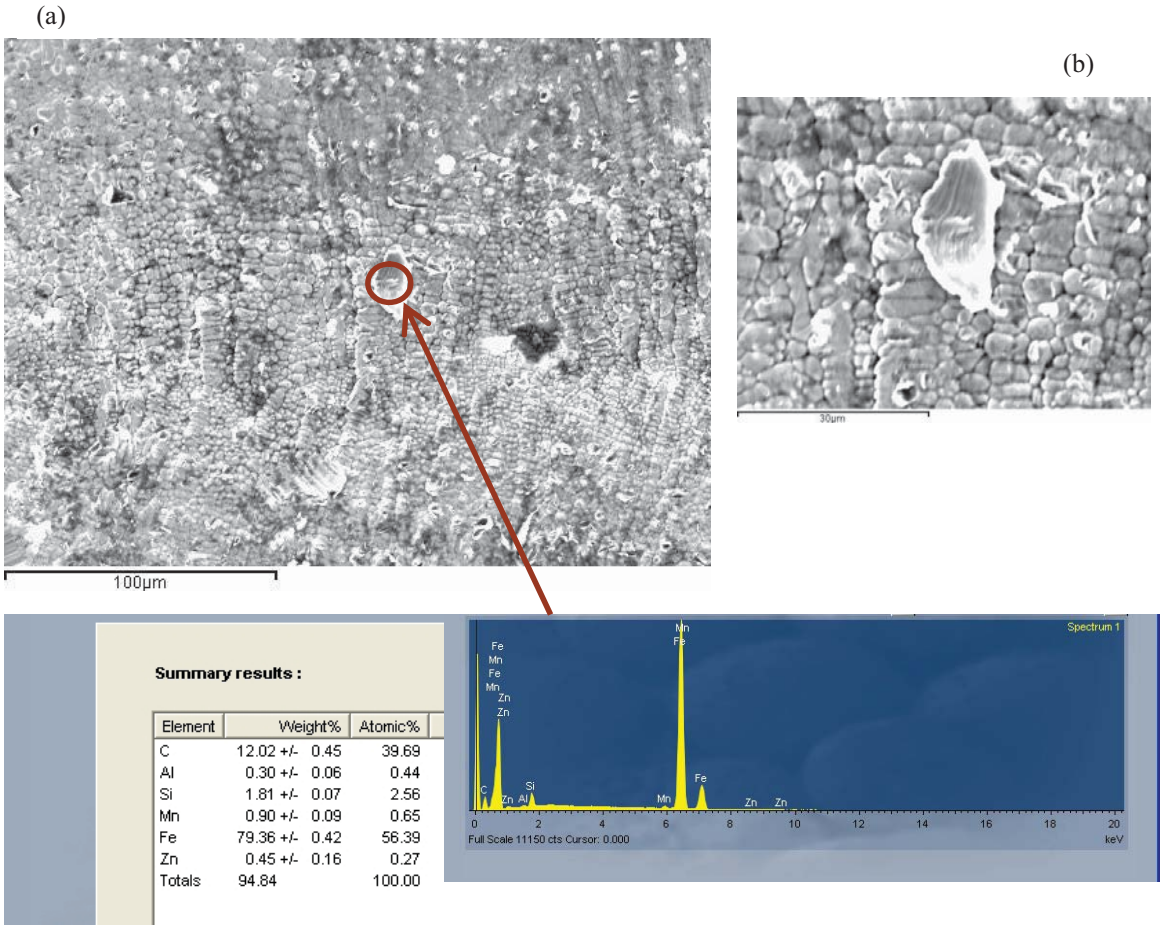

Figure 4.13 Scanning electron micrograph of U-TR sample near TRIP base metal at 500X showing grainy surface and droplets (a). Spectral analysis of a droplet showed that it consisted of aluminum and zinc in addition to iron and other elements. (b) A close-up of the droplet shown at 2000X.

The surface of the U/DP weld also seemed to contain spatters of metal. Figure 4.15 shows the top of the surface near DP base metal with several spatters. Spectral analysis of one of these spatters indicates that they are rich in aluminum. Since DP980 contains only about 0.45% of Al by weight and the spatter is about 6% Al by weight, the spatter mostly came from the USIBOR side of the joint. Another point of interest is that many of these spatters seemed to be at the edge of the weld and beyond on the DP980 base metal surface.

An examination of U/DP sample revealed that the top surface of the weld near the USIBOR base metal to be relatively free of spatters and being smoother when compared to the surface near the DP980 base metal. The results of the SEM examination leads to the conclusion that the shielding gas blown in a direction perpendicular to the direction of welding results in the spatters that could have influenced the results of

roughness and waviness values obtained. Both aluminum and zinc seem to have affected the surface roughness. The results also strongly suggest that the roughness and waviness values can be location dependent and more detailed data collection is needed to arrive at a better correlation between surface roughness measurements and the standard deviation values.

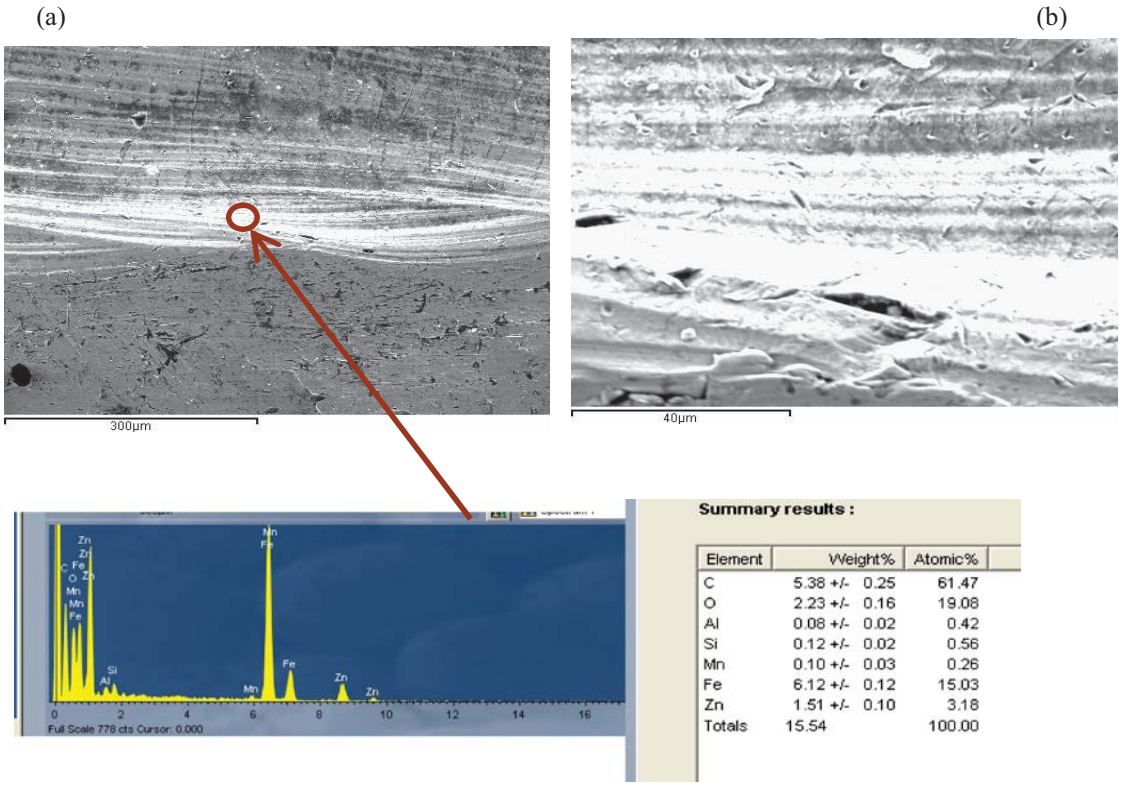

Figure 4.14 Scanning electron micrograph of U-TR sample near USIBOR base metal (a) shown at 200X revealing the grainy surface droplets and (b) at a higher magnification of 1300X. Spectral analysis of a small region again showed that it consisted of aluminum but it was richer in zinc compared to the droplet shown in Figure 4.13

4.3.5 Practical implications of the test results

From this study, it has become clear that the surface roughness and concavity issues observed in the weld regions might lead to significant functional issues such as premature fracture and reduced fatigue life. The concavity due to deep ridges leads to lower thickness in local regions which can result in higher stresses and potentially fail in those areas. Rough surface profiles are always an item of concern in the fatigue life of the products.

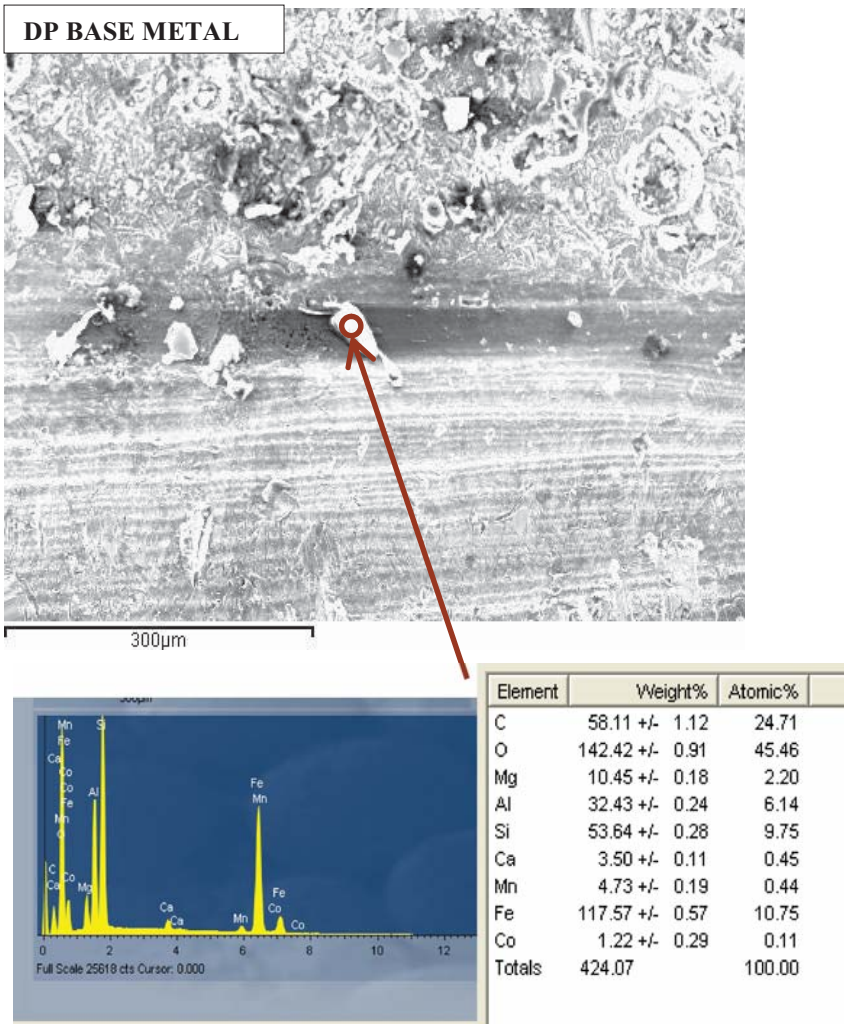

Element	Weight%	Atomic%
C	58.11 +/- 1.12	24.71
O	142.42 +/- 0.91	45.46
Mg	10.45 +/- 0.18	2.20
Al	32.43 +/- 0.24	6.14
Si	53.64 +/- 0.28	9.75
Ca	3.50 +/- 0.11	0.45
Mn	4.73 +/- 0.19	0.44
Fe	117.57 +/- 0.57	10.75
Co	1.22 +/- 0.29	0.11
Totals	424.07	100.00

Figure 4.15 Scanning electron micrograph of U-DP sample near DP980 base metal shown at 180X. From the spectral analysis, it appears that the spatters are rich in aluminum. The spatters also seemed to occur at higher frequency near DP base metal.

It should be noted that the spatters of aluminum may not be eliminated during subsequent hot forming operation. The layer of aluminum coating containing 10% silicon has a melting temperature of 600°C. However, during the subsequent heating operation to austenitizing temperature of about 900°C in the oven before hot forming operation, the coating or the spatters form a Fe-Al-Si intermetallic compound that starts at the interface with the base metal and migrates to the surface [16]. The melting point for this intermetallic compound is much higher than 900°C used for austenitizing process. On the other hand, the hot dip galvanizing (GI) process resulting in a Fe-Zn-Al intermetallic compound would have melting temperature in he

range of 600-700C and would melt during the austenitizing process. This could lead to possible contamination of the dies during hot forming process.

4.4 Conclusions

In this investigation, the size and shape variability of the weld zones was evaluated for laser welded AHSS steels with various combinations of types (TRIP780, DP980 and USIBOR), coatings (aluminized and galvanized) and thicknesses (1 mm, 1.5 mm and 1.8 mm). All these combinations were also examined for surface roughness and waviness. Scanning electron microscope was used to identify the role of aluminum and zinc on the roughness parameters. Following conclusions were reached.

(1) Larger thickness differentials between samples being welded could lead to higher variability in the weld area. In the investigation, 1.8 mm thick USIBOR (aluminized) welded to 1 mm thick TRIP-780 (galvanized) exhibited highest variability in the weld zone. This observation was confirmed by standard deviation values computed by an examination of several sections of the combinations studied as well as measurement of surface roughness of the welds.
(2) A fair correlation between standard deviation values and roughness parameters has been obtained for the combinations studied.
(3) Scanning electron microscope confirms that spatters of metal containing aluminum and zinc caused higher roughness values for USIBOR:TRIP780 combination. This phenomenon also appears to have occurred in USIBOR:DP980 combination although to a lesser degree.
(4) Since the galvanized layer could melt at austenitization process and further contaminate the dies, it is recommended that galvanization be avoided on laser-welded TWB's that are hot-formed.
(5) If tailor welded samples contain protective coatings such as aluminum, the surface profile of the welded area needs to be examined carefully. Such protective coatings may result in larger surface variability potentially to the detriment of tensile, fatigue and impact performance.
(6) SEM study also suggests that surface roughness values can vary considerably from one region to another. For example, on USIBOR:DP980 combination, surface roughness appears to be lower near USIBOR base metal region compared to DP980 base metal region.

Acknowledgements

The authors wish to thank Ford Motor Company in general for their support of this project. In particular, Matt Zaluzec, John Bonnen, James Boileau, Ron Cooper, Jon Hangas, Shannon Bollin, Brian Sullivan and Shirleen Holland of Ford Motor Company are thanked for their invaluable help and support. Ron Cooper was especially helpful with suggestions for which he is sincerely thanked. Thanks are due to Benda Yan and Matt Gallagher

of Arcelor Mittal for providing the TRIP and DP materials and Raj Mohan Iyengar of Severstal Inc for providing mild steel material. Finally, the invaluable help of Juergen Stollhof, David Havrilla and Hans Leidich of Trumpf Inc in getting the samples welded is also gratefully acknowledged.

References

[1] Gope N, Rout DK, Mukherjee S, Jha G, Bhagat AN, Verma AK, Bhattarjee D. High Strength Steels for Automotive applications: Recent Trends and Experience at Tata Steel. SAE Transactions 2005; 26; 333-344

[2] Bhadeshia H, Honeycombe R. Steels: Microstructure and Properties. Oxford, UK: Butterworth-Heinemann; 2006

[3] http://www.thefabricator.com/AutomationRobotics/AutomationRobotics_Article.cfm?ID=130

[4] Shao H, Gould J, Albright C. Laser Blank Welding of High-Strength Steels. Metallurgical and Materials Transactions 2007; 38; 321-31.

[5] Yan B, Gallagher M. Strength and Fatigue of Laser Butt Welds for IF, HSLA and Dual Phase Sheet Steels. International Symposium on Advanced High Strength Steels for the Ground Transportation Industry, Materials Science and Technology (MS&T); 2006; 2; 87-101.

[6] Gallagher M, Yan B, Nadkarni G, Polon M, Aefferer H, Leidich H. Laser Assembly Welding of Advanced High Strength Steels. Advanced Laser Applications Conference and Exposition 2005; 3; 49-62.

[7] Xia M, Sreenivasan N, Lawson S, Zhou Y, Tian Z. A comparative Study of Formability of Diode Laser Welds in DP980 and HSLA Steels. ASME Transactions July 2009; 129; 446-452.

[8] Anand D, Chen DL, Bhole SD, Andreychuk P, Boudreau, G. Fatigue behavior of tailor (laser)-welded blanks for automotive applications. Materials Science and Engineering A 2006; 420; 199-207.

[9] Sharma RS, Molian PA. Yb:YAG laser welding of TRIP780 steel with dual phase and mild steels for use in tailor welded blanks. Materials & Design December 2009; 30; 4146-4155

[10] Rajarama N, Sheikh-Ahmad J, Cheraghi, SH. CO2 laser cut quality of 4130 steel. International Journal of Machine Tools and Manufacturing March 2003; 43; 351-358.

[11] Tzeng, Y. Effects of operating parameters on surface quality for the pulsed laser welding of zinc-coated steel. Journal of Materials Processing Technology April 2000; 100; 163-170.

[12] Kou, S. Welding Metallurgy. Hoboken, NJ; John Wiley and Sons; 2002.

[13] Wadsworth HM. Handbook of statistical methods for engineers and scientists. McGraw Hill, New York, 1997.

[14] Scheers J, Vermeulen M, De Mare C, Meseure K. Assessment of Steel Surface Roughness and Waviness in Relation with Paint Appearance. . International Journal of Machine Tools and Manufacturing 1998; 38; 647-656.

[15] Rizzi P, Bellingeri S, Massimino F, Baldissin D, Battezzati L. Microstructures in laser welded high strength steels. Journal of Physics, The 13th International Conference on Rapidly Quenched and Metastable Materials; 144; 2009.

[16] http://www.nsc.co.jp/en/tech/report/pdf/n8805.pdf

[17] http://galvinfo.com/ginotes/GalvInfoNote_1_3.pdf

CHAPTER 5. WELDABILITY OF ADVANCED HIGH STRENGTH STEELS USING AN Yb:YAG DISK LASER

Paper published in Journal of Materials Processing Technology 211 (2011) 1888-1897
Rajashekhar S Sharma and Pal Molian

Abstract

In this paper, weldability results of 1030 nm, 6 kW Yb:YAG disk laser welding of various combinations of advanced high strength steels (transformation induced plasticity steel, dual phase steel and boron steel) of 1 to 2 mm thickness are presented. Weldability is expressed in terms of penetration, weld profile, weld defects, microhardness and melting efficiency. Full penetration keyhole welds with hour-glass shape were produced. Microhardness measurements indicated a substantial increase in hardness in the weld zones, attesting the superiority of laser welding. Analyses revealed that the typical melting efficiency is on the order of 50 to 70% for full penetration welding. Tensile test results confirmed the high quality of the welds obtained.

5.1 Introduction

Historically fusion welding processes based on arc and resistance are utilized to manufacture automotive structures. New welding processes have emerged over the years; however acceptance is generally slow due to the design changes required to accommodate such processes. Laser welding has been in existence for over four decades and has gradually replaced resistance mash seam welding for tailor welded blanks (TWB) in the automotive industry. TWB welds blanks of different materials, thicknesses, and coatings before the blank goes through metal-forming process, leading to lighter, less expensive parts that are functionally superior.

Laser welding offers the benefits of low heat input per unit volume, small heat affected zone (HAZ), low thermal distortion of the workpiece, fewer welding defects, high welding speed, and, deep and narrow weld profiles. In addition, it allows easy automation while welding complex joint configurations and dissimilar materials. Like other welding techniques, laser welding has its share of drawbacks that include the need for almost press fitting of parts due to its small focused spot size, high equipment and operating costs, lower welding speeds for joints with a gap greater than 0.5 mm, low electrical efficiency of the laser and, in cases of certain lasers, difficulty in welding high reflective materials like aluminum.

The most common lasers used for TWB are the industrial workhorse CO_2 (λ=10,600 nm) and diode-pumped Nd:YAG (λ=1064 nm). Recent innovations in laser design have led to the development of two novel lasers for welding applications: one is fiber laser and other is disk type. Ream (Ream, 2005) has made an extensive

analysis of the comparison of four lasers (CO_2, Nd:YAG, fiber and disk) for welding mild steel in the power range of 4 - 5 kW (Figure 5.1). He suggests that with the emergence of high-power disk and fiber lasers, the competitive landscape has expanded. Fiber and disk lasers exhibit multi-kilowatt powers in continuous wave mode, high efficiency, compact design and excellent beam quality that produce deep penetration welds at high-welding speeds. Quintino et al (Quintino et al., 2007) explains that the high electrical efficiency of the fiber laser greatly reduces operating costs while resulting in better beam quality, with very low divergence, allowing small spot diameters. They present initial data on welding of X100 pipeline steel with a 8 kW laser and obtained high melting efficiencies. Kawahito et al (Kawahito et al., 2008) used a 6 kW fiber laser to obtain deep penetration welds with narrow widths in 8 mm thick plate at a high welding speed of 4.5 m/min, and later used a 2.5 kW laser beam to weld Zr55Al10Ni5Cu30 metallic glass at very high speeds of 72 m/min.

The disk laser (Yb:YAG at 1030 nm) with powers in the 2 to 8 kW range is claimed to have the best beam characteristics among industrial lasers for welding (Kim et al., 2008). Yb:YAG is the most widely used lasing medium for thin-disk lasers because of its long radiative lifetime (~950 μs), high thermal conductivity (~6 W/m K) and good mechanical properties. Unlike Nd:YAG rod types, the disk has no thermal lensing, resulting in absence of optical distortion and keeping constant beam quality over the entire power range. Since the disk laser is not sensitive to back reflection, these lasers allow longer fiber lengths for beam delivery and thereby remote welding, as enumerated by Havrilla (Havrilla, 2005). Disk laser also offers the advantages of improved penetration and higher melting efficiency. It may be noted here that melting efficiency is defined as the ratio of the theoretical amount of energy required to melt the volume of metal compared to the delivered laser energy. In addition, absorptivity studies of various materials showed that the disk laser has an edge over CO2 and Nd:YAG lasers. Disk lasers have been successfully used to weld aluminum alloys by varying the focal point position and incident beam angle (Kim et al., 2008). It is expected that the disk and fiber lasers eventually replace conventional laser systems due to their higher quality (Kim et al., 2008). These lasers are rapidly gaining momentum in the industry because of the cost-effectiveness compared to Nd:YAG (Table 5.1) and improved quality of welded joints. It can be noted here that Volkswagen has been using both fiber and disk lasers and found that the operating costs for the disk laser is even lower than that of fiber for a three-shift welding production process over a period of eight years (Anderson, 2007).

Advanced high strength steels (AHSS) are promising solutions for the production of lighter automobiles with increased passenger safety and reduced fuel consumption (Mallen et al., 2008). AHSS grades include: (a) Dual-phase (DP) steels, which consist of a dispersion of islands of hard martensite (5 to 20% by volume) in soft ferrite matrix. These steels are characterized by high work hardening and are used in automobile components that require high strength, good crashworthiness and reasonable formability. (b) Transformation-induced plasticity (TRIP) steels that offer high strength and toughness combination with excellent uniform elongation. TRIP steels have the ability to absorb more energy during crash due to the delayed transformation

of retained austenite to martensite. They have a microstructure consisting of various fractions of ferrite, martensite, bainite and retained austenite, giving them their unique balance of properties. However, the higher percentage of alloying content and thermal cycle in welding, limits its weldability resulting in inferior microstructure and mechanical properties of the weld. (c) Boron-alloyed (MnB) steels, trademarked as USIBOR, which are more widely used by automakers today. Essentially this steel is hot stamped by heating the blank to austenitization temperature, press formed and die-quenched, resulting in very hard phases that give rise to extreme tensile strength of 1500 MPa. Other AHSS materials used by automakers are high hole expansion (HHE), complex-phase (CP), and martensitic steels. Figure 5.2 shows the optical micrographs of DP, TRIP and USIBOR steels.

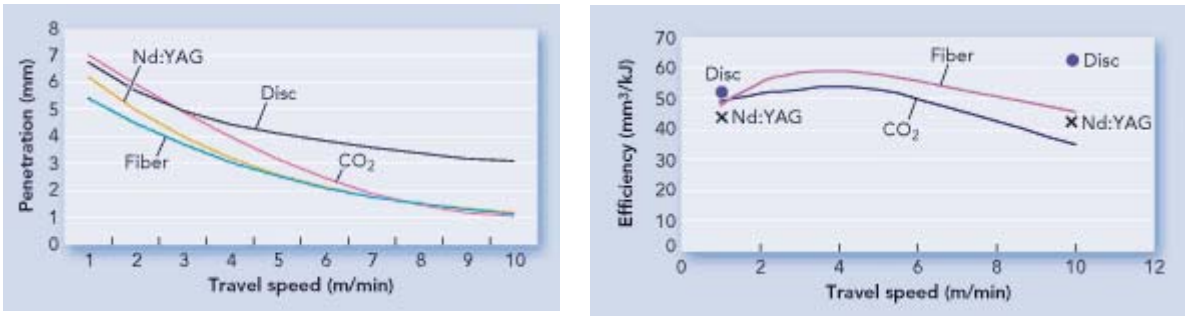

(a) **(b)**

Figure 5.1 Comparison of four different lasers for welding mild steels with Power~ 4-5 kW. (a) Travel speed versus penetration (b) Travel speed versus efficiency [*Ream, 2005*]

Table 5.1 Operating and maintenance costs for lasers (Ream, 2005)

Expenses ($/hour)	CO_2	Nd:YAG	Fiber	Disc
Depreciation and interest	$7.50	$15.30	$13.20	$18.10
Replacement Parts	$3.10	$6.80	$1.90	$11.10
Electric	$4.70	$8.90	$2.10	$1.90
Maintenance	$3.30	$3.80	$2.10	$1.90
Floor Space	$1.90	$2.10	$0.70	$1.20
Welding and Laser Gas	$3.80	$1.70	$1.40	$0.90
Total	$24.30	$38.60	$21.40	$35.10

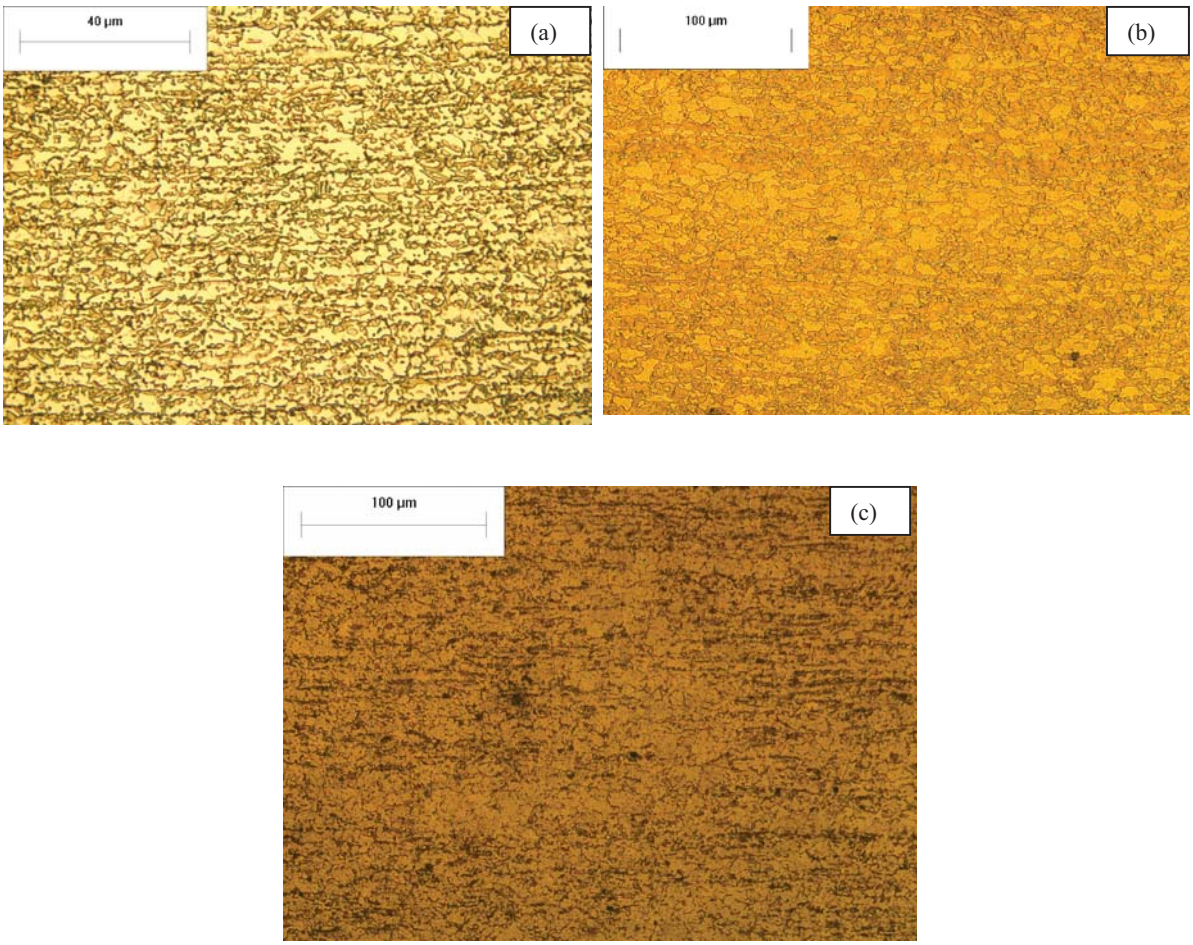

Figure 5.2 Microstructures of the three advanced high strength steels used in the study: (a) TRIP780 shown at 1000X magnification, (b) DP980 at 400X and (c) USIBOR shown at 400X. USIBOR microstructure is shown before austenitization and quenching.

Heat transfer characteristics during laser welding are of great interest to researchers. Several models ranging from simple analytical models involving moving line heat-source to elegant numerical models which account for fluid dynamics and laser–plasma interaction have been proposed in the literature. Swift-Hook and Gick (Swift-Hook and Gick, 1973) provide a simple theory that provides a good description of penetration welding for both electron beams and lasers. Steen et al (Steen et al., 1988) provide an analytical form for the temperature distribution; they have estimated weld profiles and compared them with examples of actual welds. Dowden et al (Dowden et al., 1985) have considered the interaction of conditions in the liquid metal

surrounding the keyhole formed and have developed a model for the energy interface and vapor flow in the keyhole. They have then used the model to calculate keyhole shapes and the variation of depth of the related quantities. Kaplan (Kaplan, 1994) has developed a model taking into account a point-by-point determination of the energy balance at the keyhole wall, deriving a formula for heat conduction from the model of a moving line source of heat, modeling the absorption mechanism and also considering the thermodynamics and the flow of metal vapor inside the keyhole. Huntington and Eagar (Huntington and Edgar, 1982) studied the effect of joint geometry – bead-on-plate, V groove and square groove - on the absorption of laser energy with the same laser power and found better absorption of laser beam energy in grooved joints.

All these models predict different results due to various assumptions and use of a number of different parameters such as keyhole size, material properties and absorptivity. The model proposed by Lankalapalli et al (Lankalapalli et al., 1996) relates the penetration depth to the incident laser power and the Peclet number, the latter being a function of the welding speed, the keyhole radius and thermal diffusivity. The relative importance of conduction and convection in the overall transport of heat in the weld pool can be assessed from the value of the Peclet number. For steel keyhole welding, Peclet number is much greater than 1 implying that convection of melt pool is more dominant than conduction (Zhao and DebRoy, 1999).

In this paper, a study of weldability of different combinations of advanced high strength steels (AHSS) using a 6 kW Yb:YAG laser is reported. A high power laser beam produced by TRUMPF (TruDisk 6002), transported to the work location using fiber optic technology was used, since such applications are most suitable for industrial use, and the high quality laser beam can be transported with minimal distortion of the laser beam. Since the cost gap is closing between disk and fiber lasers, a strong case can be made for the disk lasers in the cost arena too. Since a combination of AHSS and laser welding is becoming very popular, there is considerable interest in the automotive industry for evaluating the application of newer lasers for the joining of AHSS. Material section thicknesses ranged from 1 to 2 mm and keyhole welding was conducted. Weldability has been expressed in terms of penetration, weld profile, flaws, microhardness and welding efficiency. Two models have been used to arrive at conclusions regarding the melting efficiency. Using calculations, conclusions on how these models need to be used in practice have been drawn.

5.2 Experimental details of laser welding

Three grades of AHSS (TRIP780, DP980 and USIBOR) and mild steel (MS, AISI 1008) were obtained in the form of 1 mm (MS, TRIP), 1.5 mm (DP) and 1.8 mm (USIBOR) blanks. TRIP steels were pre-strained to 5% (designated TR-5) and 10% (designated TR-10) in an Instron machine. TRIP steels not pre-strained (designated TR-0) were also evaluated. The grades, compositions and mechanical properties of these steels are listed in Table 5.2 (a) and (b). Weld coupons of the size 100 mm x 200 mm were prepared and cleaned to ensure that all

samples had same surface finish. The coupons were mounted in a fixture as shown in Figure 5.3 with good clamping and a joint gap of less than 10% of thickness. The weld configuration was set as square groove, butt joint.

The specific disk laser used was continuous wave type with a power capacity of 6 kW and beam quality of 8 mm-mrad. It was manufactured by TRUMPF (TruDisk 6002). By comparison, a traditional lamp-pumped Nd:YAG would deliver 4 kW to the workpiece with beam quality of 25 mm•mrad. The laser beam was transmitted through optical fiber and focused on the specimen surface by the lens with 200 mm focal length. The spot diameter at the focal point was about 0.6 mm. The system comprises of the laser beam delivery system mounted on the robot's end-effector and moving in 3D space, with the beam perpendicular to the workpieces for all combinations except those involving USIBOR; for the USIBOR combinations, the beam was tilted at an angle of 6° to the vertical to account for large thickness differences between USIBOR (1.8 mm thick), and, mild steel and TRIP780 stock (both 1.0 mm thick). The samples were held stationary in the weld fixture.

Table 5.2 (a) Chemical compositions (wt%) of TRIP780, DP980, USIBOR and mild steel used.

Steel	C	Mn	Mo	P	S	Si	Cr	Al	B	Ti	V	Nb	Ni	Cu	N
USIBOR 1500P	0.220	1.100	0.003	0.012	0.003	0.264	0.172	0.051	0.0023	0.040	0.005	0.001	0.009	0.028	0.004
DP980	0.135	2.100	0.350	--	--	0.050	0.150	0.450	0.007	--	--	--	--	--	--
TRIP780	0.190	1.580	--	0.013	0.025	1.600	0.070	0.036	--	0.027	--	0.038	0.020	0.020	
Mild Steel	0.043	0.270	0.002	0.041	0.009	0.021	0.020	0.040	0.000	0.002	0.001	--	--	--	0.007

Table 5.2 (b) Mechanical properties of TRIP780, DP980, USIBOR and mild steel used.

Steel	Yield strength (MPa)	Ultimate strength (MPa)	Elongation (%)
DP980 CR	534	980	12.2
TRIP780 CR	471	792	18
MILD STEEL	215	355	37.8
USIBOR (before austenitization and quenching)	450	600	25
USIBOR (after austenitization and quenching)	1100	1500	6

Initially bead-on-plate experiments were performed to obtain the appropriate laser parameters for butt welding. However a small change in the parameters has to be made for butt joints because the joint geometry can change

the absorption of laser energy. A set of keyhole welding experiments was conducted with three levels of laser power and two levels of welding speed as shown in Table 5.3. Argon was used as assist gas at a flow rate of 30 l/min. After welding, the specimens were cut from transverse sections at the mid-length position of the welds and the cut surfaces prepared for metallographic inspection by polishing and etching using a 3% nital solution to display weld shape and microstructure. Microhardness was evaluated using a Vicker's hardness tester at a load of 0.5 kN.

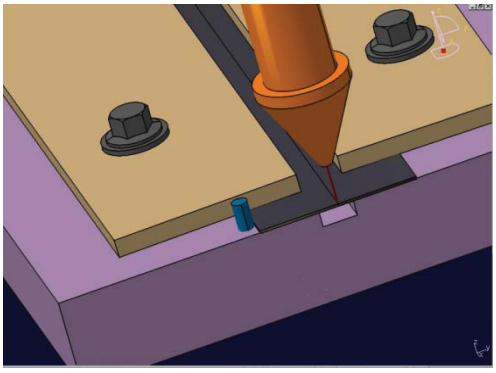

Figure 5.3 Laser welding fixture

5.3 Results

5.3.1 Microstructure and microhardness

Figure 5.4 shows top views of several welds. For the combinations involving TRIP780, DP980 and MS, the top of the welds are relatively clean, while U/TR and U/DP combinations show spatters. These spatters have been determined to be metal alloys from the zinc and aluminum coatings and blown by the shielding gas during the welding process (Sharma et al., 2010). Figure 5.5 (a) - (f) show optical micrographs of the transverse sections for six combinations (TR-0/MS-70, TR-0/DP-70, DP/MS-150, U/MS, U/TR and U/DP). The corresponding microhardness values for the combinations are shown in Figure 5.6 (a) – (b).

Table 5.3 Weld combinations used in the study.

Sample Designation	Weld Metals	Laser Power, kW	Welding Speed, mm/sec
TR-0/MS-70	TRIP-O (1 mm) to MS (1 mm)	2	70
TR-5/MS-70	TRIP-5 (1 mm) to MS (1 mm)	2	70
TR-10/MS-70	TRIP-10 (1 mm) to MS (1 mm)	2	70
TR-0/DP-70	TRIP-O (1 mm) to DP (1.5 mm)	2	70
TR-5/DP-70	TRIP-5 (1 mm) to DP (1.5 mm)	2	70
TR-10/DP-70	TRIP-10 (1 mm) to DP (1.5 mm)	2	70
DP/MS-70	DP (1.5 mm) to MS (1 mm)	2	70
TR-0/MS-150	TRIP-10 (1 mm) to MS (1 mm)	3.7	150
TR-5/MS-150	TRIP-5 (1 mm) to MS (1.5 mm)	3.7	150
DP/MS-150	DP (1.5 mm) to MS (1 mm)	3.7	150
U/MS	USIBOR (1.8 mm) to MS (1 mm)	4.5	150
U/DP	USIBOR (1.8 mm) to DP (1.5 mm)	4.5	150
U/TR	USIBOR (1.8 mm) to TRIP-0 (1 mm)	4.5	150

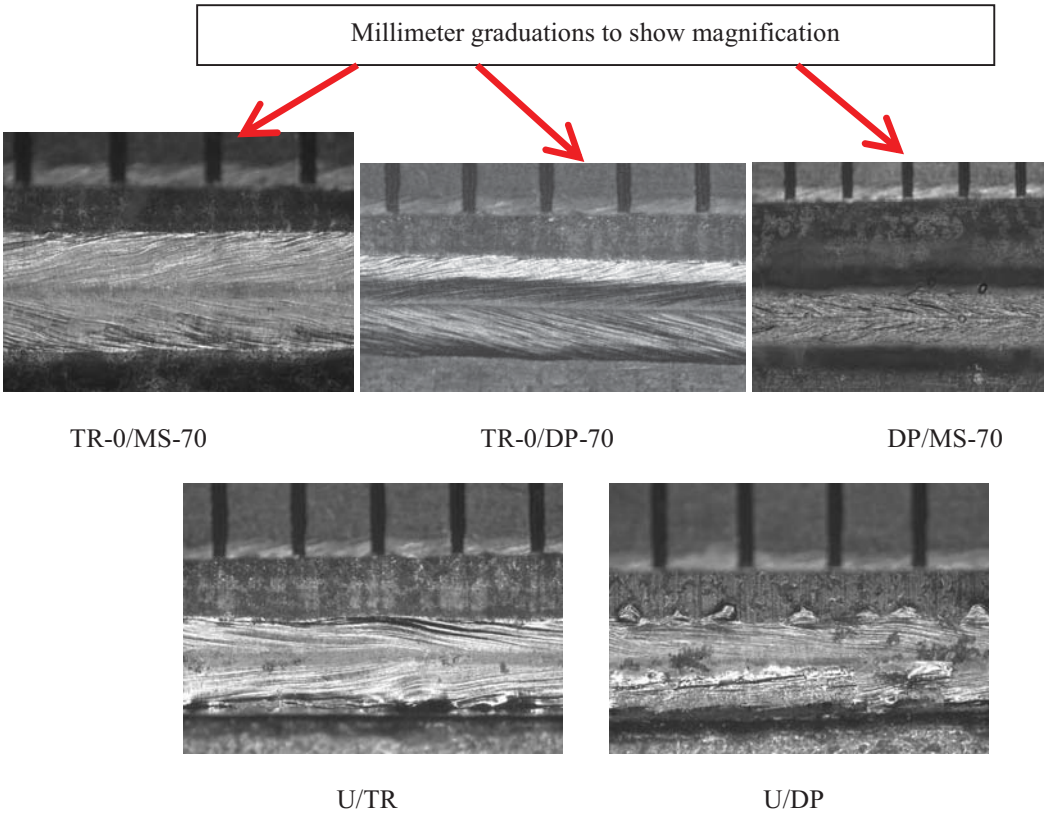

Figure 5.4 Top views of laser welded sample combinations. Magnification level is indicated by the mm graduations shown in each micrograph.

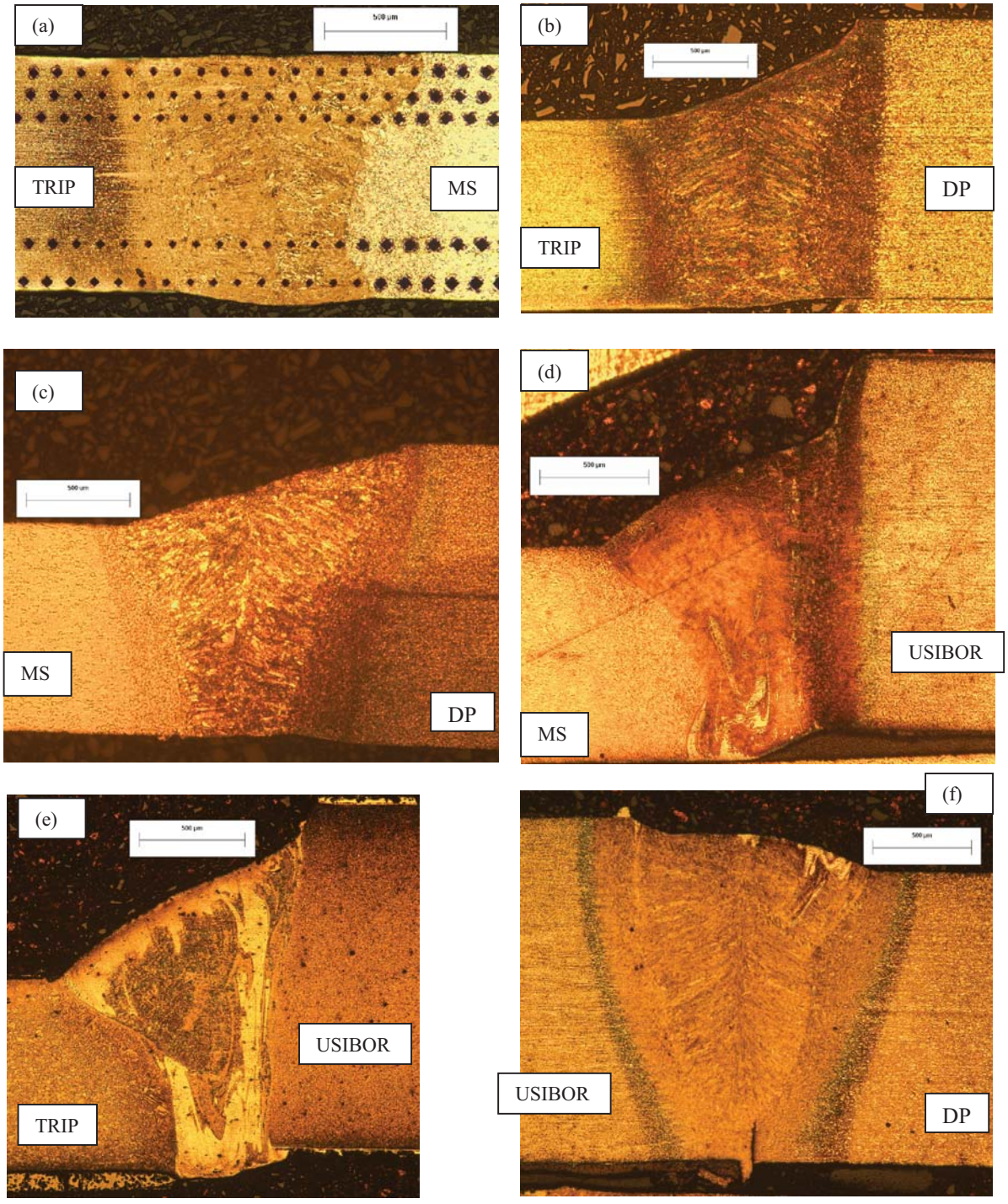

Figure 5.5 Optical micrographs at 50X magnification of the fusion zones for (a) TR-0/MS-70 [TRIP-0 welded to MS at 70 mm/sec and 2 kW power] (b) TR-0/DP-70 (c) DP/MS-150 (d) U/MS combination [USIBOR welded to MS at 150 mm/sec using 4.5 kW power] (e) U/TR, and, (f) U/DP.

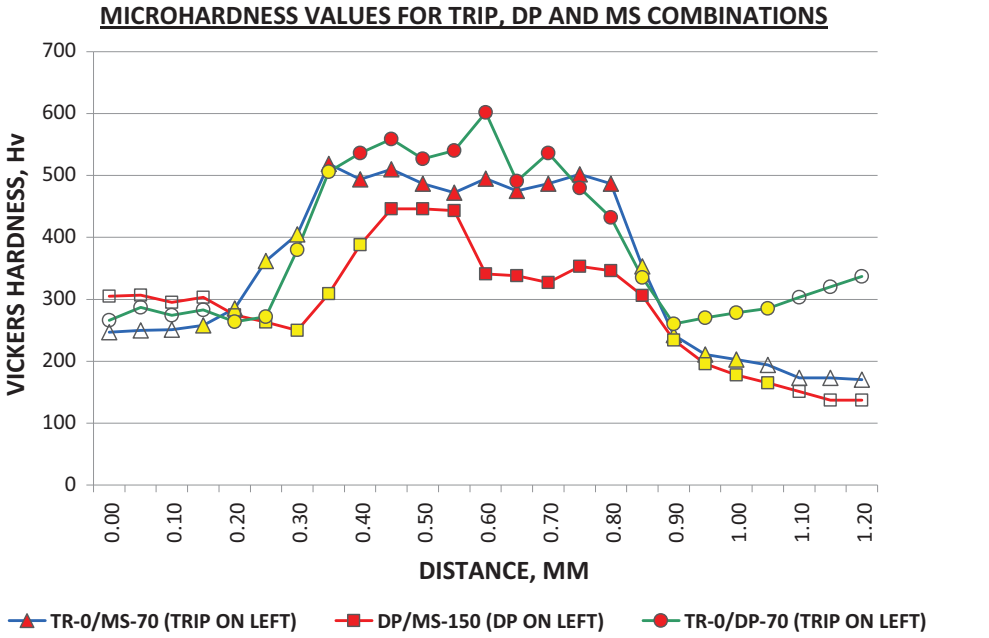

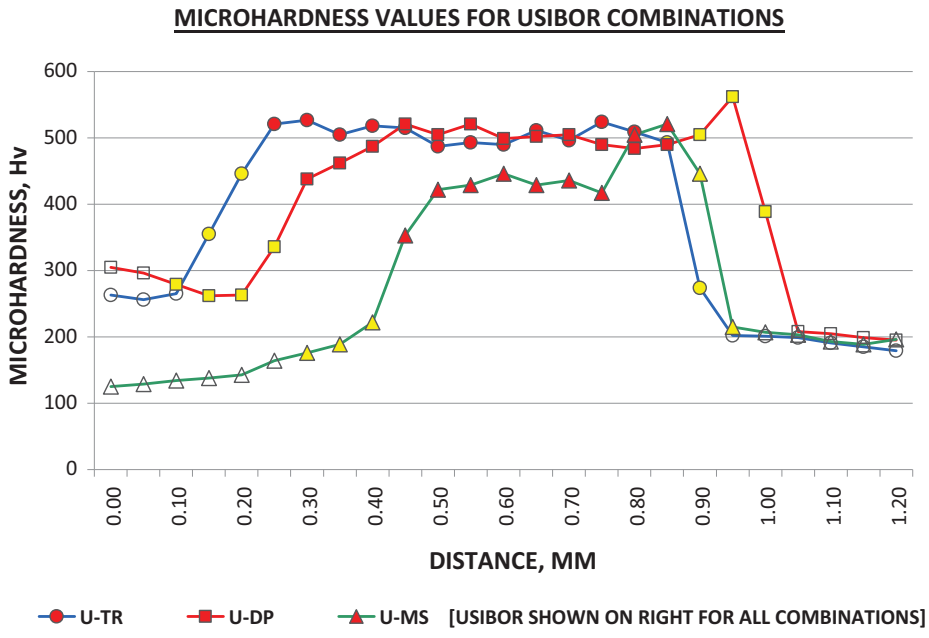

Figure 5.6 Microhardness values for the six combinations studied.

5.3.2 Tensile tests

Tensile tests were carried out for the combinations studied. The sample dimensions had a nominal width of 6 mm and a gage length of 42 mm. The sample dimensions are shown in Figure 5.7. Each sample was measured for width to normalize for errors. The USIBOR combinations were not austenitized before the tests.

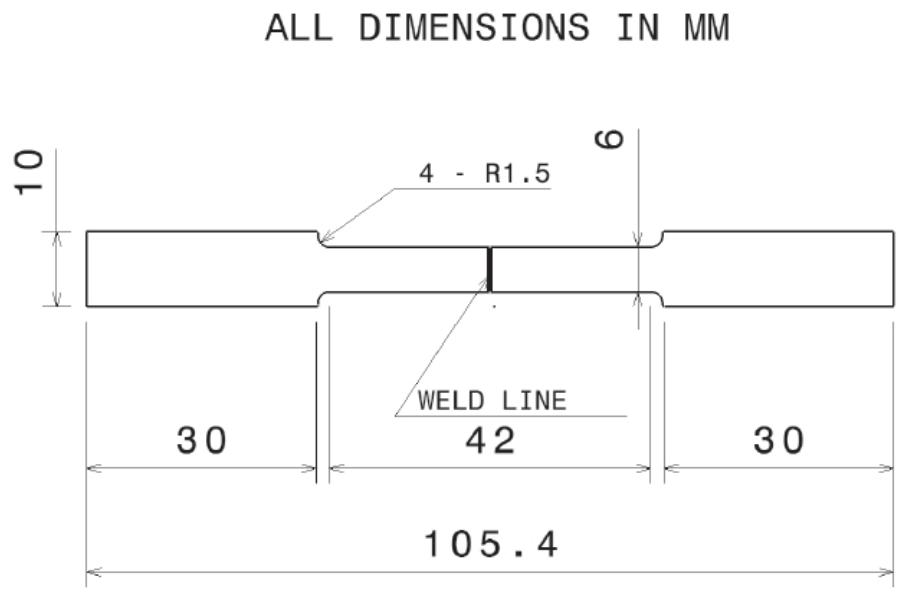

Figure 5.7 Dimensions for the tensile test samples.

Figure 5.8 shows fractured samples from the tensile test. As can be seen, for TR-0/MS-70, DP/MS-150 and U/MS combinations, the fracture occurred in the mild steel section (1.0 mm thick), while for U/TR, the thinner (1.0 mm thick) TRIP780 material fractured. In the case of TR-0/DP-70 combination, TRIP portion, which is relatively softer (compared to DP980) and thinner (1.0 mm compared to 1.5 mm for DP980), fractured. In the case of U/DP combination, the fracture occurred in the softer USIBOR section. This is because, although USIBOR material was 1.8 mm in thickness compared to a thickness of 1.5 mm for DP980, since USIBOR in this test was not austenitized and quenched, it had lower tensile strength compared to DP980. None of the fractures occurred in the weld regions. Since microhardness values in the weld regions are found to be considerably higher than either of the sample materials welded [Figure 5.5 (a) - (f)], these results agree with the results of the microhardness evaluations.

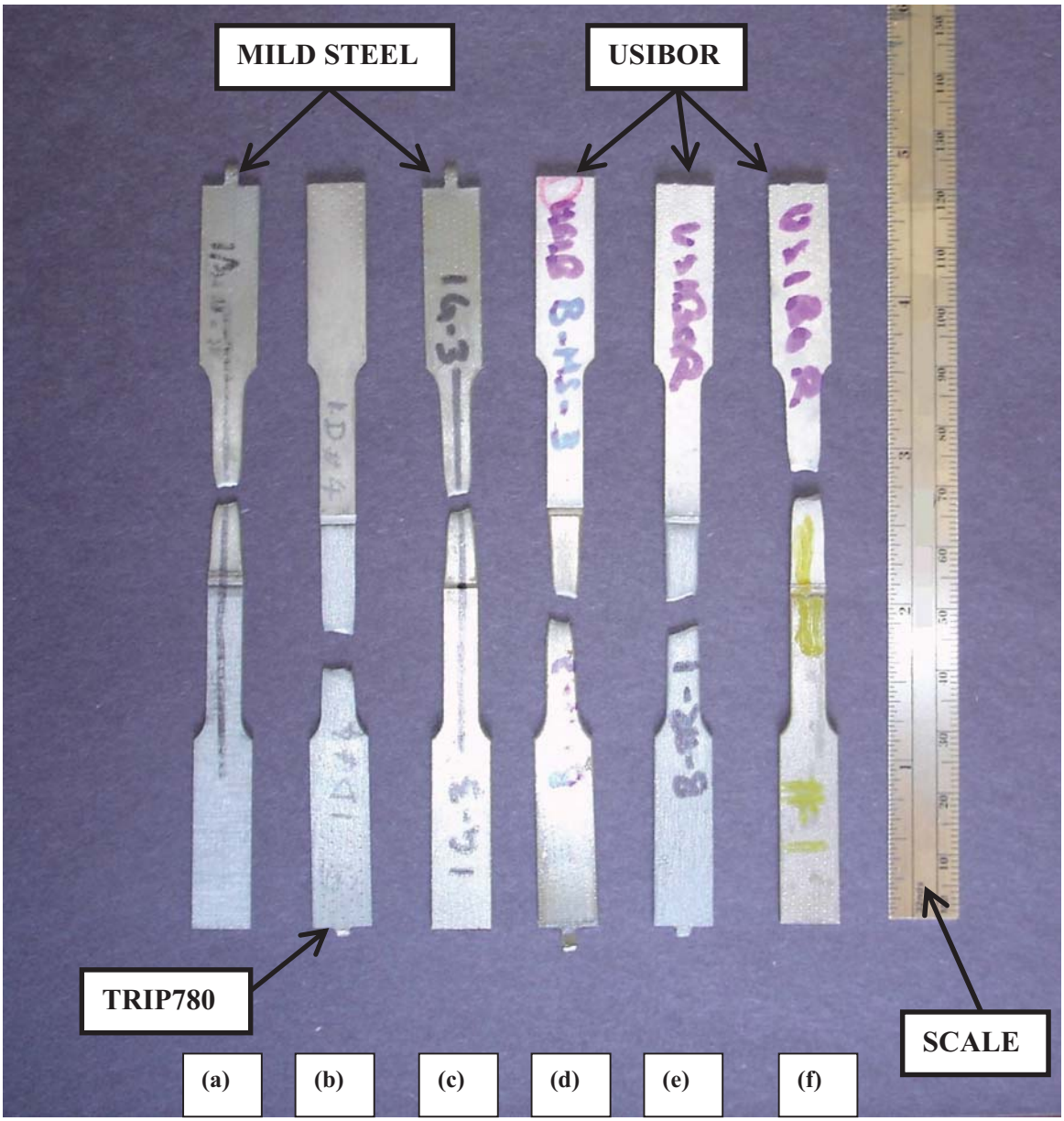

Figure 5.8 Fracture samples from the tensile tests for the six combinations studied. (a) TR/MS-70, (b) TR/DP-70, (c) DP/MS-150, (d) U/MS, (e) U/TR and (f) U/DP. A scale is included to indicate magnification. The mild steel part in (a), (c) and (d) fractured, while TRIP780 fractured in (b) and (e). In sample (f), the softer USIBOR sample fractured. Magnification is indicated by the steel scale laid next to sample (f).

The engineering stress versus strain graphs for these combinations are shown in Figure 5.9. As can be seen, the graphs for the three sample combinations involving mild steel (TR-0/MS-70, DP/MS-150 and U/MS) are very close with virtually no difference seen between TR-0/MS-70 and DP/MS-150. U/TR, U/DP and TR-0/DP

combinations exhibit considerably higher load carrying capacity and seem to absorb much larger amounts of energy during the testing. Although fracture occurs in the TRIP portion for TR-0/DP-70 and U/TR combinations, there is slight difference in the tensile strength of the joints; U/TR exhibits over 800 MPa while TR-0/DP-70 fractures close to 800 MPa. This difference is attributed to sample variability.

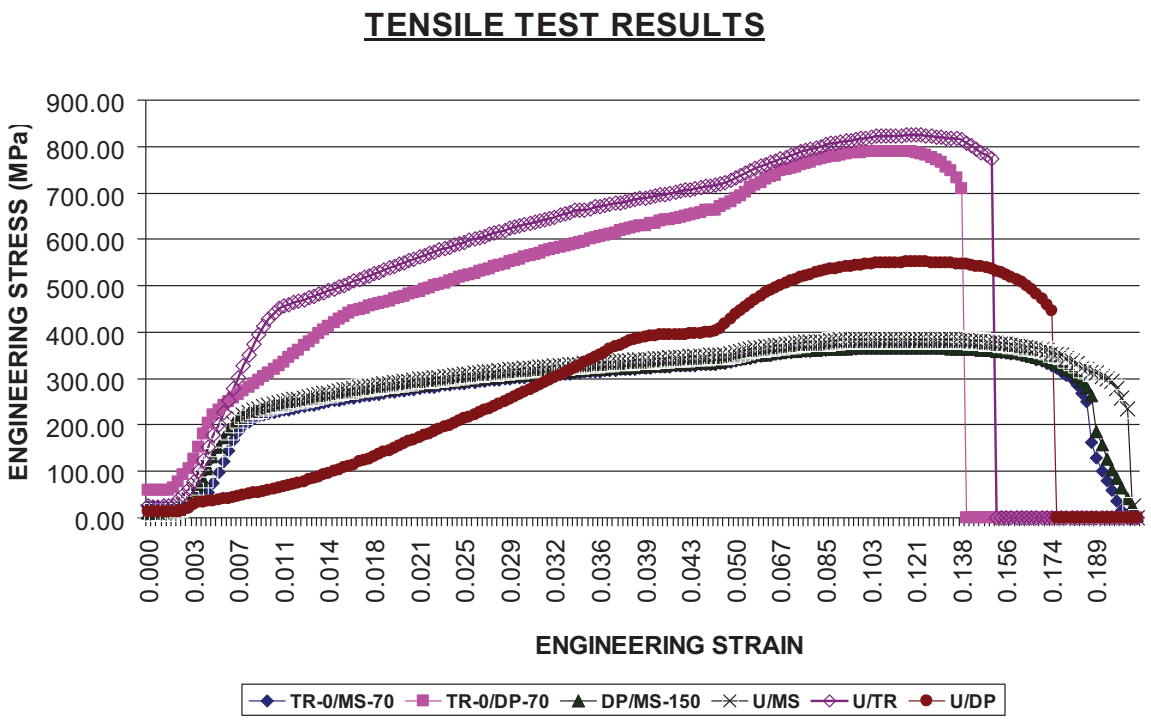

Figure 5.9 Tensile test results showing engineering stress versus strain for the six sample combinations studied.

Since the tensile strengths of steels correspond to microhardness values, if different materials of the same thicknesses are welded, it may be surmised that DP/MS-150, TR-0/MS-70 and U/MS joints would all fracture in the mild steel region, U/DP and U/TR joints would fracture in the USIBOR region and TR-0/DP-70 joint would fracture in the TRIP region. The tensile strengths as well as strains at fracture could be different due to part to part variability as well as the plastic strains experienced by the joint.

5.4 Discussion

5.4.1 Microstructure and microhardness

Reference to Figure 5.5 [(a) – (f)] suggests that all the welds exhibit hour-glass shape, characteristic of keyhole welding. There is no evidence of defects such as porosity, undercut, burn through and humping. However,

there is a slight concavity at the bottom of the joint which is more marked for TR-0/MS-70 weld joint. Minimizing concavity is critical to good formability and mechanical properties and is generally achieved by precision shearing the blank edges to be welded, addition of filler wire and beam spinning during the welding process.

In the fusion zone of Figure 5.5 [(a) – (f)], the microstructure was mostly martensitic with columnar dendrites typically oriented at 30 to 45 degrees in the top to midway regions of most welds. Such columnar growth emanating from base metal towards the center seems to be absent in the fusion zone of U/MS. The circular dendrites found for this combination are attributed to considerable turbulent fluid motion with rapid solidification taking place in this zone. The nature of the planar, cellular or dendritic growth depends upon several conditions such as thermal and constitutional conditions that exist in the immediate vicinity of the liquid-solid interface (David et. al; 2003). As can be seen, U/TR, which has the same thickness differential as U/MS, has instead columnar dendrites as well as a different weld-pool shape. This indicates that a probabilistic model needs to be included along with fluid-flow and heat transfer models to predict the dendritic growth in the weldpool.

The microhardness values were all consistently high in the fusion zone with some values exceeding 500 on Vickers scale. The higher microhardness values observed in the fusion zone of TR-0/DP-70 combination compared to DP/MS-150 and TR-0/MS-70 combinations is attributed to the ease of the formation of hard martensitic substructures in the TRIP/DP combination due to their high hardenability. The heat affected zone (HAZ) of DP980 base metal consistently shows a tendency for softening in regions away from the fusion zone closer to the base metal (HAZ is shown in yellow, while fusion zone is shown in red.) This has been reported earlier in literature. For example, Xia et al (Xia et al., 2009) have studied softening of DP980 HAZ during welding of DP980 to HSLA material. Similarly, Sharma and Molian (Sharma and Molian, 2009) have studied welding of DP980 to mild steel and TRIP780 materials and have observed softening of the DP980 HAZ. One more interesting observation is the high value of hardness in the HAZ of base metal boron steel close to the fusion zone in U/MS [Figure 5.5 (d)] and U/DP [Figure 5.5 (f)] combinations, indicating that the boron alloyed steel close to the HAZ experiences a very high rate of cooling.

5.4.2 Analysis of welding parameters for full penetration

The relationship between laser power and welding speed obtained for full penetration welds is shown in Table 5.3. Generally a relationship between welding speed and power for the same material combination will exhibit a linear relationship as reported by Quentin et al. USIBOR required higher power partly due to the larger section thickness. It is surprising to note in Figure 5.6 that different chemistry and thermal properties of AHSS steels did not significantly affect the penetration. In deep penetration welding, when the laser beam is incident

on the surface, a keyhole surrounded by molten metal is produced. A plasma forms above the keyhole preventing laser energy absorption. The keyhole becomes stable by a balance of surface tension and vapor pressure forces. The keyhole acts like a blackbody with energy absorption of about 90%. The chemistry of the steel dictates evaporation of various elements and subsequent formation of plasma and its properties while thermal properties of the steel should affect heat conduction and convection losses. It appears as though the properties and stability of keyhole are more controlling parameters on penetration than thermal and plasma characteristics.

In this work, a simple moving line source model based on a cylindrical channel surrounded by an elliptical melt pool was used to predict the penetration (Schuocker, 1999). According to this model, the radius of keyhole, r, is given by:

$$r = (4\kappa/V) * \exp [- (Tv * 2\pi * t * K/AP) – 0.577] \quad (5.1)$$

where κ = thermal diffusivity, V = welding speed, Tv = vaporization temperature, t = penetration, K= thermal conductivity, A = absorptivity, P = laser power and * represents multiplication. The constant 0.577 is obtained from an asymptotic approximation of the Bessel's function in the original equation for the melting isotherms in the cases of low welding speed welding (Schuocker, 1999). Since thermal properties of all grades of AHSS steels are not readily available, the properties of DP980 at ambient conditions provided by ArcelorMittal are used: κ = 11 x10-6 m2/sec, Tv = 3023 K and K= 42 W/m K. The radius of keyhole is assumed to be equal to the focused beam radius, 3 x 10^{-4} m while absorptivity is taken as 0.9. Substituting these values in equation (1), the P-V-t relation is given by:

$$V = 0.27 * \exp [-0.886 * (t/P)-0.577] \quad (5.2)$$

where V = m/sec, t = mm and P = kW. Application of equation (2) in the present study yields weld speeds as shown in Table 5.4. As can be seen, for lower power values and smaller thickness samples, the predicted weld speeds of 97 and 87 mm/sec are higher than the 70 mm/sec speed used, resulting in a negative error of somewhat large magnitude. This and the concavity at the bottom of the welds for TR-0/MS-70 samples (Figure 5.5) indicate that for TR-0/MS-70 combination, the speed can be slightly increased without compromising the weld quality. For boron steels, the welding speed predicted by equation (2) at 4.5 kW are 110 and 115 mm/sec, which are considerably smaller than the weld speed of 150 mm/sec used for boron steels. The disagreement in this case is partially attributed to the fact that equation (1) is a solution to heat equation based on Bessel function and is generally valid for low welding speeds (Schuoecker, 1999). An examination of Figure 5.5 (f) indicates that the laser beam has not fully penetrated the U/DP combination, suggesting that slight lowering of

the speed could be beneficial in achieving a well defined weld zone in the bottom by completing the weld penetration.

Table 5.4 Weld speeds predicted by equation (5.2)

	TR-0/MS-70	TR-0/DP-70	U/MS	U/TR	U/DP
Depth of penetration considered, t, mm	1	1.25	1.4	1.4	1.65
Power used, kW	2	2	4.5	4.5	4.5
Weld speed, mm/sec	70	70	150	150	150
Calculated weld speed, V mm/sec	97	87	115	115	110
Error	-39%	-25%	23%	23%	27%

5.4.3 Melting and energy transfer efficiencies

For laser welding, Fuerschbach (Fuerschbach, 1996) defines energy transfer efficiency as the ratio of heat absorbed by the workpiece to the incident laser energy, while he defines melting efficiency as the ratio of the heat necessary to just melt the fusion zone to the heat absorbed by the workpiece. Both melting efficiency and energy transfer efficiency are indicators of how well laser energy is utilized for welding. Fuerschbach uses the following expression for energy transfer efficiency in laser welding and used it for 304 Stainless Steel and 6061 Aluminum.

$$\eta_t = P_a/P_d \tag{5.3}$$

where η_t = energy transfer efficiency, P_a = power absorbed, P_d = power delivered or incident on the workpiece. Power absorbed can be determined using the relationship

$$P_a = [(R_y * \kappa_l 2 * H_m)]/v \tag{5.4}$$

where R_y is Rykalin number (a dimensionless parameter), κ_l = thermal diffusivity at liquidus temperature and H_m = enthalpy of melting. Since Rykalin number is not known, Fuerschbach first computes another dimensionless parameter Christensen number (Ch) defined as:

$$C_h = [v^2 * A/ \kappa_l{}^2] \tag{5.5}$$

Where v = weld speed and A = area of weld. After Christensen number is computed, Rykalin number can be found using the relationship:

$$C_h = R_y * [\{0.48 - 0.29 * \exp(-R_y/6.8)\} * \exp(-R_y/59)] \quad (5.6)$$

Once Rykalin and Christensen numbers are known, melting efficiency is computed as:

$$\eta_m = C_h / R_y \quad (5.7)$$

Application of Fuerschbach's method [equations 3-7] to determine the energy transfer efficiencies and melting efficiencies was carried out for several combinations. For this exercise, a value of κ_l = 6.3 mm2/sec for DP980 supplied by ArcelorMittal was used for all combinations. Since the enthalpy of melting for iron is about 272 J/gm and the percentages by weight of alloying elements in AHSS materials are low, a value of H_m = enthalpy of melting = 274 J/gm, or 2.2 J/mm3 was used for the calculations. The results are presented in Table 5.5 and indicate that the energy transfer efficiencies range from 14% to 19%, while melting efficiencies are in the 47% - 48% range. It should be noted here that Fuerschbach used a value of 8.7 J/mm3 for stainless steel, which when used in these calculations, result in energy transfer efficiencies in the 55% to 74% range, which is more consistent with a value of 87% reported by Fuerschbach. The value of enthalpy of melting, however, seems to have no impact on the melting efficiencies when using these equations.

Table 5.5 Melting and energy transfer efficiencies (Fuerschbach's method)

Characteristic	TR-0/MS-70	TR-0/DP-70	DP/MS-70	DP/MS-150	U/MS	U/TR	U/DP
Area of the weld, mm^2	0.89	1.03	0.90	0.95	0.91	0.97	1.23
Weld speed mm/sec	70	70	70	150	150	150	150
Christensen number, C_h	109.9	126.5	111.4	537.4	514.7	548.2	697.3
Rykalin number R_y	230.6	264.7	233.7	1119.6	1072.4	1142.1	1452.5
Melting efficiency $\eta_m = C_h/R_y$	47.6%	47.8%	47.7%	48.0%	48.0%	48.0%	48.0%
Power absorbed P_a, Watts	288	330	292	652	624	665	846
Power delivered P_d, Watts	2000	2000	2000	3700	4500	4500	4500
Energy transfer efficiency $\eta_t = P_a/P_d$	14%	17%	15%	18%	14%	15%	19%

Another method of evaluating η_m is based on thermal analysis presented by Quintino et al (*Quintino et al., 2007*) which assumes that the weld area is rectangular in shape and uses the following expression for the energy to melt the material in the fusion zone

$$P_m = V * b * h * \rho * [C_p * (\Delta T) + H] \quad (5.8)$$

where V is the velocity of weld (m/sec), b is the weld width (m), h is the weld depth (m), ρ is the density (Kg/m^3), C_p is the specific heat (J/kg-K), ΔT is the temperature rise from ambient condition to the melt point, and H is the melting latent heat (or enthalpy of melting). Since using the areas of the fusion zones will be more accurate, we modified this equation as:

$$P_m = V * A * \rho * [C_p * (\Delta T) + H] \quad (5.9)$$

In equation (9), A = area of the weld (mm^2). Since the constants C_p varies with temperature, an average value of 0.67 J/Kg-K at 700 was used for C_p and values of 7850 Kg/m^3 for ρ and 274.052 kJ/kg for H were used to compute P_m. Dividing P_m by power delivered indicates one way of indicating melting efficiencies. We call this η_{m1}. On the other hand, since Fuerschbach defines melting efficiency as the amount of power required to melt divided by the amount of power absorbed, we calculated the melting efficiency using P_m from equation (9) and P_a from Table 5.5 as calculated using equation (4). We called this η_{m2}. Both η_{m1} and η_{m2} along with other calculations are shown in Table 5.6.

Table 5.6 Melting efficiencies using method of Quintino et al

Characteristic	TR-0/MS-70	TR-0/DP-70	DP/MS-70	DP/MS-150	U/MS	U/TR	U/DP
Area of the weld, mm^2	0.89	1.03	0.90	0.95	0.91	0.97	1.23
Weld speed mm/sec	70	70	70	150	150	150	150
Power required to melt, P_m	1021.7	1176.6	1036.0	2332.0	2233.6	2378.7	3025.7
Power delivered P_d, Watts	2000	2000	2000	3700	4500	4500	4500
Melting efficiency $\eta_{m1} = P_m/Pd$	51.1%	58.8%	51.8%	63.0%	49.6%	52.9%	67.2%
Power absorbed Pa, Watts	1138	1306	1153	2577	2469	2629	3344
Melting efficiency $\eta_{m2} = P_m/P_a$	89.8%	90.1%	89.9%	90.5%	90.5%	90.5%	90.5%

It can be seen that the values of η_{m1} from Table 5.6 are comparable to energy transfer efficiency η_t from Table 5.5. This suggests that power absorbed calculated using equation (4) gives results very similar to the power

required to melt the material, calculated using equation (9). Values obtained for η_{m2} using Fuerschbach's definition of melting efficiency seem to be overly optimistic, since they are in the 80% to 90% range, suggesting that the proper method to compute melting efficiency is by using the power absorbed or power required to melt the material.

A third method of determining η_m used sometimes in literature is to describe it as the melt volume per unit of laser energy input or mm^3/kJ:

$$\text{Efficiency, } \eta_{m3} = (\text{Weld cross-sectional area}) * (\text{Travel speed})/\text{Power} \qquad (5.10)$$

Where weld cross-sectional area is in mm^2, travel speed in mm/sec and power is in kW. η_{m3} can be correlated to η_m (absolute value) as (*Kim et al., 2008*):

$$\eta_m = 1.1 * \eta_{m1} \qquad (5.11)$$

Melt efficiency for various combinations using this method are shown in Table 5.7, and seem to be considerably lower than the values obtained for the first two methods. Since Quintino's method of calculating the melt efficiency using the power required to melt the material is the most logical procedure, it can be concluded that this method does not result in accurate values.

Table 5.7 Melting efficiencies using the third method

Characteristic	TR-0/MS-70	TR-0/DP-70	DP/MS-70	DP/MS-150	U/MS	U/TR	U/DP
Area of the weld, mm^2	0.89	1.03	0.90	0.95	0.91	0.97	1.23
Weld speed mm/sec	70	70	70	150	150	150	150
Power kW	2	2	2	3.7	4.5	4.5	4.5
Melting efficiency η_{m3} = Area*Speed/Power	31.2%	35.9%	31.6%	38.4%	30.3%	32.2%	41.0%
True melting efficiency $\eta_m = 1.1 * \eta_{m3}$	34.3%	39.5%	34.7%	42.3%	33.3%	35.5%	45.1%

5.5 Conclusions

Experimental work and analysis of laser welding of advanced high strength steels was performed. The following conclusions can be drawn form the results and discussion.

1. Yb:YAG laser produces excellent welds without any defects such as porosity, undercut, burn through and humping.
2. Very high microhardness values were noted in some fusion zones.
3. Softening in the heat affected zone was observed in DP980.
4. Weld speeds calculated using a simple moving line source model based on a cylindrical channel surrounded by an elliptical melt pool yielded very good results. The calculations and micrographs suggest that the speeds used for the experiments should be slightly modified to be closer to the calculated values of the speeds.
5. Melting efficiencies were calculated using two methods and seemed to be in the 50 to 70% range.

Acknowledgements

The authors wish to thank Ford Motor Company in general for their support of this project. In particular, Matt Zaluzec, James Boileau, Ron Cooper, John Bonnen, Brian Sullivan and Shirleen Holland are thanked for their invaluable help and support. Thanks are due to Arcelor Mittal for providing the TRIP and DP materials, and for providing valuable data used in the calculations, to Severstal Inc for providing USIBOR and mild steel material, and to Trumpf Inc in getting the samples welded.

References

Anderson, S.G., 2007. Diverse markets buoy laser business. Laser Focus World 43 (1) http://www.optoiq.com/index/photonics-technologies-applications/lfw-display/lfw-article-display/282681/articles/laser-focus-world/volume-43/issue-1/columns/the-editors-desk/diverse-markets-buoy-laser-business.html

David, S.A., Babu, S.S., Vitek, J.M., 2003. Welding: Solidification and Microstructure. The Minerals, Metals & Materials Society (TMS), http://www.tms.org/pubs/journals/JOM/0306/David-0306.html

Dowden, J.M., Davis, M., Kapadia, P., 1985. The flow of heat and the motion of the weld pool in penetration welding with a laser. J. Appl. Phys., 57, 4474-4479.

Fuerschbach, P.W., 1996. Measurement and prediction of energy transfer efficiency in laser beam welding. Welding Journal, 75, 24-s to 34-s.

Havrilla, D., 2005. Disk lasers: YAG is redefined through the diode-pumped disk laser. Laser Focus World, Article 234082, 401 (8) http://www.optoiq.com/index/photonics-technologies-applications/lfw-display/lfw-article-display/234082/articles/laser-focus-world/volume-41/issue-8/features/disk-lasers-yag-is-redefined-through-the-diode-pumped-disk-laser.html

Huntington, C. A., Eagar, T. W., 1982. Laser welding of aluminum and aluminum alloys. Welding Journal 62 (4), 105s.

Kaplan, A., 1994. A model of deep penetration laser welding based on calculation of the keyhole profile. Journal of Physics D: Applied Physics, 27 (9)

Kawahito, Y., Terajima, T., Kimura, H., Kuroda, T., Nakata, K., Katayama, S., and A. Inoue, A., 2008. High-power fiber laser welding and its application to metallic glass. Materials Science and Engineering B, 148

Kim J. -K, Lim, H. –S, Cho, J.-H., Kim C.-H., 2008. Bead-on-plate weldability of Al 5052 alloy using a disk laser. Journal of Achievements in Materials and Manufacturing Engineering, 28 (2), 187-190. http://www.journalamme.org/papers_vol28_2/28212.pdf

Lankalapalli, K., Tu, J., Gartner, M., 1996. A model for estimating penetration depth of laser welding processes. Journal of Physics D: Applied Physics, 29, 1831.

Mallen, R.Z., Tarr, S., Dykeman, J., 2008. Recent Applications of High Strength Steels in North American Honda Production. http://www.autosteel.org/AM/Template.cfm?Section=Great_Designs_in_Steel_2008_Presentations&CONTENTID=24032&TEMPLATE=/CM/ContentDisplay.cfm

Quintino, L., Costa, A., Miranda R., Yapp, D., Kumar, V., C.J. Kong, C.J, 2007. Welding with high power fiber lasers - preliminary study. Materials and Design, 28, 1231-1237

Ream, S.L., 2005. Disc and fiber gain ground. Laser Focus World, Article 221991, 20 (2) http://www.optoiq.com/index/lasers-for-manufacturing/display/ils-article-display/221991/articles/industrial-laser-solutions/volume-20/issue-2/features/disc-and-fiber-gain-ground.html

Schuocker, D., 1999. High Power Lasers in Production Engineering. Imperial College Press.

Sharma, R. S., and Molian, P., 2009. Yb:YAG laser welding of TRIP780 steel with dual phase and mild steels for use in tailor welded blanks. Materials and Design, 30, (10), 4146-4155.

Sharma, R., Molian, P., Peters, F., 2010. Geometric variability and surface finish of weld zones in Yb:YAG laser welded advanced high strength steels. Journal of Manufacturing Processes, 12 (2), 73-84.

Steen, W., Dowden, J., Davis, M., Kapadia, P., 1988. A point and line source model of laser keyhole welding. J. Phys. D: Appl. Phys., 21, 1255-1260

Swift-Hook, D., Gick, A., 1973. Penetration welding with lasers. Welding Journal, 52, 492

Xia M., Sreenivasan, N., Lawson S., Zhou Y., Tian Z., 2007. A comparative study of formability of diode laser welds in DP980 and HSLA steels. ASME Journal of Engineering Materials and Technology, 129, 446-452.

Zhao, H., White, D.R., DebRoy, T., 1999. Current issues and problems in laser welding of automotive aluminium alloys. International Materials reviews, 44, 6, 238-266.

CHAPTER 6. FORMABILITY OF LASER WELDED ADVANCED HIGH STRENGTH STEELS

A modified version of this work with additional authors will be published in a research journal

Rajashekhar S Sharma and Pal Molian

Abstract

Formability of TRIP780 welded to mild steel using a 1030 nm, 6 kW Yb:YAG disk laser, was studied using Ohio State University (OSU) plane strain test method. Optical and scanning electron microscope studies of the fusion and heat affected zones, including results of color tint etching using sodium metabisulphite, were also presented. In addition, microhardness and tensile test data are also included. Microstructural analysis revealed that the fusion zone mostly consisted of martensite. Formability test results indicate that the weld joints of TRIP780 steels laser welded to mild steel are robust to fractures during plane strain tests, with the fracture occurring in the mild steel region and running parallel to the weld zone. Fracture of the locking beads during the tests prevented further testing of the joints of DP980 steels laser welded to mild steel and to TRIP780. The high microhardness values obtained in the DP980/MS as well as DP980/TRIP780 joints suggest that the laser welded zones in these combinations also would not fracture during OSU plane strain testing. It is concluded that the locking beads for the OSU test procedure must be modified substantially to accommodate high strength/low ductility materials such as DP980.

6.1 Introduction

There is considerable interest among automobile manufacturers to use tailor welded blanks (TWB) of advanced high strength steels (AHSS). TWB refers to blanks of different materials, coatings or thicknesses first welded and then processed using metal forming and other processes. Use of TWB's will result in weight and cost savings, increased passenger safety and improved fuel economy. Laser welding is the most suitable method to prepare TWB's, since they result in smaller fusion zones (FZ) and heat affected zones (HAZ) when compared to traditional welding processes such as resistance mash seam welding. Due to the inherent high rates of cooling, laser welding can also result in higher hardness values in FZ and HAZ, although in the case of very high strength materials such as DP980 and Martensitic steels, the outer edges of the heat affected zone will have lowered microhardness values [1, 2].

Several formability studies of laser welded regions are reported in literature, although not much work has been carried out on the formability of laser welded AHSS steels. Xia et al [3] have studied formability of DP980

steel welded to DP980 and high strength low alloy (HSLA) steel welded to HSLA, using Diode laser beam; they used limiting dome height (LDH) tests. Nagasaka [4] has presented investigation of the effects of laser welding conditions on mechanical properties and press formability, and concluded that lower weld speed and energy input during laser welding results in better formability. Xia, et al [5] carried out similar LDH tests on DP and HSLA steels and concluded that the failure pattern of DP parent metal was determined by its rolling direction. Sreenivasan et al [6] used LDH tests to evaluate DP980 steel compared to formability of base metal. In all these studies, regions of lowered hardness in the heat affected zones of DP980 seemed to have the largest impact on the formability. Padmanabhan et al [7] studied the effect of anisotropy in the laser-welded blank and blank rolling direction and concluded that appropriate combination of the blank sheets rolling direction orientation can significantly improve the formability of the TWB in the deep-drawing of square cup. Hyrcza-Michalska and Grosman [8] present research on laser welded blanks made of different steel grades and different combinations of thicknesses using hydroforming as well as bulging tests. Ahmetoglu et al [9] carried out deep drawing of welded blanks of aluminum killed draw quality (AKDQ) steel with weld line located at different orientations; they concluded that by adjusting the blank holder pressure (BHP), the weld line orientation can be controlled and thus it is possible to reduce the level of straining on the side of the blank that has lower thickness or lower strength. Saunders and Wagoner [10] have used LDH tests with finite element modeling using SHEET-3 software, and concluded that weld line motion during forming operations is critically important to the development of strain patters and failure sites. They also observe that when samples are stretched parallel to the weld, the limited weld ductility allows cracks to nucleate and propagate normal to the weld line; and when the samples are stretched perpendicular to the weld, the stronger material constrains the weaker one to fail near plane-strain tension with the crack in the weaker material running parallel to the crack. Several research investigators [11, 12, 13] have studied the characteristics of weld line movements for deep drawing in TWB's, while others [14, 15, 16, 17] have presented other aspects of forming of TWB's including springback [14] and Forming Limit Diagram in TWB's including DP800 material [16].

In this paper, a study of the formability of TRIP steel butt-welded to mild steel using a 6 kW Yb:YAG laser is reported. Results of attempts to conduct formability tests on DP steel welded to MS and to TRIP780 are also presented. The objective is to confirm that fractures do not occur in the weld regions in the TWB's. For the purpose of these experiments, the direction of the rolling during the manufacturing of steel was ignored. Since the unilateral plane-strain OSU formability test (OSUFT) has been found to result in the lowest variability [17], this method was chosen. Microhardness values as well as microstructural analysis using color tint etching [18, 19] and scanning electron microscope are also included, since the hardness and microstructures have a significant impact on formability.

6.2 Experimental details

Two grades of AHSS (TRIP780 and DP980) and mild steel (MS) were obtained in the form of 1 mm (MS, TRIP) and1.5 mm (DP) sheets, and sheared to coupons of about 100mm x 200 mm size. TRIP780 had been pre-coated with zinc coating by galvanizing process. Some TRIP steel coupons were pre-strained to 5% (designated TR-5) and 10% (designated TR-10) in an Instron machine. The grades, compositions and mechanical properties of these steels are listed in Table 6.1 (a) and (b). The coupons were milled on the edges to keep the straightness within 10% of thickness to allow butt welding. The coupons were later mounted in a fixture as shown in Figure 6.1 with the configuration set as a butt joint and welding was carried out. A continuous wave Yb:YAG laser, manufactured by TRUMPF (TruDisk 6002) with a power capacity of 6 kW and beam quality of 8 mm-mrad was used for welding. The laser beam was transmitted through optical fiber and focused on the specimen surface by the lens with 200 mm focal length. The spot diameter at the focal point was about 0.6 mm. The system comprises of the laser beam delivery system mounted on the robot's end-effector and moving in 3D space, with the beam perpendicular to the workpieces for all combinations. The samples were held stationary in the weld fixture as shown in Figure 6.1. Initially bead-on-plate experiments were performed to obtain the appropriate laser parameters for butt welding. Two power levels (and speeds suitable for full penetration as determined by bead-on-plate experiments) were used as shown in Table 6.2. Argon gas at 30 l/min was used for shielding. The weld scheme is presented in Table 6.2, also shows samples tested for tensile strength as well as samples prepared for formability tests.

Table 6.1 (a) Chemical composition (wt%) of DP980, TRIP780 and mild stel used.

Steel	C	Mn	Mo	P	S	Si	Cr	Al	B	Ti	V	Nb	Ni	Cu	N
DP980	0.135	2.100	0.350	--	--	0.050	0.150	0.450	0.007	--	--	--	--	--	--
TRIP780	0.190	1.580	--	0.013	0.025	1.600	0.070	0.036	--	0.027	--	0.038	0.020	0.020	
Mild Steel	0.043	0.270	0.002	0.041	0.009	0.021	0.020	0.040	0.000	0.002	0.001	--	--	--	0.007

Table 6.1 (b) Mechanical properties of DP980, TRIP780 and mild steel used.

Steel	Yield strength (MPa)	Ultimate strength (MPa)	Elongation (%)
DP980 CR	534	980	12.2
TRIP780 CR	471	792	18
Mild Steel	215	355	37.8

After welding, dog-bone shaped tensile test specimens were cut from transverse sections at the mid-length position of the welds and the cut surfaces were prepared for metallographic inspection by polishing and etching using a 3% nital solution to display weld shape and microstructure. The mounted samples were examined under optical microscope. Microhardness was evaluated using a Vicker's hardness tester at a load of 0.5 kN. Tensile tests on the welded joints were carried out on an Instron Tester. Dimensions of the tensile samples are shown in Figure 6.2.

Table 6.2 Experimental set-up for laser welds

Sample ID	Material 1	Thickness (mm)	Material 2	Thickness (mm)	Weld power (kW)	Weld speed (mm/sec)
TR-0/MS-70	TR-0 (TRIP780 as received, cold rolled and galvanized using GI process)	1.0	MS (Mild Steel, cold rolled, no protection)	1.0	2.0	70
TR-5/MS-70	TR-5 (TRIP780 5% stretched, cold rolled and galvanized)	1.0	MS (Mild Steel, cold rolled, no protection)	1.0	2.0	70
TR-10/MS-70	TR-5 (TRIP780 10% stretched, cold rolled and galvanized)	1.0	MS (Mild Steel, cold rolled, no protection)	1.0	2.0	70
TR-0/DP-70	TR-0 (TRIP780 as received, cold rolled & galvanized)	1.0	DP980 cold rolled, no protection	1.5	2.0	70
DP/MS-70	DP980 cold rolled, no protection	1.0	MS (Mild Steel, cold rolled, no protection)	1.0	2.0	70
TR-0/MS-150	TR-0 (TRIP780 as received, cold rolled and galvanized)	1.5	MS (Mild Steel, cold rolled, no protection)	1.0	3.7	150
DP/MS-150	DP980 cold rolled, no protection	1.5	MS (Mild Steel, cold rolled, no protection)	1.0	3.7	150

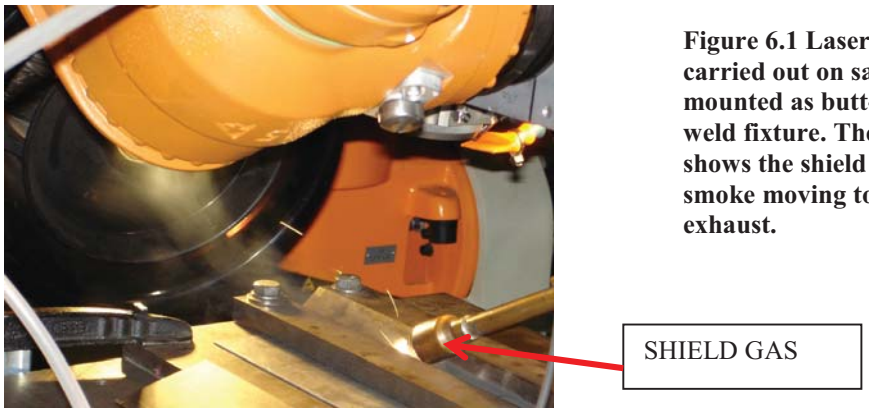

Figure 6.1 Laser welding being carried out on samples mounted as butt-joints in the weld fixture. The photograph shows the shield gas along with smoke moving towards the exhaust.

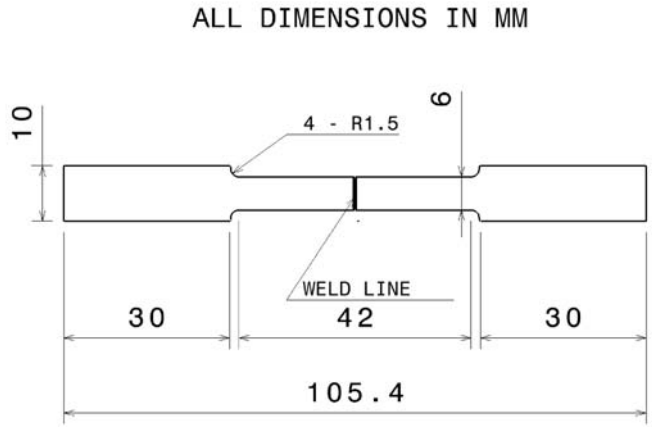

Figure 6.2 Dimensions of tensile test sample.

Formability tests were carried out using OSU formability test on an Instron Tester using special OSU fixtures (Figure 6.3). To accomplish this, welded samples as well as samples of plane stainless steel grade 409 were cut to size and milled to a uniform 192mm width. The test equipment was switched on for over an hour to stabilize actuation before the tests were run. Initially, about 20 samples of stainless steel 409 were prepared and run on the machine for conditioning of the punch and binder plates to minimize variability [17]. After this, welded samples were positioned with the weld bead in the plane strain area, with the weld zone as shown in Figure 6.3 (b), with loads applied in the transverse direction in relation to the weld line. Clamping loads typical of 333.6 kN were applied for the locking beads. No lubrication was applied to the samples during the test. The punch was advanced at 5 mm/sec. The dimensions for the OSU fixture are shown in Figure 6.4.

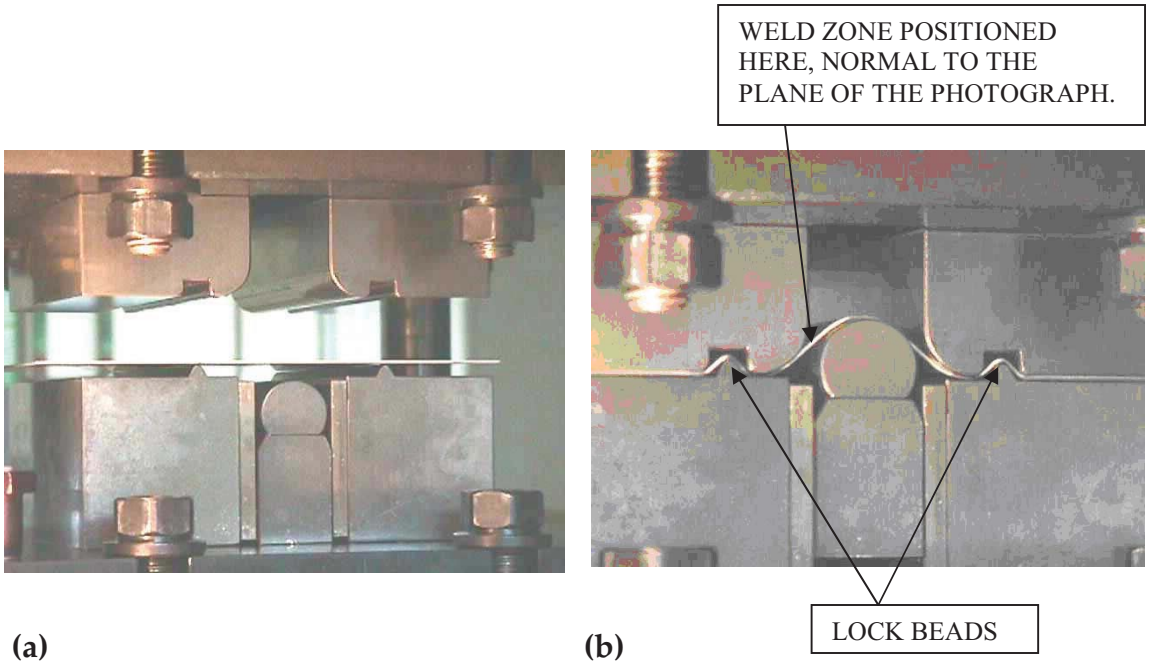

Figure 6.3 OSU formability test fixture set-up: (a) Before the start of the test (b) At the conclusion of tests when the samples are completely formed.

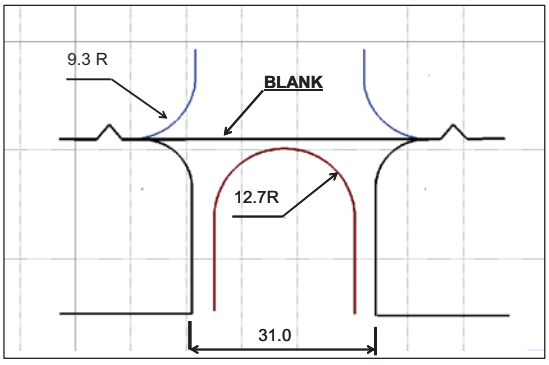

Figure 6.4 Major dimensions in the OSU test fixture.

6.3 Results and discussion

6.3.1 Microstructure

Optical micrographs of three combinations, TR-0/MS-70, TR-0/DP-70 and DP/MS-150, after being treated with 2% Nital are presented in Figure 6.5 (a) – (d). The weld zones in (a) – (c) show the typical hour-glass shape with a slight tear-drop at the bottom. The dendritic structure in the micrographs seem nearly horizontal in the bottom while at 15 to 45 degrees to the horizontal in the mid to upper regions. In a few areas of DP/MS and TRIP/MS combinations, microstructures as shown in Figure 6.5 (d) were noted. Comparison of this with the micrographs presented by Gallagher et al [1] suggests that these areas might be secondary widmanstatten ferrite with relatively lower microhardness values.

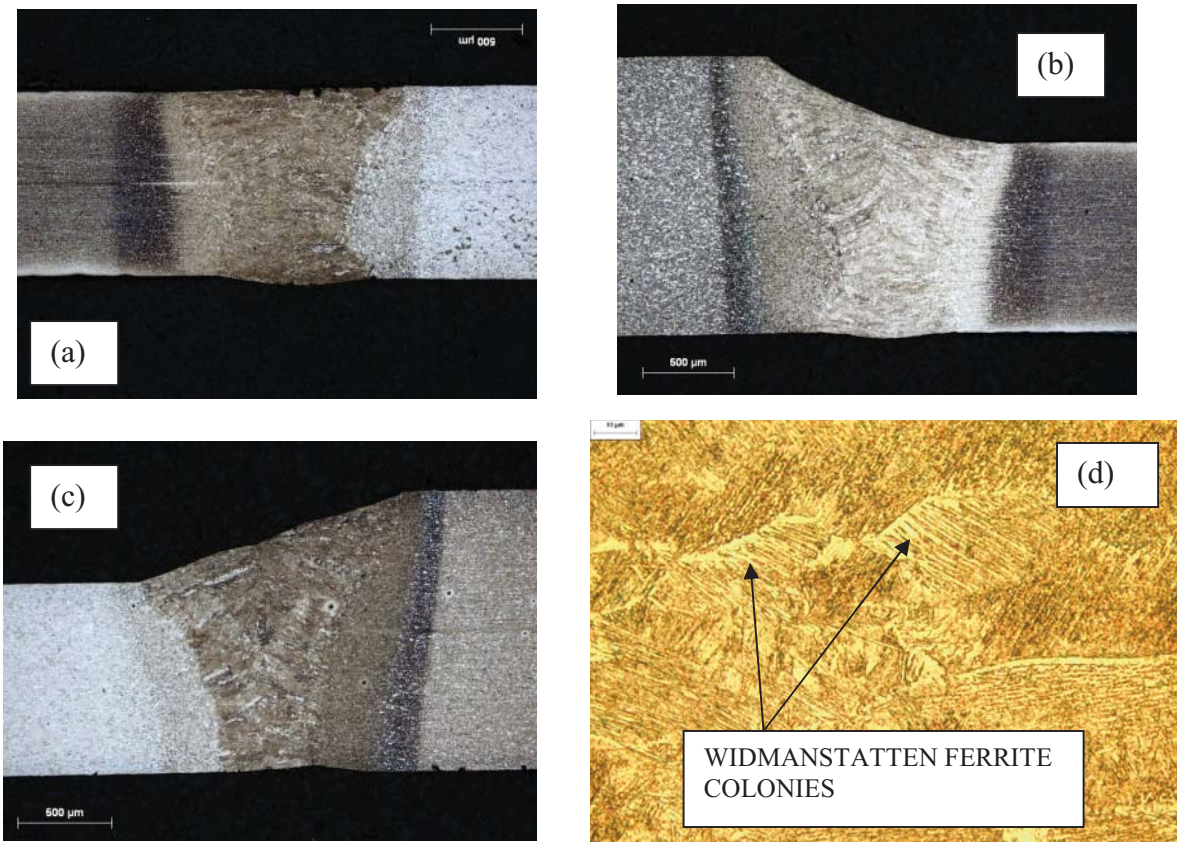

Figure 6.5 Weld zones for three combinations: (a) TR-0/MS-70, with TRIP780 shown on the left, (b) TR-0/DP-70 with DP shown on the left, and (c) DP/MS-150 with MS shown on the left. All micrographs are shown at 50X magnification. Colonies of Widmanstatten ferrite found in TR-0/MS-150 combination are shown in (d), which is captured at 1000X magnification.

Micrographs of TR/MS-70, TR/DP-70 and DP/MS-150 after treating the polished surfaces to 2% Nital followed by 2% Sodium Metabisulphite (NaMBiS) are shown in Figure 6.6. Since martensite is shown in dark

brown color after NaMBiS treatment [18], it can be said that most of the fusion zones in all three cases and parts of heat affected zones in DP980 and TRIP780 are martensitic. Presence of other microstructures cannot be ruled out since NaMBiS etches bainite also to a dark color. Regions of white are also seen, and since NaMBiS shows ferrite in white, the earlier observation about the presence of secondary Widmanstatten ferrite seems to be correct. Some regions of TR/MS-70 and DP/TR-70 are shown with varying darkness, but this is because of variation in the etching of the surfaces. In the case of Figure 6.6 (c) showing microstructure of DP/MS-150, some zones look lighter in color because of variation in the etching process. Higher magnification micrographs are presented in Figure 6.7 for the fusion zones, transition zones from FZ to HAZ, as well as from transition zones HAZ to base metal for TR/MS-70, TR/DP-70 and DP/MS-150 combinations.

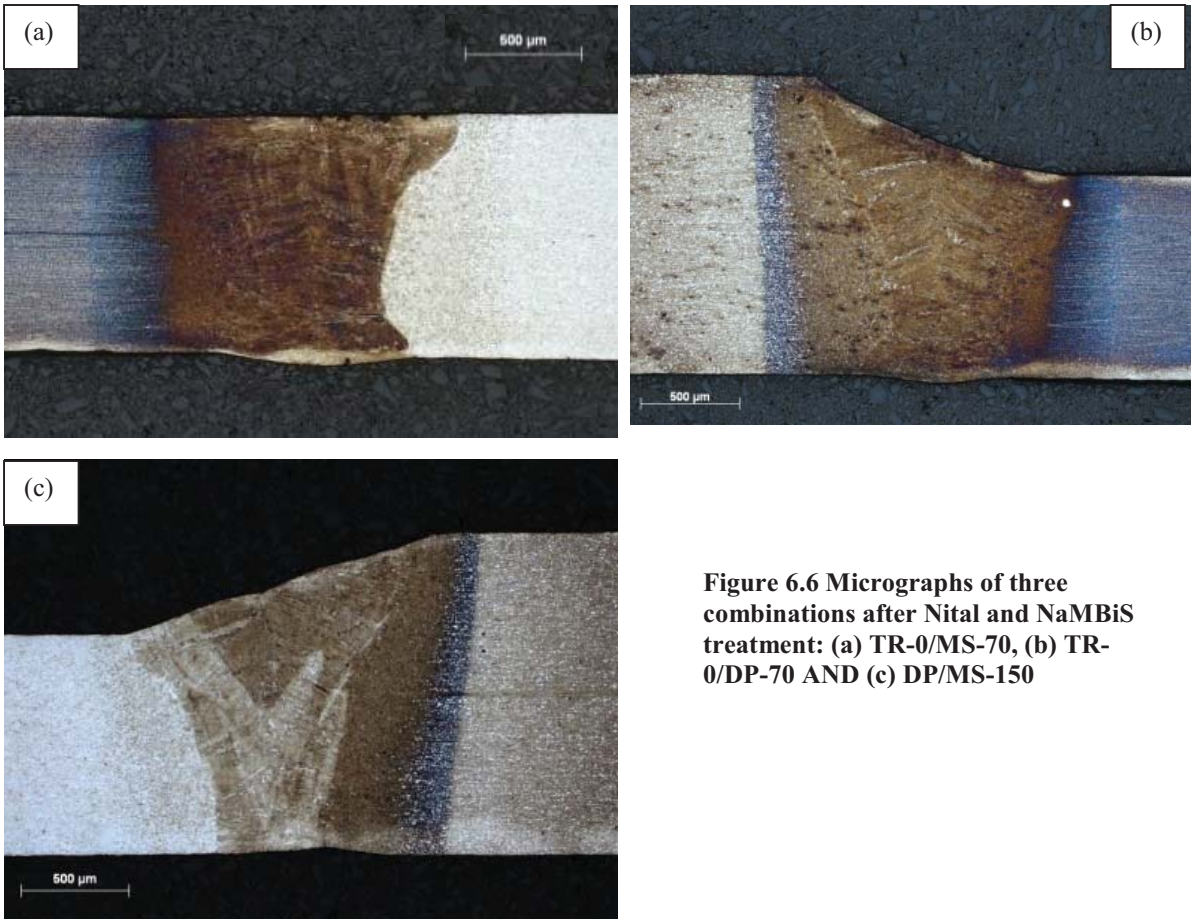

Figure 6.6 Micrographs of three combinations after Nital and NaMBiS treatment: (a) TR-0/MS-70, (b) TR-0/DP-70 AND (c) DP/MS-150

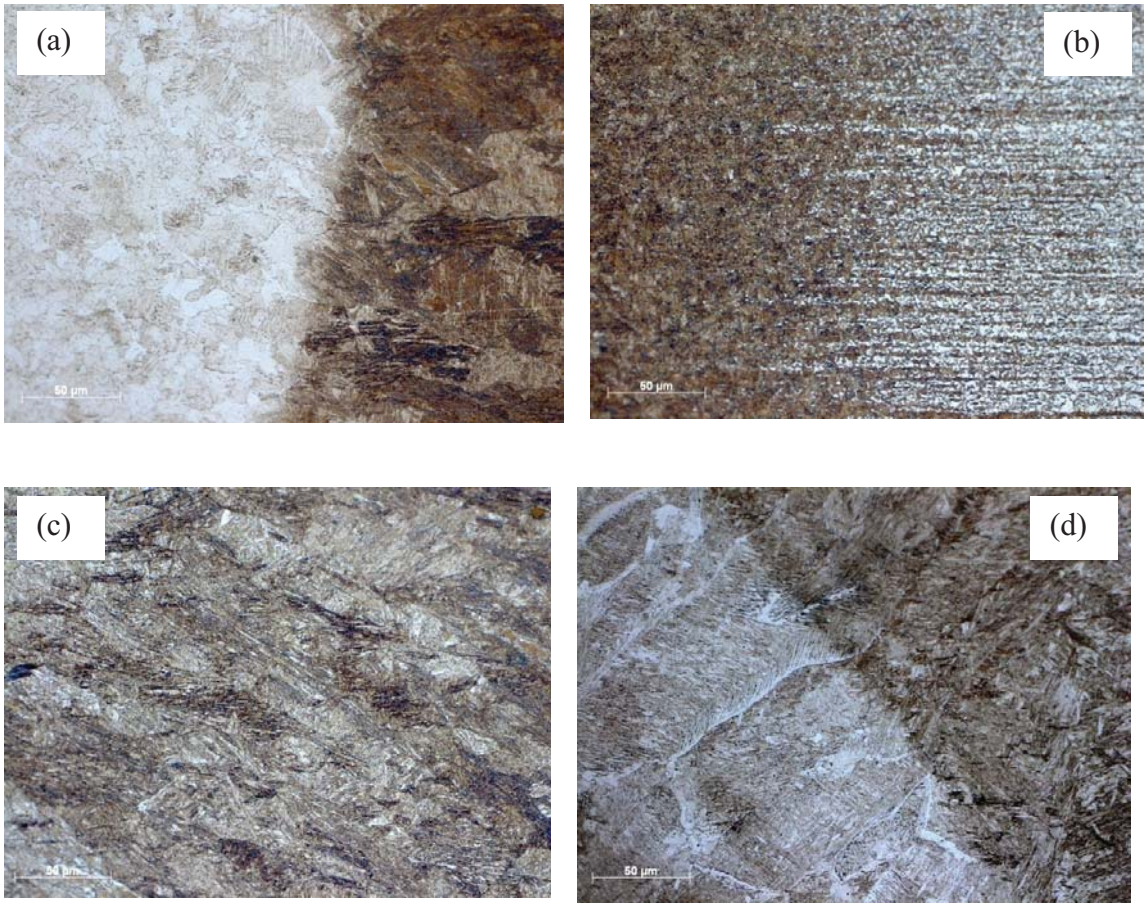

Figure 6.7 Higher magnification micrographs (all at 300X) with NaMBiS treatment in the weld zones for the three combinations: (a) HAZ TO fusion zone transition for mild steel in TR-0/MS-70, (b) HAZ to base metal in TRIP780 in TR-0/MS-70 (c) Fusion zone in TR-0/DP-70, (d) Fusion zone in DP/MS-150, and, (e) Fusion zone to HAZ in DP980 in DP/MS-150

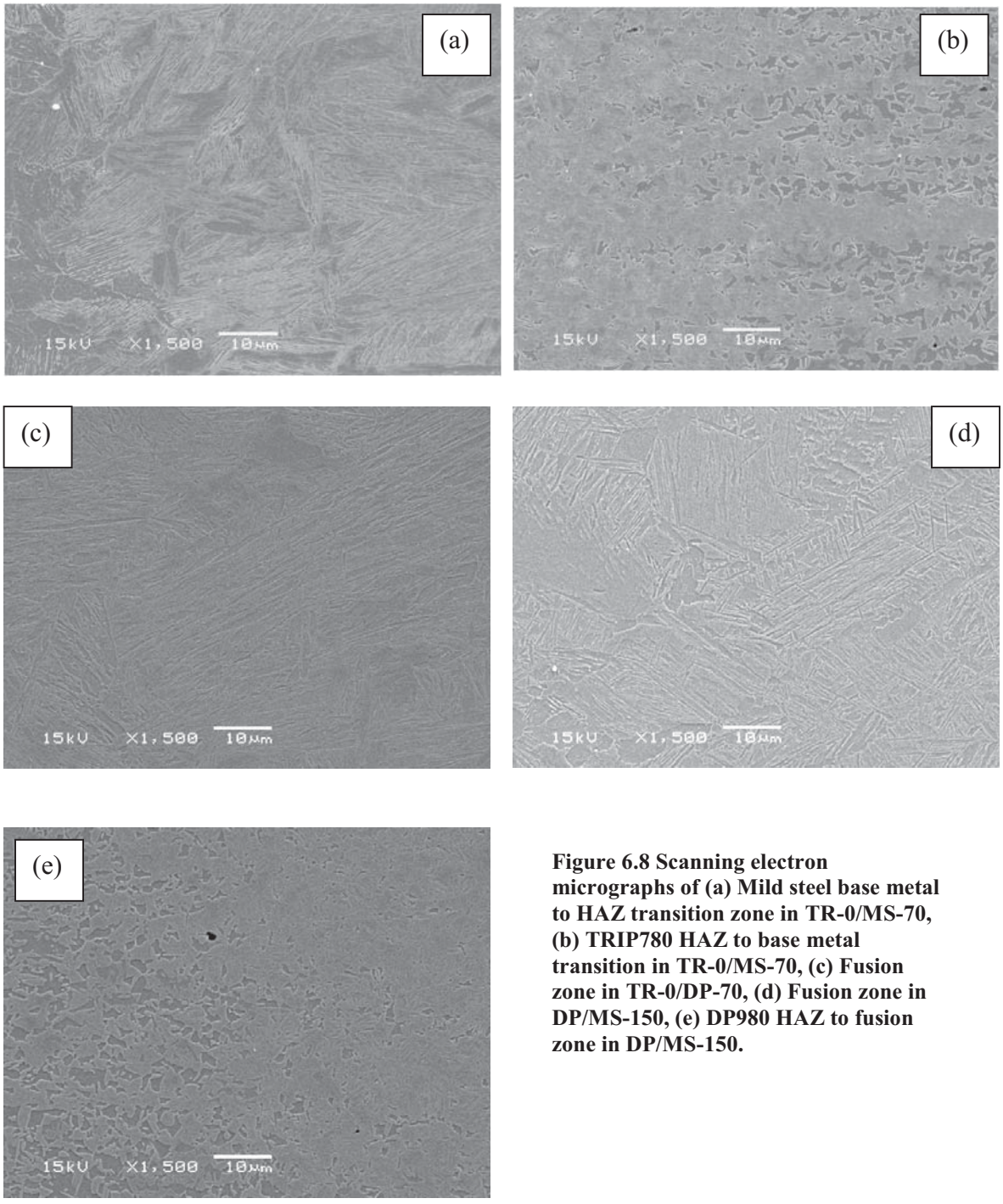

Figure 6.8 Scanning electron micrographs of (a) Mild steel base metal to HAZ transition zone in TR-0/MS-70, (b) TRIP780 HAZ to base metal transition in TR-0/MS-70, (c) Fusion zone in TR-0/DP-70, (d) Fusion zone in DP/MS-150, (e) DP980 HAZ to fusion zone in DP/MS-150.

Scanning electron micrographs of the fusion and transition zones for TR/MS-70, TR/DP-70 and DP/MS-150 are shown in Figure 6.8. All micrographs are taken at a 1500X magnification. Comparison of the SEM micrographs in the fusion zones, to the results presented by Cortez et al [20], indicates presence of both upper

and lower bainite although the microstructure seems to be mostly martensitic in nature. This agrees with the earlier statement about the presence of bainite found with color tint etching. The recrystallized grains near the HAZ for both TRIP780 and DP980 appear to be less refined compared to the base metal.

These findings about the microstructure in the fusion zone being mostly martensitic agrees with the findings of Rizzi et al [21] who conducted experiments on laser welding of TRIP, DP and martensitic steels and found the microstructure to be mostly martensitic. Since the fusion zone is rich in alloying elements, the carbon equivalent in DP steel is calculated as 0.59 wt% and 0.47 wt% in TRIP780 using the carbon equivalency calculator [22]. Together with the high rate of cooling of 2000°K/Sec [23], it can be expected that the microstructure would be nearly all martensite.

6.3.2 Microhardness

Microhardness values for the fusion and heat affected zones for TRIP/MS, DP/MS and TRIP/DP combinations were evaluated using microhardness tester. The results for TRIP/MS, TRIP/DP and DP/MS combinations have been reported in the literature [2, 24] and are shown in Figure 6.9.

Microhardness values for DP980 are lower in the outer edges of the heat affected zone, while the microhardness values of mild steel seem to be higher in the heat affected zones. However, the microhardness values of DP980 and TRIP780 as well as the fusion zones for all combinations are higher than the microhardness values for mild steel. This is an important observation since microhardness values are directly correlated to strength and is a good predictor on where the fracture can occur both in tensile tests and in plane-strain formability tests.

The variation of microhardness values in the fusion zone is attributed to the presence of secondary widmanstatten ferrite and upper and lower bainite structures.

6.3.3 Tensile Tests

The results of tensile tests are also reported earlier [2, 24] and summarized in Fig. 6.10. All joints with mild steel (TR/MS and DP/MS) fractured in the mild steel region while the TR/DP samples all fractured in the TRIP780 region. For joints with mild steel, there is very little difference in the tensile test results. For example, the graphs for DP/MS-150, TR-0/MS-70 and TR-10/MS-70 can be seen to be identical. There is, however, considerable difference in the maximum strain values before fracture between the graphs for TR-0/DP-70 and TR-10/DP-70 with TR-0/DP showing significantly higher values of strain. The maximum stress values for

these two, however, seems to be nearly the same. This suggests that the energy absorbed, and therefore the toughness, of TR-10/DP is considerably lower than that for TR-0/DP.

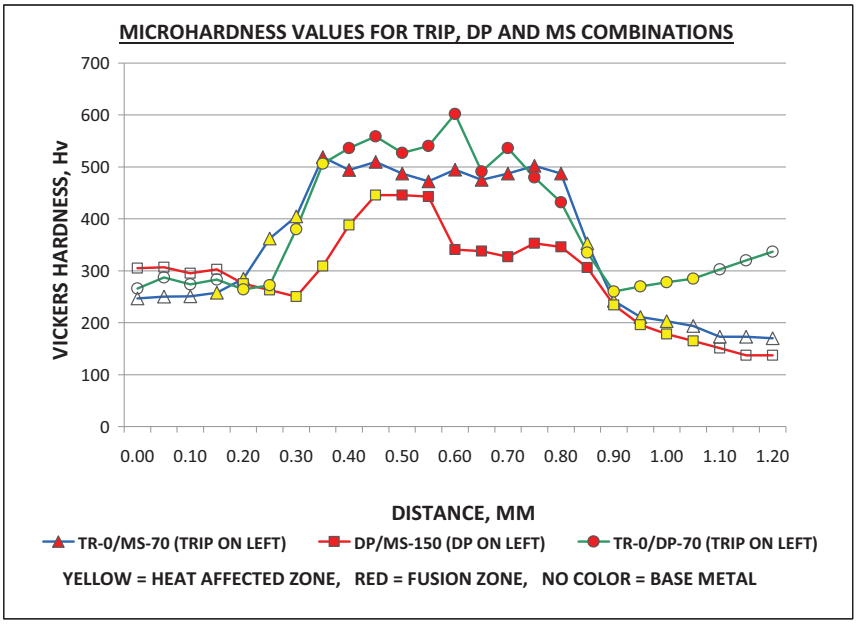

Figure 6.9 Microhardness values for three combinations, TR-0/MS-70, DP/MS-150 and TR-0/MS-150. The microhardness values for TR-5/MS-150 and TR-10/MS-150 are similar to TR-0/MS-70 and are not shown.

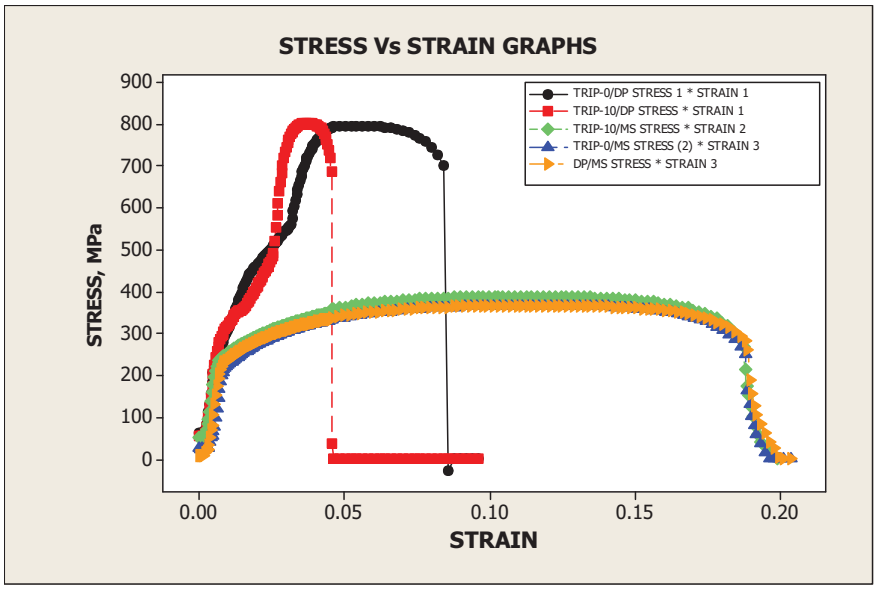

Figure 6.10 Tensile test results for TR-0/MS-70, TR-0/DP-70 and DP/MS-150 [Reference 24]

6.3.4 Formability Tests using OSUFT

Formability tests were run on multiple samples of TR-0/MS-70, TR-5/MS-70 and TR-0/MS-150 joints. Due to shortage, only one sample of TR-10/MS-70 was run. All the samples fractured in the mild steel region with the fracture running parallel to the weld. This agrees with the conclusion of Saunders and Wagoner [10] that when plane strain tests are run perpendicular to the weld line, the stronger material constrains the weaker one and the fracture occurs parallel to the weld line. Typical fracture exhibited by these sample combinations are shown in Figure 6.11 (a).

When the first sample of DP/MS-70 using OSU procedure was tested, it was observed that the test stopped due to fracture of DP material in the lock bead. A second sample resulted in the same condition. In order to understand the issues, several DP base material samples were run, some by softening the radii around the lock bead region by doubling up the samples. All but one of these samples fractured at the radius. One of the samples fractured at the locking bead is shown in Figure 6.11 (b) and the sample that survived the test is shown in Figure 6.11 (c). After these failures, simple bend tests were run on DP material and based on those, the lock bead design was changed to a friendlier design as shown in Figure 6.12 (a) – (b), where (a) shows the design before the major changes and (b) shows the design of the beads after the changes. However, even with these changes, the fracture of DP980 in the lock beads could not be prevented and therefore further tests of TR/DP-70, DP/MS-70 and DP/MS-150 were suspended.

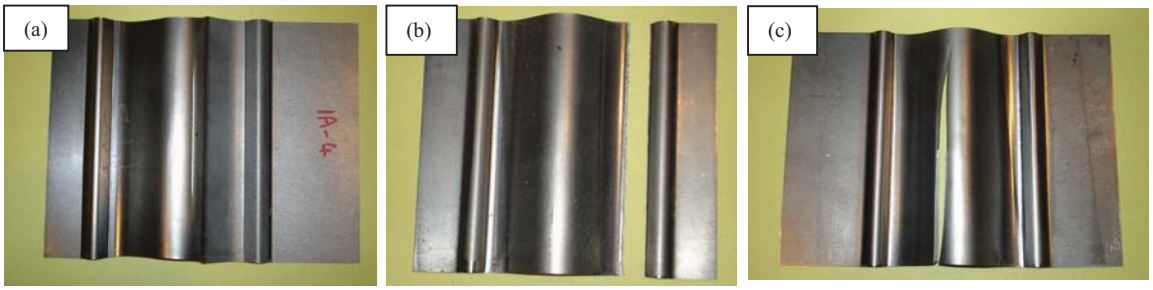

Figure 6.11 Fractured samples from the OSU formability test: (a) A typical TR-0/MS-70 sample with fracture above the weld line (b) Fracture of DP material in the lock bead before the test could be concluded (c) A DP980 base material sample that went through the test without fracture in the lock bead, indicating that reducing the stress in the lock bead would allow tests to be successfully concluded.

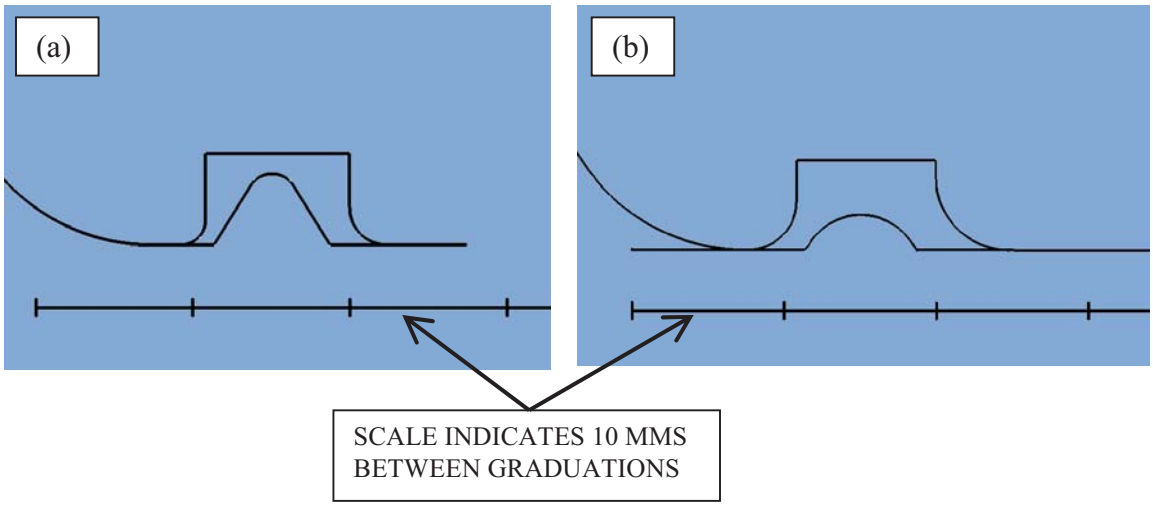

Figure 6.12 Lock bead design (a) before modifications, and, (b) after modifications. A scale is provided to indicate dimensions.

Since the microhardness values of the DP980 in the base material and in HAZ are higher than the base material hardness in TRIP780 and MS in TR/DP and DP/MS combinations, it can be expected that fractures would occur in the base metal region of TRIP780 in TR/DP combinations and MS region of DP/MS combinations. Previous studies [25] have indicated that coatings such as galvanized zinc would result in considerable dimensional variability as well as higher surface roughness on the top of the weld zones. For this reason, this theory would be valid if there are no severe concavity issues or weld defects in the fusion zones, as these would be detrimental to the strength of the joint.

The results of the formability tests for TR/MS joints are summarized in Table 6.3 and show the maximum load and stroke experienced by the punch during the tests. Since only the two TR-0/MS joints have sample sizes of more than 3, both average and standard deviation values are shown for them. Average values are shown for TR-5/MS-70, while standard deviation values are not shown for TR-5/MS-70 as well as TR-10/MS-70.

The graphs of punch load versus punch displacement are shown for the above combinations in Figure 6.13. To reduce the clutter, only the extreme values are shown for TR/MS-70 and TR/MS-150. The graph also includes results of formability tests on DP/MS-70 before fracture in the lock bead region; since the lock bead area fractures first, the data shown for DP/MS-70 should not be considered reliable. The TR/MS combinations seem to be very close to each other with fairly small spread, although the two graphs of TR-5/MS-70 seem to vary considerably from each other. Also, as can be seen, DP/MS-70 shows larger values of load as well as displacement. This indicates that the DP material took most of the load during the test before fracturing in the lock bead area.

Table 6.3 Summary of formability test results

Joint	Maximum load, kN			Maximum stroke, mm		
	Individual values	Average	Standard Deviation	Individual values	Average	Standard Deviation
TR-0/MS-70	63.80	63.79	1.50	13.44	13.38	0.28
	62.23			12.95		
	62.47			13.31		
	64.62			13.49		
	65.83			13.72		
TR-0/MS-150	62.01	64.68	1.78	12.85	13.24	0.33
	65.52			13.44		
	65.49			13.08		
	65.68			13.59		
TR-5/MS-70	66.20	63.72	N/A	12.19	12.51	N/A
	61.24			12.83		
TR-10/MS-70	62.41	N/A	N/A	12.95	N/A	N/A

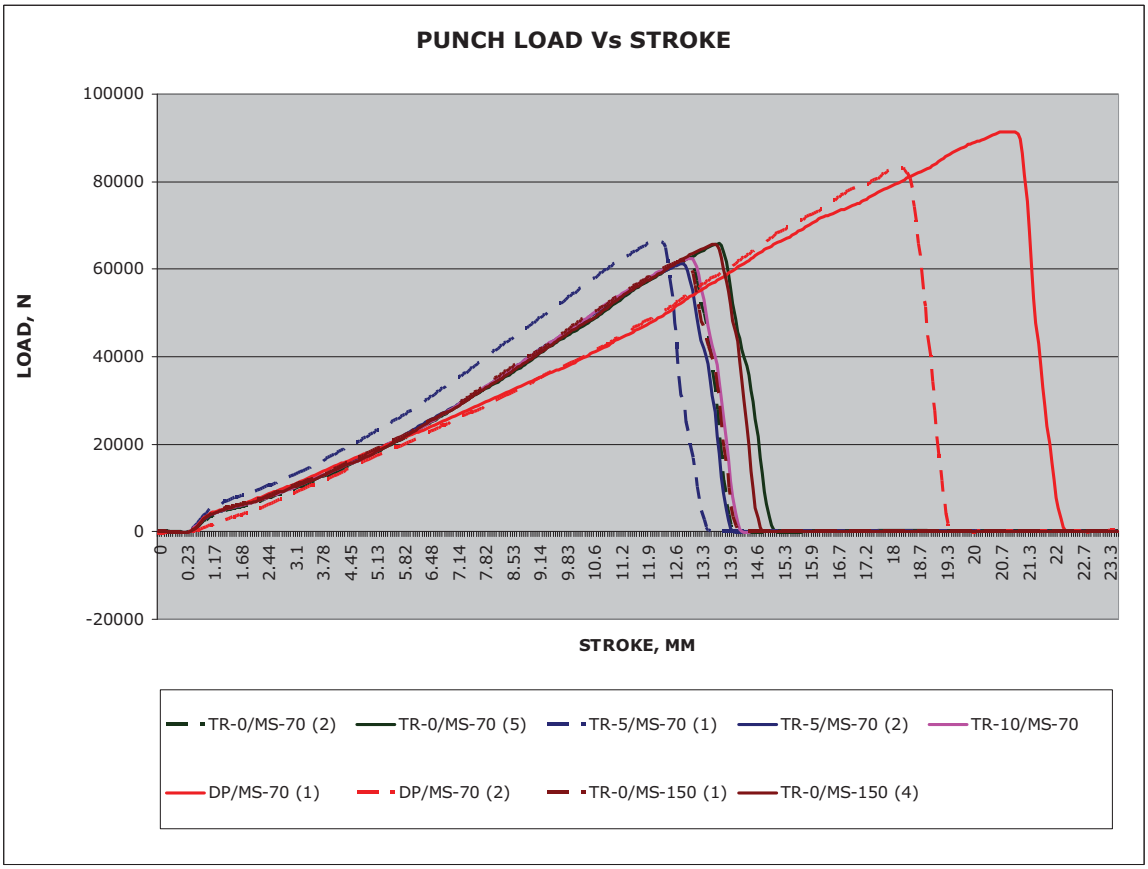

Figure 6.13 Punch load versus stroke for the combinations tested. For TR-0/MS-70 and TR-0/MS-150, only the extreme lines are shown.

Finally, a 2-sample t-test was run to determine if there is a difference in the average values of maximum loads supported by TR-0/MS-70 versus TR-0/MS-150. Since the weld region is small, and, since in both cases the microhardness values are significantly higher than the hardness in the base mild steel region, there is no reason why the two should be different. This theory proves correct, since the t-test suggests that the null hypothesis, that, the mean values for the maximum loads supported by TR-0/MS-70 and TR-0/MS-150 combinations are equal, cannot be rejected since the P-value is 0.464. The estimate for the difference between the mean values is 0.88 kN, and the 95% confidence interval for this difference is (-3.75, 1.98). Tests were run on Minitab® 15 and the results are shown in Table 6.4.

Table 6.4 Two-sample t-test for TR/MS-70 vs TR/MS-150

	N	Mean	StDev	SE Mean
TR/MS-70	5	63.79	1.5	0.67
TR/MS-150	4	64.68	1.78	0.89

Null hypothesis: μ (TR/MS-70) - μ (TR/MS-150) = 0

Alt. hypothesis: μ (TR/MS-70) - μ (TR/MS-150) $\neq$ 0

Estimate for difference: -0.88

95% CI for difference: (-3.75, 1.98)

T-test of difference = 0 (vs not =): T-Value = -0.79 P-Value = 0.464

6.4 Conclusions

Detailed microstructural characterization of tailor welded blanks of advanced high strength steels followed by results of microhardness, tensile and plane-strain formability tests have been presented. OSU formability test was used to conduct plane strain tests with the loads being perpendicular to the weld line. Color tint etching method, as well as scanning electron microscopy, were used to characterize the microstructures. Following are the conclusions that can be drawn:

1. The microstructure in the fusion zones and parts of heat affected zones for TR/MS, TR/DP and DP/MS combinations seem to consist of primarily martensite. However, presence of other microstructures such as lower and upper bainite and widmanstatten ferrite were also detected.
2. Microhardness values were in the 450-600 Hv range, further substantiating the presence of martensite in both fusion and heat affected zones.

3. No fractures occurred in the fusion or heat affected zones during the tensile and formability tests, suggesting that the high microhardness values in these regions adequately compensated for concavity, dimensional variability and surface roughness on the top of the weld.
4. The mild steel region in the TR/MS joints fractured during the formability tests with the fracture running parallel to the weld line. This agrees with the conclusion arrived at by Saunders and Wagoner [10] that the weaker material in TWB's will fracture with the fracture line being parallel to the weld line, when loads are applied perpendicular to the weld line during plane strain formability tests.
5. OSU formability test fixture needs to be modified to prevent fracture of high strength, low ductility materials such as DP980 in the lock bead region.
6. Weld speed and power does not affect the results obtained during formability tests.

Acknowledgements

The authors wish to thank Ford Motor Company in general for their support of this project. In particular, Matt Zaluzec, James Boileau, Ron Cooper, John Bonnen, Brian Sullivan and Shirleen Holland are thanked for their invaluable help and support. Help of Robert Comstock and his management at AK steel in running the formability tests and of Naveen Ramisetti and Min Kuo in helping with identification of microstructures using sodium metabisulphite is gratefully acknowledged. Thanks are due to ArcelorMittal for providing the TRIP and DP materials and to Severstal Inc. for providing mild steel material. Finally, the invaluable help of Juergen Stollhof, David Havrilla and Hans Leidich of Trumpf Inc. in getting the samples welded is thankfully acknowledged.

References

[1] Gallagher M, Yan B, Nadkarni G, Polon M, Aefferer H, Leidich H. Laser Assembly Welding of Advanced High Strength Steels. Advanced Laser Applications Conference and Exposition 2005; 3; 49-62

[2] Sharma, R.S. and Molian, P. Yb:YAG laser welding of TRIP780 steel with dual phase and mild steels for use in tailor welded blanks. Materials and Design 30 (2009) 4146-4155.

[3] Xia M, Sreenivasan N, Lawson S, Zhou Y, Tian Z. A comparative Study of Formability of Diode Laser Welds in DP980 and HSLA Steels. ASME Transactions July 2009; 129; 446-452

[4] Nagasaka, A. Press formability of YAG laser welded TRIP steel sheets. ACTA Metallurgica Sinica (English Letters), Vol. 15, No. 1, pp 21-25, February 2002.

[5] Xia, M.S., Kuntz, M.L., Tian, Z.L., Zhou, Y. Failure study on laser welds of dual phase steel in formability testing. Science and Technology of Welding and Joining, pp 378-387, Vol 13, No 4, 2008.

[6] Sreenivasan, N., Xia, M., Lawson, S., Zhou, Y. Effect of laser welding on formability of DP980 steel. Journal of Engineering Materials and Technology, Vol 130, 2008.

[7] Padmanabhan, R., Baptista, A.J., Oliveira, M.C., Menezes, L.F. Effect of anisotropy on the deep-drawing of mild steel and dual-phase steel tailor-welded blanks. Journal of Materials Processing Technology, 184 (2007) 288-293.

[8] Hyrcza-Michalska, M, Grosman, F. The research of laser welded blanks characteristics in basic and technological drawability tests. Metal Forming, Vol.1, 2008, pp 780-787.

[9] Ahmetoglu, M.A., Brouwers, D., Shulkin, L., Taupin, L., Kinzel, G.L., Altan, T. Deep drawing of round cups from tailor-welded blanks. Journal of Material Processing Technology, 53 (1995) 684-694.

[10] Saunders, F.I., Wagoner, R.H. The use of tailor-welded blanks in automotive applications. Simulation of Materials Processing, Balkema, Rotterdam, 1995, pp 157-164.

[11] Choi, Y., Heo, Y., Kim, H.Y., Seo, D. Investigations of weld-line movements for the deep drawing process for tail welded blanks. Journal of Materials Processing Technology, Vol 108, Issue 1, 2000, pp 1-7.

[12] Tang, B.T., Zhao, Z., Yu, S., Chen, J., Ruan, X.Y. One-step FEM based control of weld line movement for tailor-welded blanks forming. Journal of Materials Processing Technology, Vol 187-188, pp 383-386, 2007.

[13] Panda, S.K., Kumar, D.R. Study of formability of tailor-welded blanks in plane-strain stretch forming. The International Journal of Advanced Manufacturing Technology, Vol 44, Numbers 7-8, 2008.

[14] Padmanabhan, R., Oliveira, M.C., Laurent, H., Alves, J.L., Menezes, L.F. Study of springback in deep drawn tailor welded blanks. International Journal of Material Forming, Volume 2, Supplement 1, 829-832, 2009

[15] Reis, A., Texeira, P., Duarte, J.F., Santos, A., Barata da Rocha, A., Fernandes, A.A. Tailor welded blanks – an experimental and numerical study in sheet metal forming on the effect of welding. Computers and Structures 82 (2004) 1435-1442.

[16] Sheng, Z.Q. Formability of tailor-welded strips and progressive forming test. Journal of Materials Processing Technology, Volume 205, 2008, pp 81-88.

[17] Karthik, V., Comstock Jr., R.J., Hershberger, D.L., Wagoner, R.H. Variability of sheet formability and formability testing. Journal of Materials Processing Technology, Vol 121, pp 350-362, 2002.

[18] Girault, E., Jacques, P., Harlet, Ph., Mols, K., Van Humbeeck, J., Aernoudt, E., Delannay, F. Metallographic methods for revealing the multiphase microstructure of TRIP assisted steels. Materials Characterization, Vol 40, pp 111-118, 1998.

[19] De, A.K., Speer, J.G., Matlock, D.K. Color tint-etching for multiphase steels. Advanced Materials & Processes, pp 27 – 30, 2003.

[20] Cortez, V.H.L, Medina, G.Y.P., Valdez, F.A.R., Lopez, H.F. Effects of the heat input in the mechanical integrity of the welding joints welded by GMAW and LBW process in Transformation Induced Plasticity steel used in the automotive industry. Soldag. insp. (Impr.) vol.15 no.3 São Paulo July/Sept. 2010. http://dx.doi.org/10.1590/S0104-92242010000300010

[21] Rizzi P, Bellingeri S, Massimino F, Baldissin D, Battezzati L. Microstructures in laser welded high strength steels. The 13th international conference on rapidly quenched and metastable materials, vol. 144; 2009. p. 1–4.

[22] http://www.chapelsteel.com/carbon-equivalency.html

[23] Grigorevich, Aleksandr. Basics of laser material processing. CRC Press, 1994.

[24] Sharma, R.S., Molian, P. Weldability of advanced high strength steels using an Yb:YAG disk laser. Journal of Materials Processing Technology 211 (2011) 1888-1897.

[25] Sharma, R., Molian, P., Peters, F. Geometric variability and surface finish of weld zones in Yb:YAG laser welded advanced high strength steels. Journal of Manufacturing Processes 12 (2010) 73-84.

CHAPTER 7. GENERAL CONCLUSIONS AND FUTURE WORK

Application of laser welding to tailor-welded blanks consisting of advanced high strength steels has a bright future in the automotive industry. Although use of AHSS materials and laser welding process is predominantly used in Europe, automobile manufacturers in USA are beginning to realize their advantages and are moving towards use them in higher abundance. This work indicates that AHSS materials can be joined among themselves and to mild steel successfully resulting in high quality welds. Microstructural analyses, microhardness tests, tensile and fatigue tests amply support this conclusion. While coatings such as aluminum and zinc do affect factors such as concavity, surface finish and hardness, laser welding seems to overcome these shortcomings in several cases. Some of the significant conclusions are:

1. The fusion zones are generally free of defects such as cracks, porosity, voids and inclusions, and exhibit microhardness values as high as 600 Hv. Some softening in high strength materials such as DP980 materials are noted, and it can be expected that when DP980 is welded to DP980, fractures would occur in these regions. However, when DP980 is joined to lower strength materials such as TRIP780 and mild steel, the weaker substrate such as TRIP780 or mild steel would fracture.

2. There is evidence suggesting that the hardness of the fusion zone closer to the top of the surface is higher than the hardness in the lower regions, since the rate of cooling in the upper regions would be enhanced due to blowing of the shield gas.

3. Factors affecting the surface roughness and weld concavity are coatings and thickness differentials between the samples being joined using laser welding. Thickness differential has been shown to result in higher variability in weld concavity, which could become an important consideration in cases where hardness (and therefore strength) of the joint is lower than that of the substrate materials being joined. Thickness differential by itself may not contribute to higher surface roughness, but in combinations with other coatings, it has been shown to result in higher surface roughness. Since surface roughness has an impact on the fatigue strength of the joint, these factors need to be considered carefully.

4. Weld speeds calculated using a simple moving line source model based on a cylindrical channel surrounded by an elliptical melt pool provided very good results. Calculated melting efficiencies seemed to be in the 50 to 70% range.

5. TRIP780 steels laser welded to mild steel were tested successfully using Ohio State University plane strain formability test with fracture occurring in the mild steel region away from the weld. Since the

microhardness values of the weld zone and heat-affected zones would be higher than that in mild steel, the fracture ran parallel to the weld line; this agrees with the observations of other researchers.

Since this area is still relatively new, many recommendations for future work based on the research presented in this work can be offered and are summarized below.

1. Effects of laser welding of other AHSS materials: Although considerable investigative research work has been carried out in laser welding of AHSS materials, not all AHSS materials have been researched for the effect of laser welding on tensile strength, fatigue and dynamic impact tests which will simulate crash performance. With the arrival of new steels such as TWIP steels, even more research needs to be carried out to further improve passenger safety, fuel economy and other factors for the customers.

2. Predictive models for laser welding process: Although a significant amount of work has been carried out in modeling heat transfer characteristics for laser welding [1, 2], there is considerable room for improving the predictive models for size of the fusion zone, rate of cooling, and other important considerations. Further, using better models, the hardness, dendritic structure, residual stresses, microstructure and the strength of the joint can be predicted, which will prove to be highly useful in industry.

3. Use of finite element analysis to prove the applications in automobiles for tensile strength, formability, fatigue and crash events: Currently, FEA is a critical tool used extensively in automotive industry. These tools need to be developed further for predicting performance when AHSS materials are laser welded and used in automobiles either as laser welded blanks or as separate components joined together.

4. Differential cooling when using USIBOR as part of TWB: When USIBOR is used as a tailor welded blank joined to other materials like mild steel, DP980 and TRIP780, use of hot forming process will negatively affect the properties of these other materials. A well designed differential cooling process will keep USIBOR's properties of very high strength and the ductility, high elongation and other properties of the other materials in tact. This will save considerable cost during processing while delivering high performance.

5. Auto-correlation and cross-correlation values for the surface roughness can be determined for various cases involving different coatings and material thicknesses. Using these values, the weld cross sections can be simulated using fast fourier transforms (FFT) and Monte Carlo methods. These

simulations can then be used to statistically determine if the samples can survive tensile and fatigue tests when the hardness values in the weld region would be comparable or significantly lower than the hardness of materials that are being joined.

6. Methods to prevent softening in HAZ, concavity and other issues: While welding certain very high strength steels such as DP980, the hardness drops in the outer regions of the heat affected zones. When joining DP980 to DP980, such hardness drops occur in both HAZ regions. Additionally, severe weld concavity can reduce the strength of the joints also. These may not present a problem if the product can be designed around the properties of such joints, but the product can be further enhanced by coming up with new methods to prevent such problems.

7. An important and interesting finding reported in Appendix B is that TRIP steels exhibit higher tensile strengths in the transverse direction when compared to rolling direction. The toughness of TRIP780, DP980 and mild steels were all, however, higher in the rolling direction when compared to transverse directions. More research needs to be carried out to reveal the underlying phenomena behind these findings.

References

[1] Rai, R. Modeling of heat transfer and fluid flow in keyhole mode welding. PhD Thesis, Pennsylvania State University, UMI Number 3346365, 2009.

[2] Dahotre, N.B., Harimkar, S.P. Laser fabrication and machining of materials. Springer Science and Business Media, 2008.

APPENDIX A. EFFECTS OF SURFACE COATINGS AND THICKNESS DIFFERENTIALS OF MATERIALS BEING JOINED ON SURFACE ROUGHNESS

A.1 Introduction

During the investigation of geometric variability (Chapter 4), it was surmised that two factors affect the roughness and waviness of the top surface of the laser welds: (a) Presence or absence of coatings, and, (b) Difference in thicknesses of materials being joined. The presence of coatings such as aluminum (USIBOR) or zinc through galvanized iron process (TRIP780) would tend to increase both the roughness and waviness of the top surface. This is because during the welding process, the coatings would melt and get blown by the shield gas and get redeposited on the top of the weld. A larger difference in the thicknesses of materials being joined might not have an effect on surface roughness and waviness values but a confirmation of this using a systematic experimentation would be useful.

A full factorial design of experiments (DOE) was carried out to find out the effect of these two factors (coatings and thickness differentials) on the surface roughness and waviness values.

A.2 Materials and Methods

A 2-factor DOE was set-up with thickness differential (three levels) and coating (two levels: with and without) as the two factors, and is shown in Table 1. The three levels of thickness differentials were 0.0 mm, 0.3 mm and 0.8 mm. The combinations are designated R1C1 (Row 1, Column 1) through R2C3 (Row 2, Column 3). Row 1 show sample combinations with coating while Row 2 show sample combinations without any coating. Similarly, columns 1 through 3 show thickness differentials between materials being welded with values of 0, 0.3 and 0.8 mm respectively. USIBOR samples were 1.8 mm thick and had aluminum coating, TRIP780 was 1 mm thick and had zinc coating and DP980 (1.5 mm thick) and mild steel, MS (1 mm thick) had no coatings. For R1C2 combination, USIBOR was ground on the bottom using a surface grinder with magnetic table to achieve a 1.5 mm thick material; however, this could not be ground further since doing so would move the sample (and damage it) during the grinding operation. For this reason, TRIP780 material with zinc coating was used for the R1C3 combination. For samples without coating (Row 2), 1.8 mm and 1 mm thick mild steel samples as well as 1.5 mm thick DP980 material were used. Since one of the samples (1.5 mm thick USIBOR) was ground on the bottom and another sample (TRIP780) had zinc coating instead of aluminum coating, these can be considered as noise factors.

The edges on the sample combinations were prepared by using an EDM operation. After this, they were mounted on the weld fixtures and were all welded using 3.8 kW power at 70 mm/sec speed. The top of the

weld regions of weld samples were analyzed using the UBM roughness analyzer. 3 scans were recorded in the middle of the welded region on the top of the weld in the direction of the weld. The scan lines were each 40 mm long and were spaced at 0.13 mm. The three scans for each combination were used as three replicates. Response data was collected for surface roughness values (R_a) and waviness (W_t) and analyzed.

Table A.1 Set-up of Design of Experiments

		Thickness differential		
		0 mm	0.3 mm	0.8 mm
Surface	Coating	1.8 mm USIBOR welded to 1.8 mm USIBOR (R1C1)	1.8 mm USIBOR welded to 1.5 mm USIBOR (R1C2)	1.8 mm USIBOR welded to 1.0 mm TRIP (R1C3)
	No coating	1.8 mm MS welded to 1.8 mm MS (R2C1)	1.8 mm MS welded to 1.5 mm DP980 (R2C2)	1.8 mm MS welded to 1.0 mm MS (R2C3)

A.3 Results and Discussion

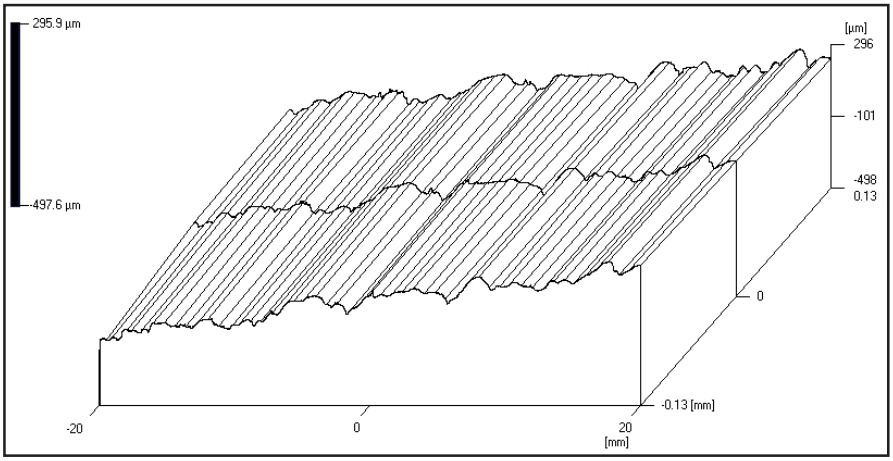

Figure A.1 Surface roughness profile for R1C1 combination (3 lines, each 40 mm long, spaced at 0.13 mm, measured on the top of the weld in the weld direction).

An example plot of surface roughness obtained for R1C1 combination is shown in Fig A.1. The three scans shown are at 0.13 mm apart and are 40 mm long. Each of the horizontal line scans were analyzed for roughness and waviness using DIN 4776 filter. The three scan values were considered as three replicates of the same experiment and are summarized in Tables A.2. The main effects and interaction plots are shown in Figures A.2 (a) - (b).

An examination of Figure A.2 indicates that both the roughness and waviness values of the surface on the top of the welds will be significantly higher when samples with coatings are welded compared to when samples without coating are welded. Also, with increasing thickness differentials, the roughness values have a tendency decrease for samples with coatings while increasing for samples without coating. Interestingly, the waviness values have a tendency to fall with increasing thickness differential. Also, the interaction plots suggest that there is a strong interaction between the two factors, coating and thickness differential, for both roughness and waviness.

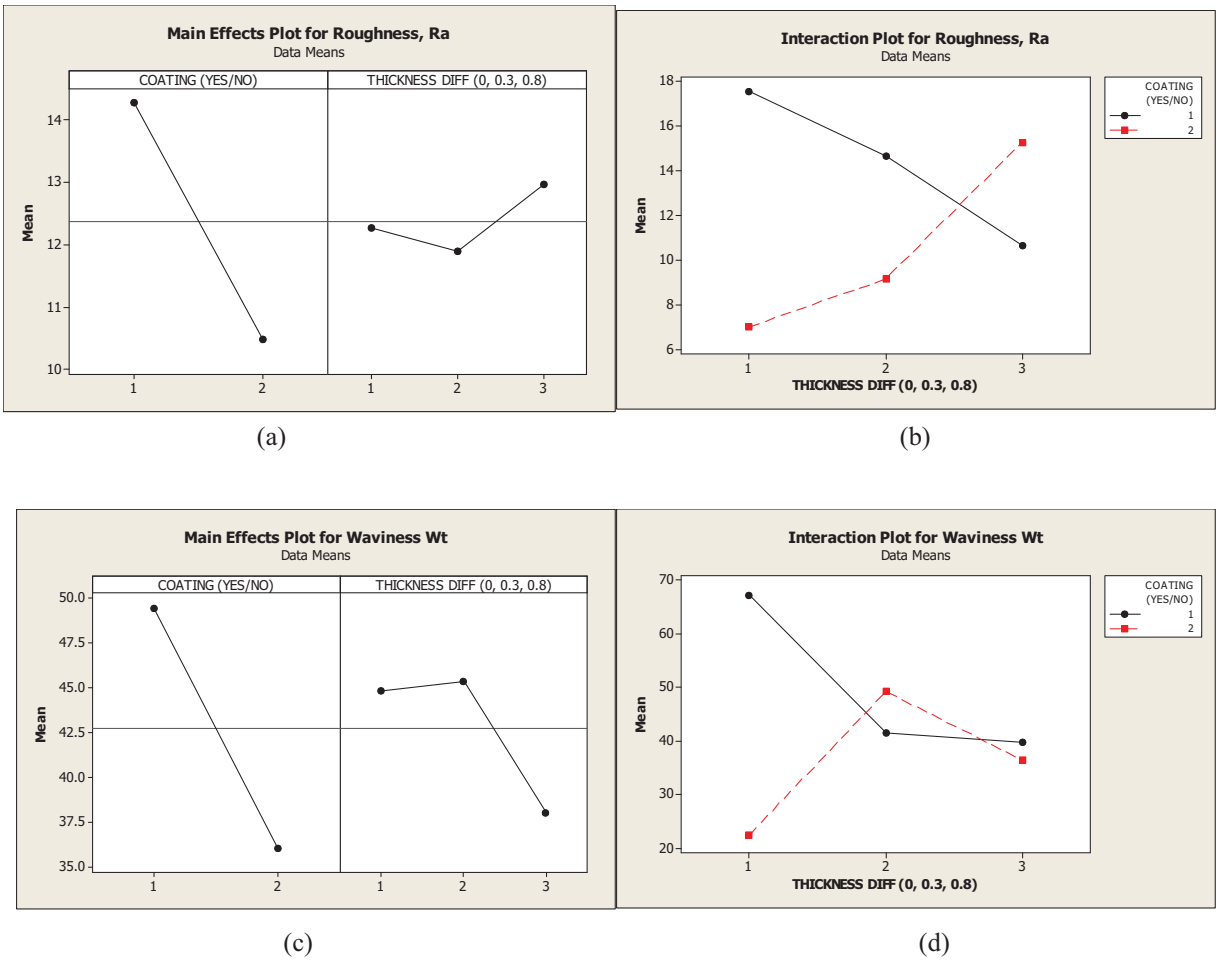

Figure A.2 Main effects and interactions plots for Roughness [(a) and (b)] and Waviness [(c) and (d)]

The data for both roughness and waviness were analyzed using Minitab® version 15 (Paul Mathews, "Design of Experiments with Minitab", Quality Press, 2005). As mentioned earlier, the three line-scan values for each combination shown in Table 1.3 were used as three replicates. This is because, if the average values shown Table A.2 are used for analysis considering the number of replicates as 1, the degrees of freedom (DF) for error would be zero, and the analysis of variance cannot be carried out.

Table A.2 DOE Results - Roughness and Waviness values

Replicate	Coating (Yes/No)[1]	Thickness Difference[2]	Roughness (R_a)	Waviness (W_t)
1	1	1	16.97	70.15
2	1	1	17.41	67.47
3	1	1	18.24	64.09
1	1	2	15.05	39.58
2	1	2	13.79	38.88
3	1	2	15.08	45.85
1	1	3	12.15	40.16
2	1	3	10.99	39.97
3	1	3	8.79	38.95
1	2	1	8.73	28.86
2	2	1	6.73	20.63
3	2	1	5.56	17.84
1	2	2	12.84	69.48
2	2	2	8.97	49.45
3	2	2	5.65	28.9
1	2	3	22.07	54.28
2	2	3	14.58	34.33
3	2	3	9.21	20.7

[1]Coating: Yes=1, No=2. [2]Thickness difference: 0mm=1, 0.3mm=2, 0.8mm=3

Tables A.3 (a) and (b) show the results of the analysis of variance for roughness and waviness. The F-values and the corresponding P-values indicate that, for $\alpha = 0.05$, the null hypothesis that no effect is significant can be rejected for the main effect of coating as well as the interaction effect between coating and thickness differentials. However, such a null hypothesis cannot be rejected for the main effect of thickness differential,

and for this reason, only the coating and the coating - thickness differential interaction are the only significant factors for variance.

Table A.4 (a) and (b) show similar results for the t-tests carried out for means. Analysis of the waviness data in Table 1.5 (a) indicates that coating and the interaction are both statistically significant and the null hypothesis for these can be rejected at $\alpha = 0.05$. For roughness values, the interaction for (1,2) is not statistically significant, but the null hypothesis can be rejected for (1,1), indicating that there is some evidence that the mean values for this interaction is significant but not overwhelming.

TABLE A.3 (a) Analysis of Variance for Roughness, Ra, using Adjusted SS for Tests

Source	DF	Seq SS	Adj SS	Adj MS	F	P
Coating (Yes/No)	1	64.71	64.71	64.71	6.35	0.027
Thickness Difference (0, 0.3, 0.8)	2	3.52	3.52	1.76	0.17	0.843
Coating (Yes/No)*Thickness Diff (0, 0.3, 0.8)	2	179.2	179.2	89.6	8.8	0.004
Error	12	122.2	122.2	10.18		
Total	17	369.7				

S = 3.19136 R-Sq = 66.94% R-Sq(adj) = 53.16%

TABLE A.3 (b) Analysis of Variance for Waviness Wt, using Adjusted SS for Tests

Source	DF	Seq SS	Adj SS	Adj MS	F	P
Coating (Yes/No)	1	808.4	808.4	808.4	6.43	0.026
Thickness Difference (0, 0.3, 0.8)	2	198.7	198.7	99.3	0.79	0.476
Coating (Yes/No)*Thickness Diff (0, 0.3, 0.8)	2	2309	2309	1155	9.19	0.004
Error	12	1508	1508	125.7		
Total	17	4825				

S = 11.2112 R-Sq = 68.74% R-Sq(adj) = 55.71%

Table A.4 (a) Results of t-test for roughness data

Term		Coef	SE Coef	T	P
Constant		12.3783	0.7522	16.46	0
Coating (Yes/No)					
1		1.8961	0.7522	2.52	0.027
Thickness difference					
1		-0.105	1.064	-0.1	0.923
2		-0.482	1.064	-0.45	0.659
Coating (Yes/No*Thickness Difference)					
1	1	3.371	1.064	3.17	0.008
1	2	0.847	1.064	0.8	0.441

Table A.4 (b) Results of t-test for waviness data

Term		Coef	SE Coef	T	P
Constant		42.754	2.642	16.18	0
Coating (Yes/No)					
1		6.702	2.642	2.54	0.026
Thickness difference					
1		2.086	3.737	0.56	0.587
2		2.603	3.737	0.7	0.499
Coating (Yes/No*Thickness Difference)					
1	1	15.695	3.737	4.2	0.001
1	2	-10.622	3.737	-2.84	0.015

The residual plots for roughness and waviness are shown in Figures A.3 and A.4 respectively. This includes the normal probability plots, plots of residuals against fits and the histograms. Both normal probability plot and residuals versus plot indicate that there are a few outliers, but the data looks normal without any unusual readings.

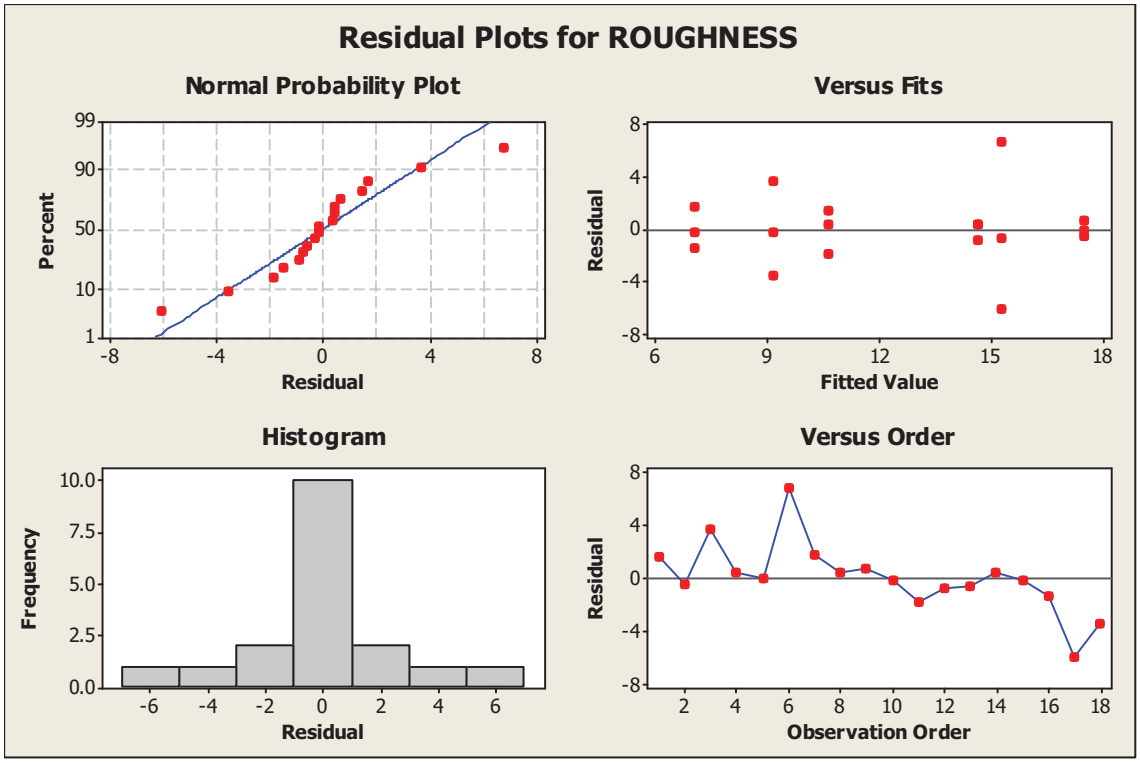

Figure A.3 Residual Plots for Roughness

Regression analysis was used to compute the coefficients in the equation:

$$\text{Roughness or Waviness} = \beta_0 + \beta_1.A + \beta_2.B + \beta_3.AB \qquad \text{(A.1)}$$

Using the values of β_x obtained from the regression analysis, the equations for roughness and waviness are written as:

$$\text{Roughness } R_a = 40.1 - 19.0*A - 11.0*B + 7.59*AB \quad \text{(A.2)}$$

$$\text{Waviness } W_t = 132 - 54.9*A - 34.5*B + 20.8*AB \quad \text{(A.3)}$$

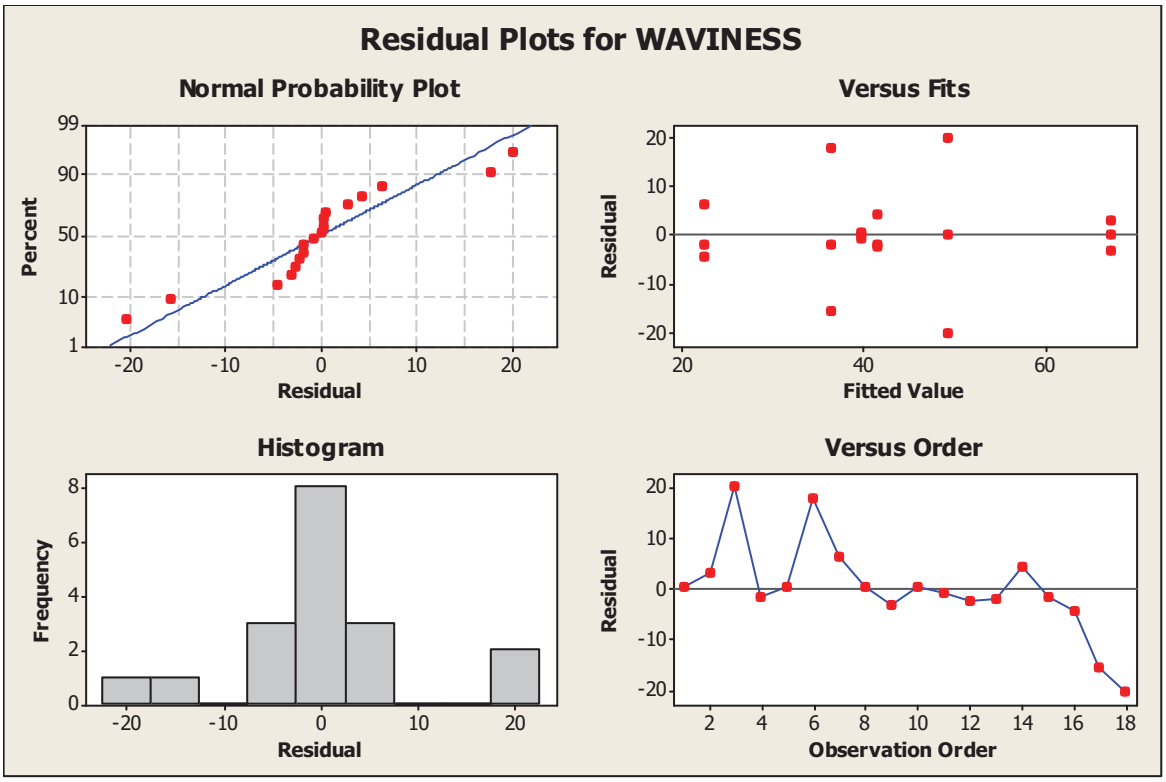

Figure A.4 Residual Plots for Waviness

In the equations (1.2) and (1.3), the term A represents coating or no coating, B represents the thickness differential and AB is the interaction term. It should be noted that the values of A and B are the coded values shown under Table 1.3, whereas the coded values for the interaction term, AB, is obtained by multiplying the coded values for A and B from the same table. These values along with the data, fitted and residual values are shown in Table 1.6.

Table A.5 Fits and residual values using regression procedure

Coating (A)	Thickness diff (B)	Interaction (AB)	Roughness			Waviness		
			Data	Fits	Resids	Data	Fits	Resids
1	1	1	16.97	17.54	-0.57	70.15	63.23	6.92
2	3	6	22.07	15.29	6.78	54.28	43.05	11.23
1	3	3	12.15	10.64	1.51	40.16	35.68	4.48
1	1	1	17.41	17.54	-0.13	67.47	63.23	4.24
1	2	2	15.05	14.64	0.41	39.58	49.46	-9.88
2	2	4	12.84	9.15	3.69	69.48	36.05	33.43
2	1	2	8.73	7.01	1.72	28.86	29.06	-0.20
1	2	2	13.79	14.64	-0.85	38.88	49.46	-10.58
2	2	4	8.97	9.15	-0.18	49.45	36.05	13.40
2	3	6	14.58	15.29	-0.71	34.33	43.05	-8.72
1	3	3	10.99	10.64	0.35	39.97	35.68	4.29
2	1	2	6.73	7.01	-0.28	20.63	29.06	-8.43
2	1	2	5.56	7.01	-1.45	17.84	29.06	-11.22
1	3	3	8.79	10.64	-1.85	38.95	35.68	3.27
2	2	4	5.65	9.15	-3.50	28.90	36.05	-7.15
1	2	2	15.08	14.64	0.44	45.85	49.46	-3.61
2	3	6	9.21	15.29	-6.08	20.70	43.05	-22.35
1	1	1	18.24	17.54	0.70	64.09	63.23	0.86

A.4 Conclusions

From the above results and discussion, the following conclusions can be drawn:

1. Presence or absence of coatings such as aluminum or zinc is a significant factor that affects both roughness and waviness values.
2. Thickness differential between materials being joined does not seem to be a significant factor but since it has a strong interaction with the existence or non-existence of coating, it cannot be ruled out as being ineffective.
3. Plot of data in Fig. 1.2 suggests that, for smaller thickness differentials, the influence of coatings seem to be greater and it seems to diminish with increasing thickness differentials. In the same way, when coatings are absent, smaller thickness differentials seem to produce lower surface roughness; the roughness values seem to increase with increasing thickness differential. This is attributed to variability in the weld regions when materials with larger thickness differentials are welded together.

APENDIX B. Effect of rolling direction on tensile strength of joints

B.1 Introduction

The effect of rolling direction on the maximum tensile strengths of DP980, TRIP780 and mild steel as well as DP/MS and DP/TR joints are investigated further in this section. The objective is to study the effect of rolling direction on the tensile strengths of these materials, as well as on the welded joints comprising of these materials, and statistically prove (or disprove) that rolling direction has a significance in the maximum tensile strengths.

B.2 Materials and Methods

Large sheets of three materials, TRIP780 (1.0 mm thick with galvanized zinc coating), DP980 (1.5 mm, cold rolled only) and mild steel (0.7 mm, galvanized zinc coating) were specially provided by Arcelor Mittal for this project. The sheets had been marked with rolling direction. Samples were cut along and perpendicular to the rolling direction from the sheets. The edges of the samples were machined using EDM process. The samples were then mounted on weld fixture and welded at 3.8 kW and 70 mm/sec speed. To reduce the number of combinations, the welding was carried out with rolling directions for both samples in the same direction as the tensile test samples (with this direction being perpendicular to the weld line) or with the rolling directions for both samples being transverse to the direction of the tensile test samples (with this direction being parallel to the weld line). The weld scheme is shown in Table B.1 and Figure B.1.

The welded samples were then removed and tensile samples were cut using EDM process. Since the EDM process results in lesser variability compared to waterjet process, this process can be expected to yield more accurate results. Dimensions of the tensile samples are shown in Figure B.2.

The tensile samples were tested in an Instron tester. 6 samples for each joint were tested. Before the tests were run, the widths of the samples were measured and recorded. At the end of the test, the maximum loads carried by the joints were recorded. Confirmation tests were run on regular TRIP-780, DP980 and MS tensile samples cut along the rolling and transverse directions.

Table B.1 Weld scheme for evaluating effect of rolling direction

Designation	Material 1	Material 2
DP/MS-R	DP980 (weld line perpendicular to roll direction; tensile load direction is the same as roll direction)	Mild Steel (weld line perpendicular to roll direction; tensile load direction is the same as roll direction)
DP/MS-X	DP980 (weld line same as rolling direction; roll direction is transverse to direction of tensile load direction)	Mild Steel (weld line same as rolling direction; roll direction is transverse to direction of tensile load direction)
DP/TR-R	DP980 (weld line perpendicular to roll direction; tensile load direction is the same as roll direction)	TRIP780 (weld line perpendicular to roll direction; tensile load direction is the same as roll direction)
DP/TR-R	DP980 (weld line perpendicular to roll direction; tensile load direction is the same as roll direction)	TRIP780 (weld line perpendicular to roll direction; tensile load direction is the same as roll direction)

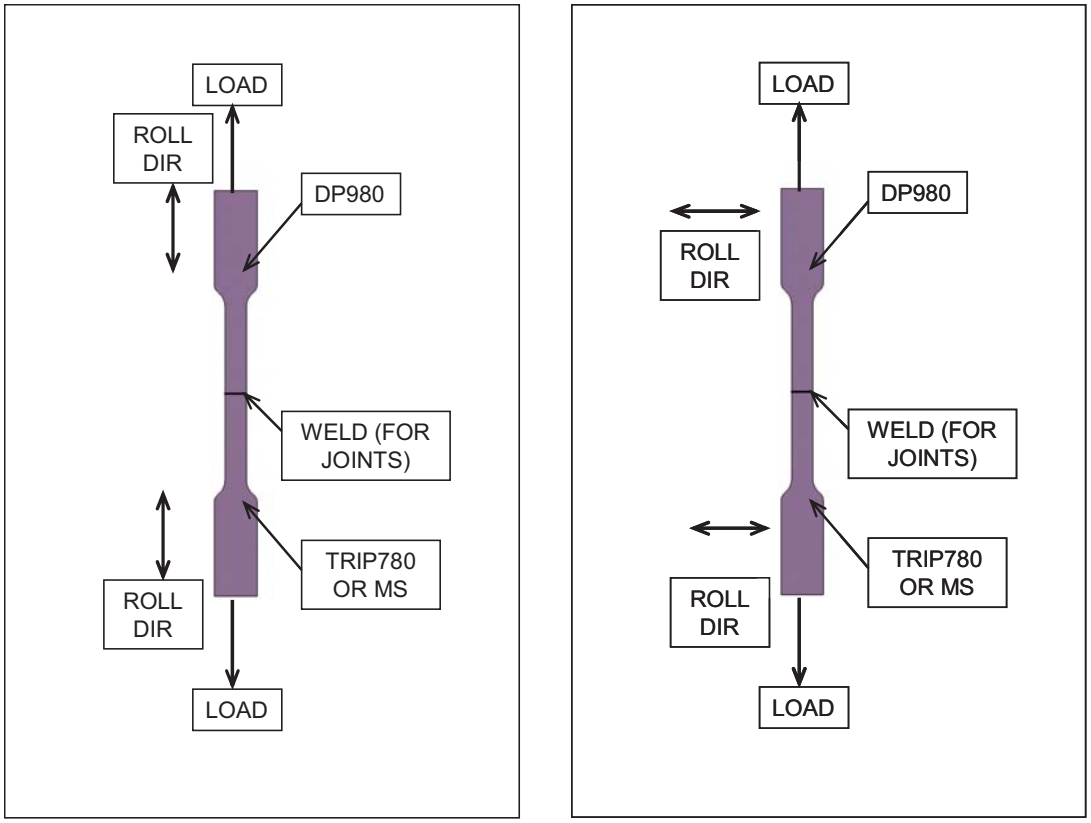

(a) (b)

Figure B.1 Roll directions for (a) DP/MS-R and DP/TR-R, (b) DP/MS-X and DP/TR-X.

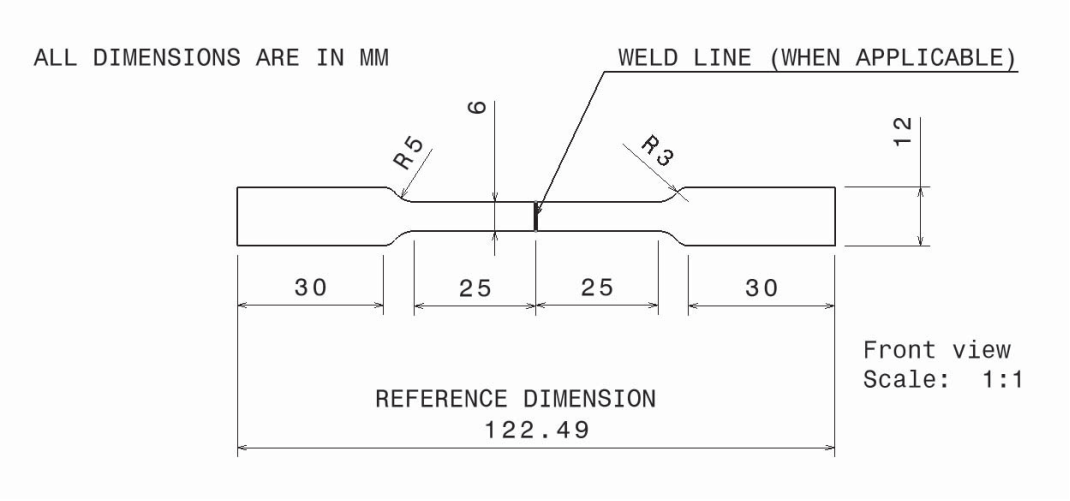

Figure B.2 Dimensions for tensile test samples. Note that the gage length for base materials remains at 50 mm.

B.3 Results and Discussion

B.3.1 Tensile test results for welded joints

All the DP/MS joints fractured in the mild steel region away from the weld and all the DP/TR samples fractured in the TRIP780 region, also away from the weld, suggesting that the welds are excellent in quality. Samples were measured carefully for widths and thickness values, but since the variability of thickness values was negligible, the thickness was not taken into account. However, since there was some variability in the widths of the tensile samples, the values of maximum tensile loads experienced by the joints were normalized to 6.1mm width and are shown summarized in Table B.2. Since the values have been normalized, the maximum tensile loads also represent the maximum tensile stress supported by the samples.

The results shown in Table B.2 were analyzed using Minitab® 15. The box plots and individual plots for the rolling direction versus transverse direction for DP/MS and DP/TR are shown in Figure B.3. Both individual value plot and box plot shown in Figure B.3 (a) and (b) indicate that DP/MS-R fractures at slightly higher loads compared to DP/MS-X. However, it can be noticed that there is considerable overlap in the values as shown in the individual value plots for DP/MS. On the other hand, Figure B.3 (c) and (d) indicate that DP/TR-X fractures at higher loads compared to DP/TR-R. The individual value plots do not show any overlap between roll direction versus cross direction and the boxplot clearly indicates that the steel is stronger in the transverse direction. This contrast between the two is interesting since the cold working and hot working of steels reduce

the ductility, impact and fatigue properties in the transverse direction (Steel castings handbook by Thomas Stevens) and therefore it can be expected that both steels would be stronger in the transverse direction.

Table B.2 Maximum loads during tensile tests

DP/TR-R			DP/TR-X		
Max load (kN)	Width (mm)	Load (kN) normalized for 6.1 width	Max load (kN)	Width (mm)	Load (kN) normalized for 6.1 width
5.108	6.147	5.069	5.144	6.020	5.212
5.009	6.045	5.055	5.246	6.147	5.206
5.024	6.045	5.070	5.146	6.121	5.128
5.048	6.081	5.064	5.161	6.045	5.208
5.001	6.045	5.047	5.173	6.045	5.220
5.047	6.045	5.093	5.147	6.020	5.215

DP/MS-R			DP/MS-X		
Max load (kN)	Width (mm)	Load (kN) normalized for 6.1 width	Max load (kN)	Width (mm)	Load (kN) normalized for 6.1 width
1.385	6.020	1.403	1.388	6.121	1.383
1.389	6.020	1.407	1.386	6.121	1.381
1.385	6.020	1.403	1.387	6.121	1.382
1.392	6.020	1.410	1.385	6.071	1.392
1.385	6.096	1.386	1.386	6.096	1.387
1.392	6.096	1.393	1.390	6.121	1.385

Statistical t-tests were carried out to confirm or reject the null hypotheses that the maximum tensile loads for DP/MS-R and DP/MS-X are the same, and, that the maximum tensile loads for DP/TR-R and DP/MS-X are the same. Results of the t-tests are summarized in Table B.3. The P-value for DP/MS-R versus DP/MS-X is of the order of 0.009, while the P-value is of the order of 0.000 for DP/TR-R versus DP/MS-X. This means that the null hypothesis that the two means are equal can be rejected at $\alpha = 0.05$ for both DP/MS-R versus DP/MS-X, as well as DP/TR-R versus DP/TR-X combinations. As shown in Table B.3, the 95% confidence interval (CI) for the difference in the mean values for DP/MS-R and DP/MS-X is around 0.015 suggesting that the mean value for DP/MS-R is higher than the mean value for DP/MS-X. On the other hand, the difference in the mean values for DP/TR-R versus DP/TR-X is -0.132, indicating that the mean for DP/TR-X is greater than that for DP/TR-R.

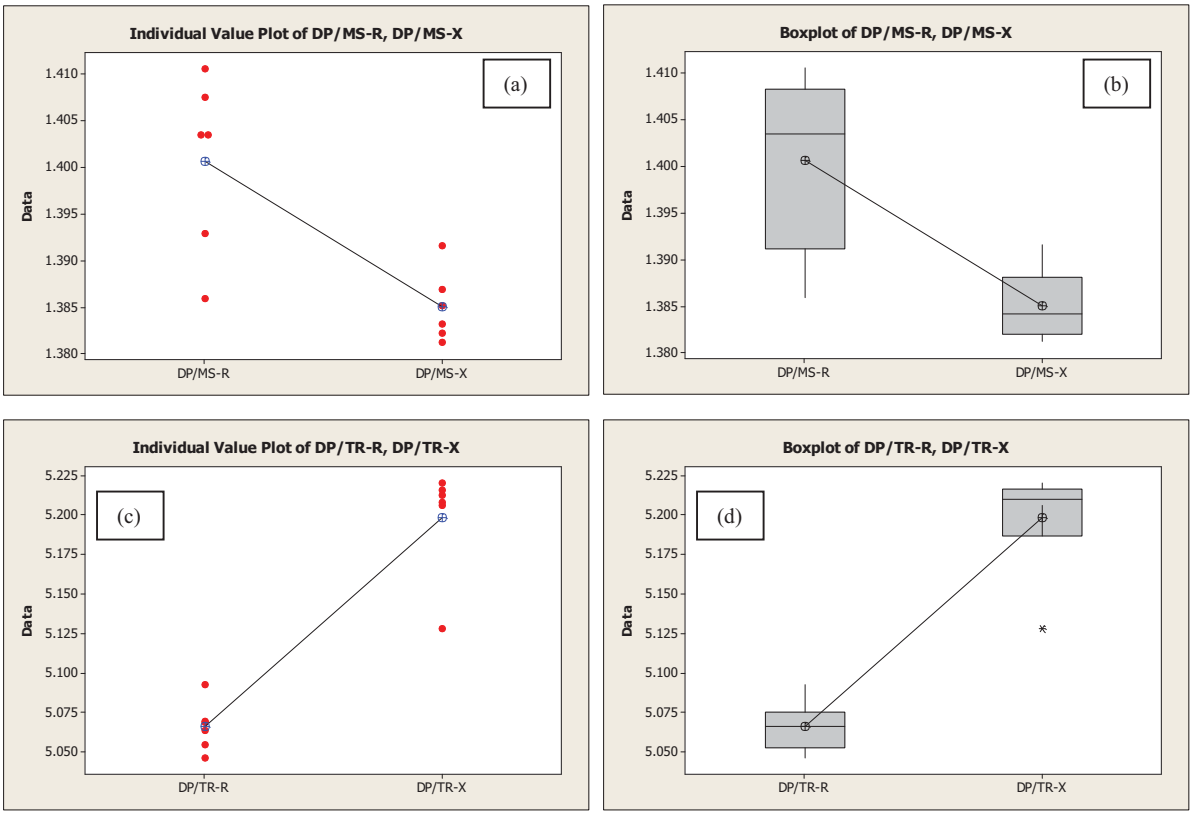

Figure B.3 (a) Individual value plots for DP/MS-R Vs DP/MS-X (b) Boxplots for DP/MS-R Vs DP/MS-X (c) Individual value plots for DP/TR-R Vs DP/TR-X (d) Boxplots for DP/TR-R Vs DP/TR-X

Table B.3 (a) Two-sample T for DP/MS-R vs DP/MS-X

	N	Mean	StDev	SE Mean
DP/MS-R	6	1.4006	0.00933	0.0038
DP/MS-X	6	1.38508	0.0038	0.0016

T-test of difference = 0 (vs not =): T-Value = 3.77 P-Value = 0.009

95% CI for DP/MS-R, DP/MS-X

Difference = μ (DP/MS-R) - μ (DP/MS-X)

Estimate for difference: 0.01552

95% CI for difference: (0.00545, 0.02559)

Table B.3 (b) Two-sample T for DP/TR-R vs DP/TR-X

	N	Mean	StDev	SE MEAN
DP/TR-R	6	5.0661	0.0159	0.0065
DP/TR-X	6	5.1983	0.0347	0.014

T-test of difference = 0 (vs not =): T-Value = -8.50 P-Value = 0.00

95% CI for DP/TR-R, DP/TR-X

Difference = μ (DP/TR-R) - μ (DP/TR-X)

Estimate for difference: -0.1323

95% CI for difference: (-0.1691, -0.0955)

B.3.2 Tensile test results for TRIP780, DP980 and mild steel materials

Since DP/TR and DP/MS combinations exhibited different results, confirmation tests were run on TRIP780, DP980 and MS material samples in both the direction of the roll and in the transverse directions. The goal was to reproduce the results obtained for the mild steel fracture in DP/MS joint and TRIP780 fracture in DP/TR joint, and to understand if the materials by themselves exhibit a different degree of difference for the two directions.

6 samples each of TRIP780 and MS were tested with the tensile samples oriented in the rolling direction and transverse direction. Only 3 samples of DP980 were tested for the two directions. TRIP780 samples oriented in the rolling direction were designated TR-R while those oriented in the transverse direction were designated TR-X; similarly, DP980 and mild steel samples were designated as DP-R, DP-X and MS-R, MS-X. All the samples were nearly identical in the sample widths and had a value of 6.1 mm. For this reason, the need for normalizing the data did not arise.

The maximum loads supported by the samples are all shown in Table B.4. The data suggests that TR-X values are higher than TR-R values, while MS-X values are lower than MS-R values. A clear observation cannot be made for DP980 samples.

Table B.4 Maximum loads during tensile tests

TR-R	TR-X	DP-R	DP-X	MS-R	MS-X
5.037	5.265	9.758	9.714	1.457	1.416
5.025	5.265	9.711	9.711	1.456	1.415
5.048	5.291	9.586	9.732	1.455	1.417
5.064	5.280			1.469	1.418
5.063	5.274			1.456	1.419
5.061	5.271			1.459	1.414

The individual data plots and box plots of these values are shown in Figure B.4. The contrast in the differences for rolling directions versus transverse directions for TRIP780 and MS seem sharper when compared to what can be noted from Figure B.3. Figures B.4. (c) and (d) suggest that there may not be a difference between rolling and transverse directions for DP980 material.

Results of two-sample t-tests are shown in Table B.5. The data shows that hypothesis that the means of TR-R and TR-X are the same can be rejected. The T-values are sharply higher when compared to the values obtained for DP/TR-R versus DP/TR-X and shown in Table B.3. Similarly, the null hypothesis (means are the same) can be rejected for MS-R and MS-X, and at higher T-values when compared to DP/MS-R and DP/MS-X T-values in Table B.3. The P-value for DP-R versus DP-X seems to be high and thus the null hypothesis that the means maximum loads for rolling versus transverse directions for DP980 material cannot be rejected.

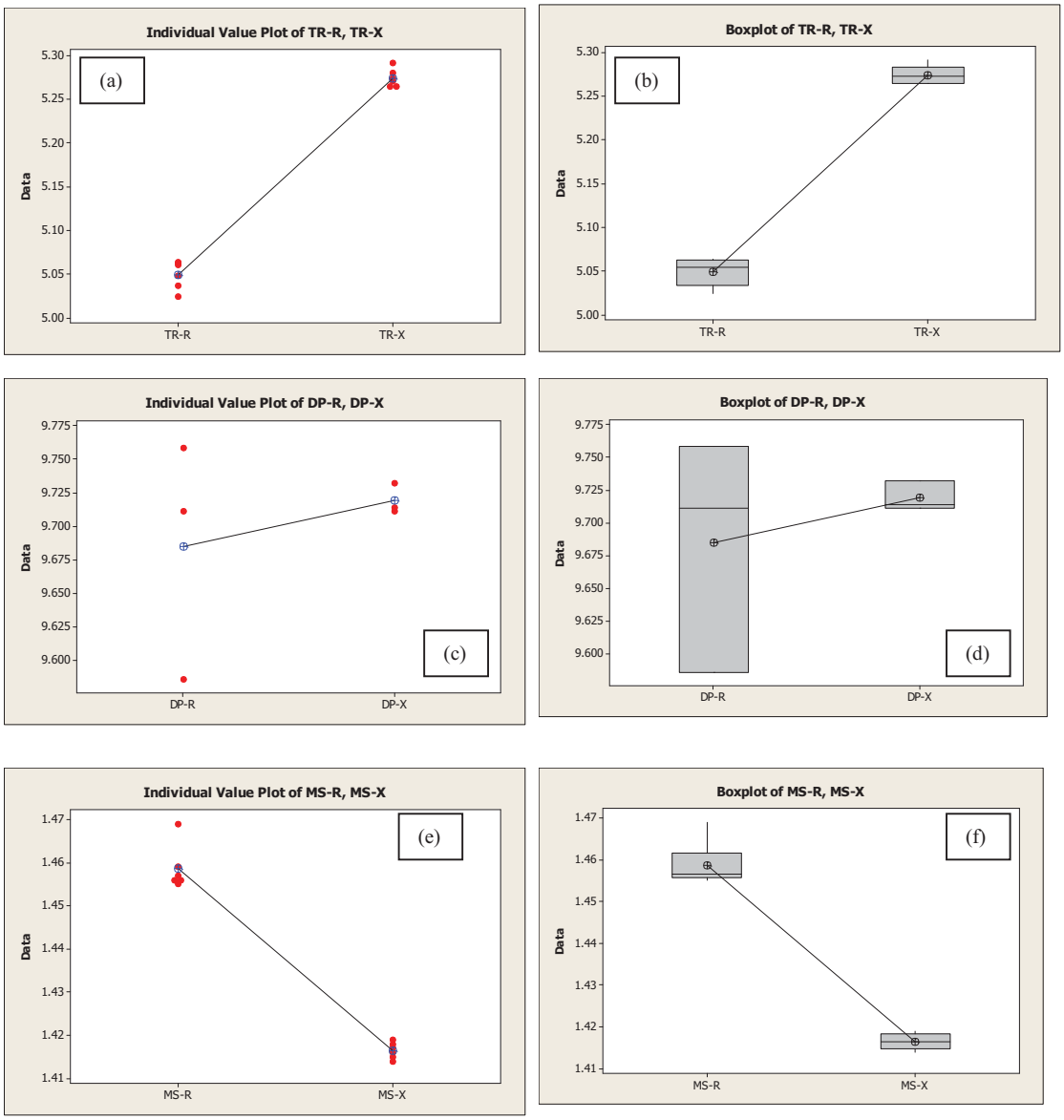

Figure B.4 (a), (b) Individual value plots and boxplots for TR-R versus TR-X
(c), (d) Individual value plots and boxplots for DP-R versus DP-X
(e), (f) Individual value plots and boxplots for MS-R versus MS-X

Table B.5 Maximum loads during tensile tests

Two-sample T for TR-R vs TR-X	Two-sample T for DP-R vs DP-X	Two-sample T for MS-R vs MS-X
N Mean StDev SE Mean	N Mean StDev SE Mean	N Mean StDev SE Mean
TR-R 6 5.0497 0.0160 0.0065	DP-R 3 9.6850 0.0889 0.051	MS-R 6 1.45867 0.00524 0.0021
TR-X 6 5.27433 0.00995 0.0041	DP-X 3 9.7190 0.0114 0.0066	MS-X 6 1.41650 0.00187 0.00076
Difference = mu (TR-R) - mu (TR-X)	Difference = mu (DP-R) - mu (DP-X)	Difference = mu (MS-R) - mu (MS-X)
Estimate for difference: -0.22467	Estimate for difference: -0.0340	Estimate for difference: 0.04217
95% CI for difference: (-0.24242, -0.20691)	95% CI for difference: (-0.2566, 0.1886)	95% CI for difference: (0.03661, 0.04773)
T-Test of difference = 0 (vs not =):	T-Test of difference = 0 (vs not =):	T-Test of difference = 0 (vs not =):
T-Value = -29.18 P-Value = 0.000	T-Value = -0.66 P-Value = 0.579	T-Value = 18.56 P-Value = 0.000

Typical engineering stress versus strain graphs for rolling direction versus transverse direction for the three materials are shown in Figure B.5 (a) – (c). As can be seen, in the case of TRIP780, the maximum stress is larger in the transverse direction, while in the case of MS, the maximum stress is slightly higher in the direction of rolling. Interestingly, the maximum strain before fracture is higher in the rolling direction when compared to transverse direction for all three materials.

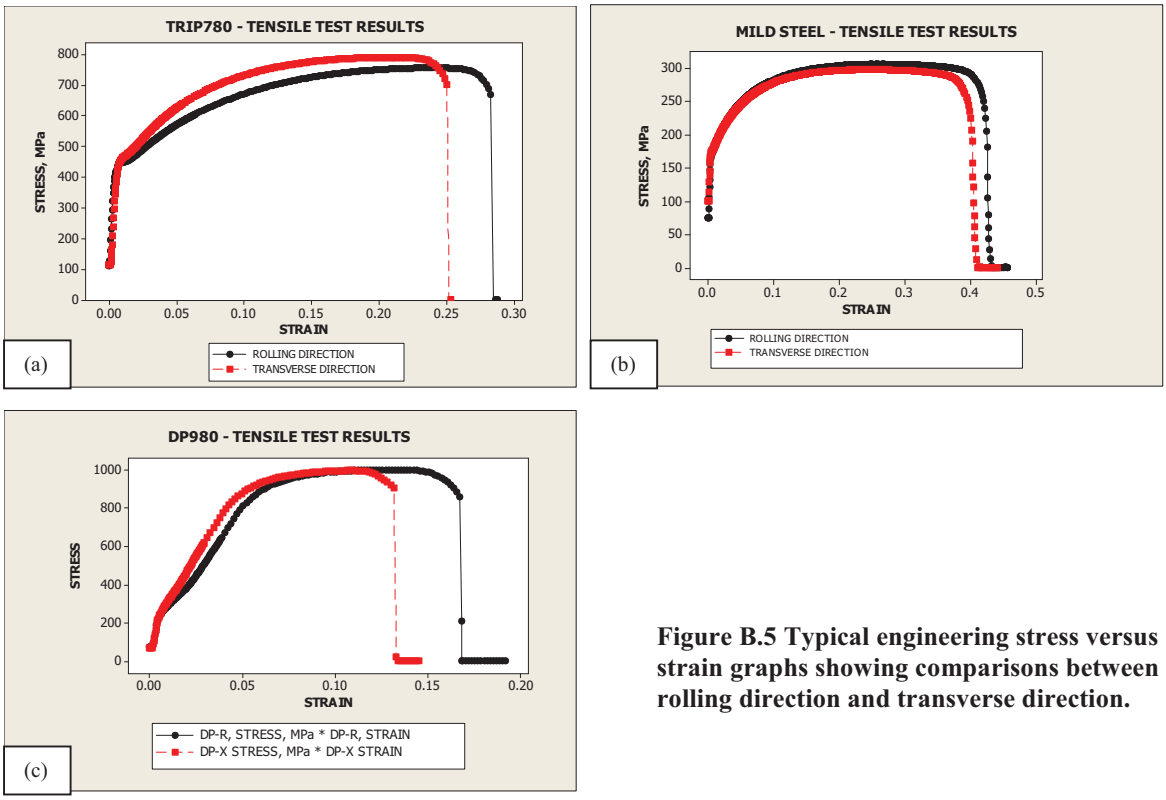

Figure B.5 Typical engineering stress versus strain graphs showing comparisons between rolling direction and transverse direction.

The area under the stress-strain graph up to the yield point represents the resilience of the material while the remaining area under the curve represents the toughness of the material. For the three materials, for the rolling and transverse directions, the areas under the curves from the yield point to the fracture point were computed and are presented in Table B.6. The data suggests that the toughness of all materials is greater in the rolling direction, but the value of toughness in the rolling direction is significantly greater than in transverse direction for DP980 material. These values agree well with what can be noted from Fig. B.5.

Table B.6 Comparison of toughness in rolling versus transverse directions (MPa)

	Area under curve (Toughness)	Difference	% better in rolling direction over transverse direction
TR-R	185.86	12.98	7.5%
TR-X	172.88		
MS-R	120.29	9.17	8.3%
MS-X	111.12		
DP-R	134.52	30.01	28.7%
DP-X	104.50		

B.4 Conclusions

1. The results indicate that statistically there is a difference in the maximum loads (or maximum tensile strengths) in the rolling versus transverse direction for TRIP780 and mild steel materials; however, there is no difference in the maximum tensile strength of DP980 in the two directions.
2. DP980 seems to have significantly higher toughness in the rolling direction when compared to transverse direction.
3. These differences, in turn, affect the performance of the joints, although the significance of the differences get reduced due to other factors such as reduced gage length and the presence of fusion and heat affected zones as well as the presence of other materials.

APPENDIX C. DIODE-PUMPED Yb:YAG DISK LASER

The disk laser (λ=1030 nm) used in this work is a brilliant combination of solid-state (disk) and semiconductor (diode) lasers. The diode laser provides high pumping efficiency while the disk laser generates high beam quality. The key benefits of disk laser compared to the traditional rod type are enhanced electrical efficiency and beam quality. The higher beam quality allows higher energy densities, which in many applications translate directly into faster processing speeds and/or higher precision for welding and cutting applications, albeit at a higher initial system cost. For example, cutting 1-mm mild steel with the 1-kW disk laser was accomplished at nearly twice the speed achieved by a conventional 1-kW Nd:YAG. The advantages of good beam quality are summarized in Table C.1.

Table C.1 Comparison of disk laser to rod laser

	Disk laser (good beam quality)		Rod laser	
Characteristic	Effect	Comments	Effect	Comments
Spot size (with given focal length)	Small	High speed welding	Large	High heat input
Focal length (with given focal length)	Long	Farther from smoke/spatter	Short	Higher mirror/lens/cover slide maintenance
Depth of focus (with given focal length)	Large	Large process window	Small	Harder to find and maintain focus

TRUMPF has developed a disk pumping arrangement featuring a parabolic mirror system, a prism coupling unit, homogenizer, a beam collimator, and diode pumping to produce a device that can be scaled to multi-kilowatt levels at high efficiency and vastly improved beam quality. The specific disk laser used is continuous wave type with 6 kW of power and a beam quality of 8 mm-mrad (TruDisk 6002) and is manufactured by TRUMPF. By comparison, a traditional lamp-pumped Nd:YAG would deliver 4 kW to the workpiece with beam quality of 25 mm•mrad. Unlike rod types, the disk has no thermal lensing, resulting in absence of optical distortion and keeping constant beam quality over the entire power range. Conventional Nd:YAG rod dissipates heat through its cylindrical surface, which is perpendicular to the axis of the laser beam, creating thermal gradients and subsequently thermal lensing. In contrast, the disk dissipates the heat parallel to the axis of the laser beam, resulting in uniform temperature over the disk surface and hence no thermal lensing. Large working distances and narrow focusing optics can thus be realized. Because the disk laser is not sensitive to back reflection, these lasers allow longer fiber lengths for beam delivery and thereby remote welding. In addition, highly reflecting materials such as copper can be processed.

Yb:YAG is the most widely used material for thin-disk lasers because of its long radiative lifetime (~950 μs), its high thermal conductivity (~6 W/m K for typical doping concentrations) and its good mechanical properties. The highest output power demonstrated so far from a single disk is 5.3 kW. The most powerful commercial unit on the market is currently the Trumpf model TruDisk 8002, which puts four disks in a single resonator to generate 8 kW with an M2 beam quality of 24.

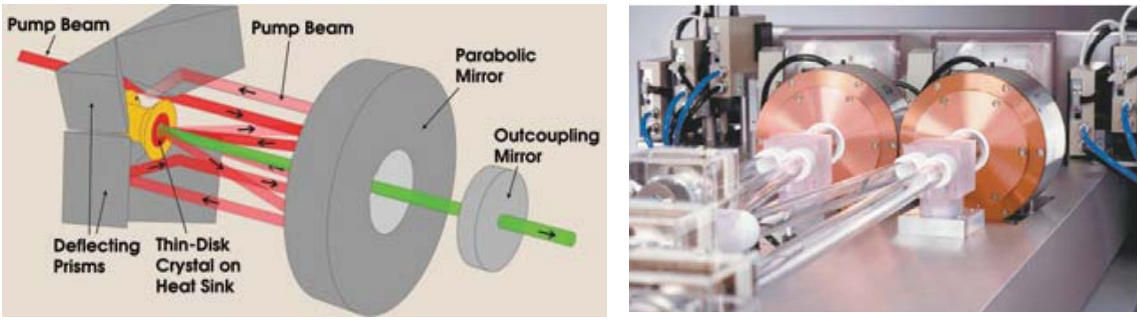

Figure C.1 For efficient absorption, the pump light is reflected through the thin disk multiple times.

Figure C.1 shows a thin-disk design that employs gain media (10% ytterbium content YAG) with a thickness less than 0.2 mm thick and a diameter between 10 and 20 mm, depending on the desired power level. The disks are antireflection-coated for the pumping and lasing wavelengths at the front side and coated for high-reflectivity at both wavelengths on the back. The crystal is mounted on a heat sink and cooled from behind, so that the thermal gradient is nearly perfectly orthogonal to the surface. Thus, thermal lensing is minimal. But because only a small amount of pump light is absorbed by the thin, face-pumped disk, the pump light must be bounced back and forth through the disk numerous times. In practice, a parabolic mirror and deflecting prisms guide as many as 32 passes through the disk. A simple laser resonator can be formed between the highly reflecting back surface of the disk and an output-coupling mirror, or a more sophisticated resonator can employ additional optics to enhance spatial overlap between the pump light and the intracavity mode.

On the welding front, disk laser technology offers several benefits:

1. It allows precision welding of smaller welds with less heat input.
2. In aluminum welding, the system reaches threshold intensity with lower power.
3. The ability to use longer-focal-length optics, particularly scanning optics, which can provide precision beam motion at extremely high speeds, especially in remote welding of complex parts without moving them mechanically.

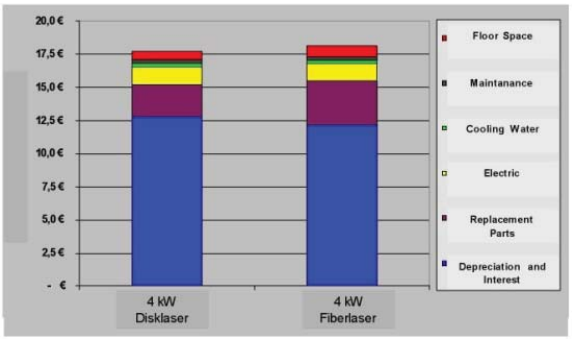

Figure C.2 Operating costs of lasers for a three-shift welding production process over a period of eight years [Reference 2]

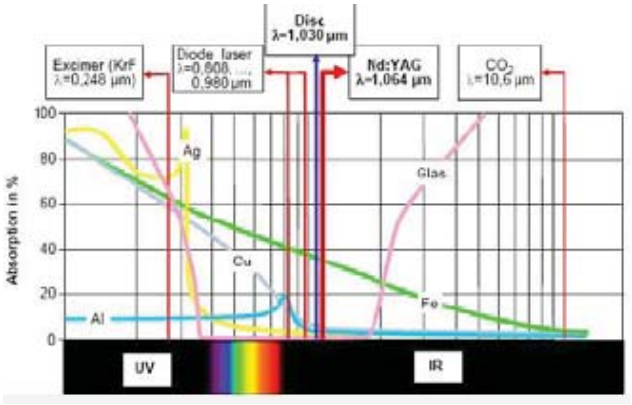

Figure C.3 Absorption energy spectrum of different materials

4. The use of more compact welding optics can be beneficial when welding must take place in confined or difficult-to-reach spaces.
5. It is superior to the recently developed fiber laser as the operating costs are lower (Figure C.2).
6. It has improved energy absorption compared to the traditional Nd:YAG and CO2 lasers (Figure C.3).

Reference

[1] D. Havrilla, "YAG is redefined through the diode-pumped disk laser," Laser Focus World, August 2005, 102-105

[2] Schluter, H. Thin-disk-laser power scaling improves welding efficiency. Laser Focus World, 12/15/2006. http://www.laserfocusworld.com/ARTICLES/280055